Engineering 3D Human Cardiac Ventricular Models with Controllable Architecture

Nisa Penland Williams

A dissertation

submitted in partial fulfillment of the

requirements for the degree of

Doctor of Philosophy

University of Washington

2020

Reading Committee:

Charles E. Murry (Chair)

Deok-Ho Kim

Michael Regnier

Program Authorized to Offer Degree:

Bioengineering

University of Washington

Abstract

Engineering 3D Human Cardiac Ventricular Models with Controllable Architecture

Nisa P. Williams

Chair of the Supervisory Committee:

Charles E. Murry, M.D., Ph.D., Professor

Department of Pathology

Department of Bioengineering

Department of Medicine/Division of Cardiology

Tissue engineering combined with the power of stem cell technology provides unprecedented opportunity to interrogate and discover human biology. The derivation of human cardiomyocytes from induced pluripotent stem cells (iPSCs) has enabled the development of de novo cardiac tissues that recapitulate several characteristics of functional human myocardium. These platforms act as advanced models with which cardiac development, biomechanics, and disease pathology can be reverse engineered

to glean otherwise unobtainable information that has great significance to human health. Despite this progress, tissue engineering is in its infancy, and the ability to produce cardiac tissues that mimic the function of mature adult myocardium has proven to be quite challenging. Using immature tissues for disease modeling or developing novel therapeutics poses a potential danger for generating falsely positive or negative results. To combat this risk, there has been significant effort in developing biofabrication strategies to recapitulate the complex tissue architecture of the myocardium. However, there are few platforms available that can recreate the multiscale organization of the heart, including tissue anisotropy, helical myocardial organization, and ventricular and atrial chamber geometries. To address this shortcoming, we have developed a nanopatterned cell sheet technology for fabrication of complex 3D cardiac ventricular models with controllable cellular architecture. In this approach flexible thermoresponsive nanofabricated substrates (fTNFS) were used to create sheets of organized cardiac tissue and cast them into simplified chamber geometries such as a hollow tube or cone shape. These tissues exhibited spontaneous beating and could create measurable pumping pressures. Additionally, we measured functional benefits from tissues with anisotropic cellular patterning as compared to tissues with non-biomimetic cellular arrangements. We also observed that tissues patterned with circumferential cellular alignment exhibited surprising cellular remodeling where the cells rotated almost 90 degrees in orientation from their initial circumferential pattern. Upon modeling this effect computationally using finite element analysis, we discovered large gradients of shear stress perpendicular to cellular alignment that may have motivated cellular reorganization. Together, these findings demonstrate the importance of mimicking myocardial

architecture in engineered tissue models. These works provide an advanced platform for studying tissue structure-function relationships in cardiac development and disease.

Table of Contents

List of Figures

Acknowledgements

I would first like to thank my advisor, Prof. Deok-Ho Kim. You saw potential in a young student who had little experience in engineering and gave me the chance to learn many new disciplines and grow into the scientist that I am today. You always encouraged me to explore new and creative methods to push the boundaries of my experimental process and gave me free reign to do so. I will forever be grateful for your impact on my graduate experience and beyond.

I also owe great thanks to my supervisory committee, Prof. Charles Murry, Prof. Michael Regnier, Prof. David Mack, and Prof. Jeffery Chamberlain, for their tremendous mentorship and guidance in my graduate experience. You all have had immeasurable impact in my development as a thinker, a scientist, and a member of the scientific community.

There have been many members of my research community, past and present, that have provided me with a wealth of enriching experiences, opportunities for collaboration, mentorship, and friendship. Although they are not all listed here, these are several individuals who have had an impact during my graduate studies: Dr. Jon Tsui, Dr. Alec Smith, Travis Moerk, Changho Chun, Dr. Jongseob Choi, Dr. Joy Su, Yeseul Kim, Dr. Jesse Macadangdang, Dr. Alex Jiao, Winnie Leung, Marcus Rhodehamel, Calysta Yan, John Foster, Mikael Perla, Joseph Henthorn, Yu Jung Shin, Rahaf Qamou, Jasmine Rinnofer, Hyejin Kim, Elisa Clark, Saffie Mohran, Nicole Zeinstra, Dr. Christian Mandrycky, Kevin Beussman, Dr. Farid Moussavi-Harami, Dr. Nate Sniadecki, Amy Martinson, and Dale Haley.

I would be remiss to not also acknowledge the several women in science that I have been surrounded by over the past 6 years. Specifically, I would like to thank Drs. Kelly Stevens, Jen Davis, Ying Zheng, Hanele Ruhola-Baker, Carol Ware, and Lil Pabon. You all have been amazing examples of successful and intelligent women in science. You are doing cutting-edge science, taking on leadership roles, and promoting the future of women in a field that has been historically dominated by men. I thank you all for your inspiration and the role you played in giving me confidence to pursue a career in science.

I would like to thank my family for their unconditional love and support throughout my life. Mom, thank you for teaching me to be a strong and caring person, and to stand up for myself. Dad, thank you for encouraging me to be curious of the world around me and showing me how to be resilient in the face of challenge. Alec, thank you for teaching me to always be true to who I am and to do the things that I love in life and not just those that others expect of you.

Lastly, I thank my husband, Andy Williams, for believing in my ability to succeed in opportunities that I never thought I would be capable of. You have provided me with irreplaceable emotional and scientific support that without I know I could not have achieved this goal. I will forever remember this time and love you all the more for it as we grow old together. I love you.

For my husband

Chapter 1. Introduction

1.1 Cardiovascular Disease and Implications for Human Health

Cardiovascular disease (CVD) has been the leading cause of death worldwide for over a century. In the United States in 2017, heart disease claimed over 900,000 lives where 17.78% of those deaths were attributed to ischemic heart disease[1]. Many of these CVDs result in heart failure by ischemic injury, or myocardial infarction, where the supply of oxygen to the heart muscle is disrupted and or blocked resulting in muscle death. Upon an ischemic event, the necrosis of the heart muscle begets a cascade of immune and fibrotic responses resulting in the formation of a non-contractile scar[2]. The substitution of stiff scar for functional muscle tissue tips the balance of heart function towards failure. It is this viscous cycle that predicates an excessive financial burden of $351.2 billion of direct and indirect costs on the American health care system each year[3].

1.1.1 Limited Regenerative Capacity of the Human Heart

The crux of heart disease is the extremely limited regenerative capacity of the heart where after ischemic injury new cardiomyocytes do not have the capacity to proliferate and replenish the lost cell population[4]. Humans are unlike lower vertebrates such as the zebrafish and salamander who can regenerate their adult hearts when injured [4–6]. Human fetal cardiomyocytes are highly proliferative to build the early heart's structure and increase its size with development[7]. However, after birth human cardiomyocytes are only proliferative for a short time (about 1 week in the mouse heart) before they

withdraw from the cell cycle and enter a hypertrophic state to increase in size rather than number[8]. This is as evidenced by the presence of bi-nucleated cardiomyocytes in the adult heart and formation of mature intercalated discs between neighboring cardiomyocytes[9]. The physiological reasons for binucleation in the heart are still not well understood, but one biological argument is that binucleation occurs to meet the high metabolic demand of the heart where resources and energy are devoted to maintenance of contractile machinery and protein production [9,10]. Additionally, measurements of radioactive carbon-14 (^{14}C) from above-ground nuclear bomb testing have been performed with genomic DNA from individuals born during the Cold War era, around 1963[11]. These experiments suggested that cardiomyocytes have a decreasing turnover rate from 1% at age 25 to 0.45% at age 75, and fewer than 50% of the cardiomyocytes in the heart are replaced over a lifetime. The fact that there is some turnover of cardiomyocytes within the heart suggests that there is the potential to encourage or force them to re-enter the cell cycle through viral transduction or drug delivery. However, there is little evidence so far that this is possible as of now[4].

1.1.2 Prohibitive Costs of Clinical Trials and Reasons for Failure

In tandem to the limited regenerative capacity of the heart in response to injury, there are currently no available therapies that treat the underlying mechanism for ischemic heart failure, but rather are palliative and treat the resulting symptoms of the pathology. One reason for the lack of treatment options may be the dearth of suitable drug candidates that pass through the approval process of the United States Federal Drug

Administration (FDA). For example, for every 10,000 compounds that are screened there are only a few that are further evaluated through clinical trials, and only one that receives final FDA approval[12]. Additionally, the drug development process is estimated to cost between $2 and $3 billion per approval due to high costs in research and development, extensive animal testing, several clinical trial phases, and lengthy FDA approval processes[13]. This cost is prohibitive for the development of many novel drugs and slows the rate of translation from bench to bedside.

Although this problem is multifaceted, a major reason for this high attrition rate and lofty price tag is thought to be due to a lack in translation of experimental findings in animal models to human physiological outcomes[14]. Experimentation with animal models has provided extraordinary insight into fundamental cardiac developmental biology, disease pathophysiology, and subsequently potentially druggable target pathways for therapy development[15]. However, the physiology of animal models does not fully recapitulate that of the human and therefore assumes risk of negative or deleterious outcomes in clinical trials.

For example, there are several examples of drugs that produced promising results in a small animal models but failed once they underwent clinical trials because they precipitated unforeseen cardiotoxicity[16]. As an example, terfenadine (trade name Seldane) was pulled from the US market by the FDA in 1997 for elevated risk of cardiac arrythmia[17]. Terfenadine and may others, are now known to target the human ether-a-go-go gene (HERG) that encodes the delayed rectifier current (I_{Kr}) present in the human ventricles and causes long QT syndrome[18,19]. However, there are several other ion-channels that participate in the cardiac action potential that could be impaired through

drug off-target effects. In response to the clandestine pro-arrhythmic effects of several drugs, the Comprehensive In Vitro Proarrhythmia Assay (CiPA) Initiative was founded in 2013. Their goal is to evaluate proarrhythmic risk based on mechanistic electrophysiologic understanding of proarrhythmia by testing and modeling drug effects on cardiac currents and using this data to predict clinical effects based on electrocardiogram data from phase 1 clinical trials[20].

The CiPA initiative like many other industry and academic institutions before it have recognized the shortcomings of modeling drug responses and diseases in animal models and have begun to adopt the power of human induced pluripotent stem cell (hiPSC) technology[16]. In 2006, Drs. Shinya Yamanaka and Sir John B. Gurdon discovered that human adult somatic cells could be reprogrammed back to their pluripotent state and give rise to all cell types within an organism[21]. This seminal technology provides an inexhaustible source of human cardiomyocytes and other cells from the cardiac lineage[22]. To address the need for human cardiac tissue models for drug testing and biological study, the relatively young fields of tissue engineering and induced pluripotent stem cells have begun to marry concepts of engineering biological microenvironments with the ability to derive human cardiac cell populations[17]. Namely, cardiac tissue engineering has the power to recreate aspects of the cardiac niche, both chemically and physically, to produce human cardiac tissue models that exhibit some structural and functional characteristics native heart tissue[23]. Engineered human cardiac tissue could provide a complementary testbed to animal models for therapeutic development and potentially shoulder some of the translational burden.

1.2 Human Induced Pluripotent Stem Cells: Applications and Limitations

Before the dawn of stem cell technology, sources of human cells were extremely limited and explanted cells from patient biopsy sources could not be maintained in culture for very long, with the exception of immortalized cell lines such as HeLa cells [24]. Now, only 14 years after the discovery of reprogramming adult somatic cells into a pluripotent state, there have been thousands of publications on the derivation of almost every cell type in the body including cardiomyocytes[25] and vascular cells[26], hemopoietic[27] and immune cells[28], germ cells[29], kidney[8], liver[30], neurons[31], and skeletal muscle[32] and bone[33]. Abundant sources of human iPSC-derived cardiomyocytes (hiPSC-CMs) has enabled the development of single-cell to cardiac microphysiological systems to model cardiovascular development[22,34] and disease[35], screen drug compounds for cardiotoxic effects[36], and develop *de novo* sources of cardiac tissues for implantation and regenerative medicine[25,37].

1.2.1 Use of iPSCs for Modeling Cardiovascular Development

Modeling cardiovascular development or disease in the dish can provide unique insight into fundamental mechanisms that might govern tissue morphogenesis or pathology[38]. The use of cardiac organoids has become increasingly popular for recreating the environment of the developing cardiac niche with respect to its 3D nature, tissue stiffness, and clustering of cardiac progenitor cells[34,39,40]. For example, Z. Ma and colleges fabricated culture wells patterned with polyethylene glycol (PEG) to

geometrically confine hiPSC colonies and spatially present mechanical stress[41]. By modulating Wnt-signaling to specify cardiac mesodermal lineages in confined colonies, they observed greater cell density on the perimeter which corresponded with higher expression of OCT4 (a marker of pluripotency) and E-cadherin (a known mechano-sensing structure and a marker of pluripotent maintenance). Cells on the perimeter eventually gave rise to myofibroblasts expressing SM22, calponin, and smooth muscle α-actin. Conversely, they observed lower cell densities in the center of the colonies and expression of N-cadherin which is an indicator of epithelial to mesenchymal transition and subsequent development of cardiomyocytes forming hollow microchambers. These results demonstrate how biophysical cues direct cell condensation and lineage specification and that they can be controlled experimentally to explore the mechanisms of early cardiac development. This model and others like it offer reproducible methods to study the emergent properties of heart development in healthy and diseased patients, such as those with congenital heart defects for example[40,42].

1.2.2 Use of iPSCs for Modeling Cardiovascular Disease

Intrinsic to cellular biology and stem-cell technology is the capacity to generate iPSCs from any individual using almost any cell in the body as starting material. This property opens the door for modeling cardiomyopathies in the dish with relative ease[43]. For example, several groups have utilized patient urine cells or skin fibroblasts taken from individuals with Duchenne muscular dystrophy (DMD) and reprogrammed them back to a pluripotent state using viral delivery of the Yamanaka factors[21,44–46]. DMD is an X-linked muscle wasting disease that predominantly impacts young boys and affects their

skeletal, cardiac, and smooth muscle. As a result, these boys typically survive into their early twenties and are dying more often from their developed dilated cardiomyopathy which eventually outweighs their loss in skeletal muscle function. Their cell samples were then differentiated into skeletal myoblasts and cardiomyocytes to examine their *in vitro* phenotypes including metabolic, functional, and transcriptomic profiles. In each of these studies, the dystrophic iPSC-CMs displayed elevated cytosolic calcium levels, weaker contractile forces, heightened responses to hypotonic stress, and slower mitochondrial pore opening compared to iPSC-CMs from healthy donors[44–46].

1.2.3 Gene Editing Stem Cells for Disease Modeling

These and other groups have provided models with which potential therapies could be developed by identification of druggable targets or even gene editing. With the discovery of gene editing approaches such as zinc finger nucleases[47], transcription activator-like effector nucleases (TALENs)[48], and clustered regularly interspaced short palindromic repeats (CRISPR)-Cas systems[49], patient-specific iPSC lines can be genetically manipulated to correct or produce mutations of interest[50,51]. This is particularly useful for several reasons, including producing isogenic control iPSC lines where a diseased cell line can be genetically edited to correct its mutation producing a ‘healthy’ control line, or inversely, producing an identical mutation in a healthy-donor line to recreate a known disease mutation[52]. Through this process, a form of forward and reverse engineering, great insight can be gleamed about the mechanistic underpinnings of disease pathology. For example, J.G.W. Smith and colleges generated iPSC lines from family members who were either healthy (non-carrier) or carriers of a mutation in the ACTC1 gene that encodes

for cardiac α-actinin sarcomeric protein[53]. This mutation results in a post-translation substitution of an amino acid E99K which is related to hypertrophic cardiomyopathic (HCM) phenotypes. iPSC-CMs from carriers of the mutation recapitulated several aspects of the disease phenotype, such as abnormal contractility, calcium sensitivity and handling, arrythmogenesis, and hypertropic signaling profiles. These aberrant phenotypes were more pronounced in the mutant iPSC-CMs than in the healthy or isogenic controls, further suggesting the role of the mutant protein in HCM. These disease phenotypes could be rescued through treatment with drugs targeting calcium handling pathways, specifically ranolazine and dantrolene in combination. Most interestingly, the researchers noticed a marked difference in phenotype from the lines generated from the heterozygous father as compared to the 19-year-old son who was also a carrier. This finding was unexpected and potentially speaks to the difference in age between the father and son but could also have implications in disease severity between patients even when they are related. For example, unique differences in the genetic mutation itself and the background epigenetics are likely influencing factors on the genetic and phenotypic manifestation for each individual.

1.2.4 Representing Genetic Diversity in the Dish

Production of individual patient-specific iPSC lines and complementary isogenic controls provides more precise models for disease study however they do not capture the diverse patient population that suffers from any disease phenotype. As demonstrated by a previous example, genetic and phenotypic variances exist between individuals of different age, sex, and race, and therefore disease manifestation can also differ between

individuals, even of the same familial tree[53]. Subsequently, the iPSCs derived from different individuals can similarly present diverse phenotypic behavior within an engineered environment. The time and resources required to develop iPSC lines from patients is non-trivial and can therefore make modeling patient diversity within an *in vitro* study complicated. This is well understood to be a necessary hurdle to overcome in order to utilize human iPSCs as a translative tool for disease modeling and therapy development[54]. If genetic and phenotypic variance are not considered, it is possible that a promising therapeutic in the *in vitro* setting could fail in clinical trials, similarly to the failures of therapy development in animal models[55]. In the face of this challenge, there have been some large-scale studies that attempt to account for this by developing large banks (~50-700) of patient iPSC lines from diverse backgrounds and performing phenotypic and genetic profiling[54,56,57]. These studies characterize several cell lines based on their morphology, reprogramming and differentiation, transcriptome, proteome, and epigenome to identify how variation is commonly regulated between cell lines[58]. By comparing hundreds or thousands of cell lines, patterns can emerge that might provide insight into how genetically complex disorders such as cardiovascular, blood, and neurological disorders[59,60].

1.2.5 *In Vivo* Applications of iPSC-Derived Cardiomyocytes

Given the limited regenerative capacity of the heart, an immediate application of the unlimited source of human iPSC-CMs was to explore their capacity to rescue lost heart function after ischemic injury[4,37,61,62]. There have been several approaches to deliver *de novo* cardiac muscle to the infarcted area of the injured heart including surgical

implantation of engineered muscle sheets[63], injection of human embryonic stem cell (hESC)-derived cardiomyocytes into the heart wall[64], or delivery of reprogramming factors in attempts to transdifferentiate resident fibroblasts into cardiomyocytes[65]. There has been success in rescuing some heart function with each of these methods in small and large animal studies although the mechanism behind functional improvement is still unclear. Cell sheet patches provide applicational advantages by their relatively large size (~ 4 x 2 x 1.5 cm)[66], use of naturally derived scaffolding (e.g. cell matrix secretion, fibrin or decellularized tissue)[67], and potential incorporation of releasable factors to promote angiogenesis and cell survival[68]. Patches are typically glued and or sutured onto the epicardial surface of the heart and have shown improvements in cardiac function weeks after an ischemic event[69]. For example, L. Gao and colleges developed a multi-cellular (cardiomyocytes, smooth muscle cells, and endothelial cells) fibrin patch with embedded microspheres that provided slow release of insulin growth factor 1 (IGF1) from the patch to the infarcted area. They saw reduction in the infarct size (~ -1.5% in area), improved pressure production (+10 mmHg) and left-ventricular ejection fraction (LVEF, ~ +4%) four weeks after myocardial infarction[68]. This approach addressed several gaps in knowledge about the role of tissue-engineered patches and their associated factors in promoting the survival and engraftment of transplanted cardiovascular cells[66]. However, a limitation to this approach is the relatively invasive application which requires open-chest surgery and could introduce additional safety concerns in the translation to humans. Other approaches such as cellular or drug injection via catheterization could provide an advantage over additional invasive surgery.

Attempts to re-muscularize the damaged heart through direct injection has been extensively explored and has provided marked improvement in heart function in large animal models, including non-human primates[2,4,61,70,71]. For example, Y. Liu and colleges demonstrated in a seminal study that cardiomyocytes derived from two different hESC lines were capable of making large engraftments into the non-human primate, *Macaca nemestrina*[37]. Fourteen days after infarction, human ECS-CMs were delivered via a left-sided thoracotomy and multiple syringe injections through the epicardial surface into the infarcted region of the heart. Four weeks post-injection, LVEF% was improved by 10% compared to baseline measurements taken after infarction. Additionally, two treated primates were evaluated at twelve weeks post-injection and their LVEF% was nearly restored to pre-infarction baselines. These experiments also demonstrated injected-cardiomyocyte elongation and maturation, coupling with host tissue through intercalated disc and gap junction formation, improved vasculature formation in the graft tissue compared to the fibrotic scar regions. This and other studies have demonstrated the extremely promising translational aspect of human cell therapy for heart failure, but they have also been accompanied by ventricular tacharrythmias[37,72]. The arrythmias are thought to be due to micro-reentry patterns or abnormal pulse generation from the engrafted tissue[37] or the epicardial surface[72], respectively. These results are still not fully understood and are under extensive interrogation as they are an extremely limiting factor in the translation to human application.

Given the current difficulties with cell-sheet patch and direct injection therapies for cardiac regeneration, direct cellular reprogramming of resident cardiac fibroblasts has also provided a novel approach for treatment of heart failure[65]. These resident fibroblasts

have been the recent target for direct reprogramming through exposure to a cocktail of transcription factors and small molecules[73,74]. Namely, Gata4, Mef2c, with Tbx5 (GMT) and or HAND2 were demonstrated to directly reprogram committed murine cardiac fibroblasts into beating cardiomyocytes both *in vitro* and *in vivo*[75,76]. Mice treated with GMT through direct injection with GMT-encoding retrovirus demonstrated rescued cardiac function by about 10% within two weeks after delivery and increased to 15-20% rescue after six or twelve weeks[75]. These and other direct reprogramming studies in the sensory neurons provide exciting prospects for regeneration in tissues that are considered to have little to no regenerative capacity. However, the local delivery of retrovirus poses some concern for off-target effects by negatively affecting neighboring cell types or downstream affects in other parts of the body.

An emerging body of thought that is worth discussing is the role of the immune system in the repair and improvement of cardiac function after ischemia and therapeutic treatment. The improvements in cardiac function afforded by the application of a cardiac patch, direct injection of hEC-CMs, and direct reprogramming are not well understood as to *how* these treatments provide a rescuing effect on cardiac function. A notable hypothesis is that the triggered immune response that occurs after an ischemic event *and* in response to a post-infarct treatment (e.g. cell injection) plays a large, and potentially dominating, role in the rescuing effect[77]. It is well understood that following an ischemic event, the heart muscle begins to necrose with the lack of oxygen from decreased blood flow. In response, two waves of macrophage responses are set into motion that ultimately recruit resident fibroblasts and promote their differentiation into activated myofibroblasts [78]. Upon activation, myofibroblasts begin to secrete dense extracellular matrix to form a

fibrotic scar that is both a necessary response to prevent the heart from rupturing but also reduces the contractility and compliance of the heart leading to reduced heart function. Additionally, the administration of a therapy to treat the infarction, there is an immune response that follows that event as well. There is evidence that even injection of fractionated or dead mononuclear cells can also provide functional benefits for cardiac function[77]. This result demonstrates the powerful role that the immune system plays in therapeutic response and should be greatly considered and investigated going forward in development of regenerative therapies for heart failure.

1.2.6 Immaturity of Stem-Cell Derived Cardiomyocytes

Reprogrammed or embryonic stem cell-derived cardiac progenitors or cardiomyocytes are a powerful tool that can be used to study cardiovascular development, function, and disease in the dish, and even serve as a potential treatment for heart failure. However, a widely recognized limitation of using iPSC-CMs as an *in vitro* model is their relative immaturity both structurally and functionally compared to the adult cardiomyocyte[71]. For example, induced cardiomyocytes are smaller and rounder in size and have reduced membrane capacitance, higher resting membrane potential, shorter sarcomere lengths (~ 1.6 μm vs. 2.2 μm), more fetal ratios of β:α myosin heavy chain isoforms, lower contractile force, and lack T-tubules[71]. These and other differences in their transcriptomic, genomic, and proteomic profiles present problems for accurately representing cardiovascular biology and pathology *in vitro*. This is particularly true for CVDs that have late onset and require more mature cells to reproduce the disease phenotype, such as dystrophic cardiomyopathy that is associated with Duchenne muscular dystrophy[79].

Additionally, these differences could also present as a potential pitfall for drug screening where the results achieved within an *in vitro* setting could be an artifact or false positive of a cell-model system[80].

The prevailing hypothesis surrounding this observation is that the culture conditions that are used to differentiate and culture iPSC-CMs are wildly foreign compared to the multidimensional and dynamic microenvironments of the native heart tissue and do not promote adult-like maturation. Firstly, the tissue culture dish is two-dimensional (2D) and extremely stiff (10^9-Pascal range) compared to the 3D native cardiac tissue (10^3-Pascal range)[81]. There have been large scale efforts to address this problem by the cardiac tissue engineering field by developing platforms to better recapitulate the native cardiac microenvironment, provide mechanical and electrical conditioning, and utilize small molecules such as the T3 hormone to improve iPSC-CM maturation[82]. However, there are only a few platforms that have been able to reproduce cardiac tissues with adult-like structural and functional properties[23,83]. It is possible that these platforms are still too dissimilar to the anisotropic, 3D environment of the adult or even fetal myocardium. To adequately address this issue, one must first appreciate the morphogenesis of the heart and the relationships that exist between the structural architecture of the myocardium and its organ-level function.

1.3 Multi-scale Structure and function of the Heart: Organ Function to Cellular Organization

1.3.1 Heart Morphogenesis

The primitive stricture of the embryonic heart, or the heart tube, is one of the first structures to form in the developing embryo, just 22 days after fertilization in humans (**Figure 1A**) [84,85]. The rightward bending or looping of the heart tube is the first event that breaks developmental symmetry in the embryo and is highly conserved, so much so that incorrect looping can halt further embryological development [86]. Furthermore, each of the stages of heart development are highly conserved among vertebrates although the speed and timing of these events are variable (**Figure 1B**). This intricate and robust process requires timely positioning, migration, proliferation, and cell-fate specification of several cell populations in concert with embryonic structural and mechanical cues.

The heart tube exhibits complex geometric changes during looping and the identities of the comprising cell populations are also dynamic throughout cardiac morphogenesis (**Figure 1C-D**)[87]. The linear heart tube first consists of two layers of beating cardiomyocytes encircling a layer of cardiac jelly, a mixture of hydrophilic of extracellular matrix proteins which separates the cardiomyocytes from an inner endocardial cell layer and lines the hollow lumen of the heart tube[87]. Fate-mapping studies have revealed that certain regions of the linear heart tube are destined to become the different atrial and ventricular chambers of the adult heart (**Figure 1A**)[88]. The following steps of development act to fold these regions into their anatomical locations within the four-chambered heart. Shortly after the linear heart tube forms it begins to increase in

size and rotate, or loop, to the right side to create a C-shaped bend (C-looped heart tube). Subsequently, the section of the heart tube that will become the ventricles moves downward forming the S-looped heart tube. The last stage of looping occurs by nestling the aorta between the developing atria to begin forming a four-chambered organ.

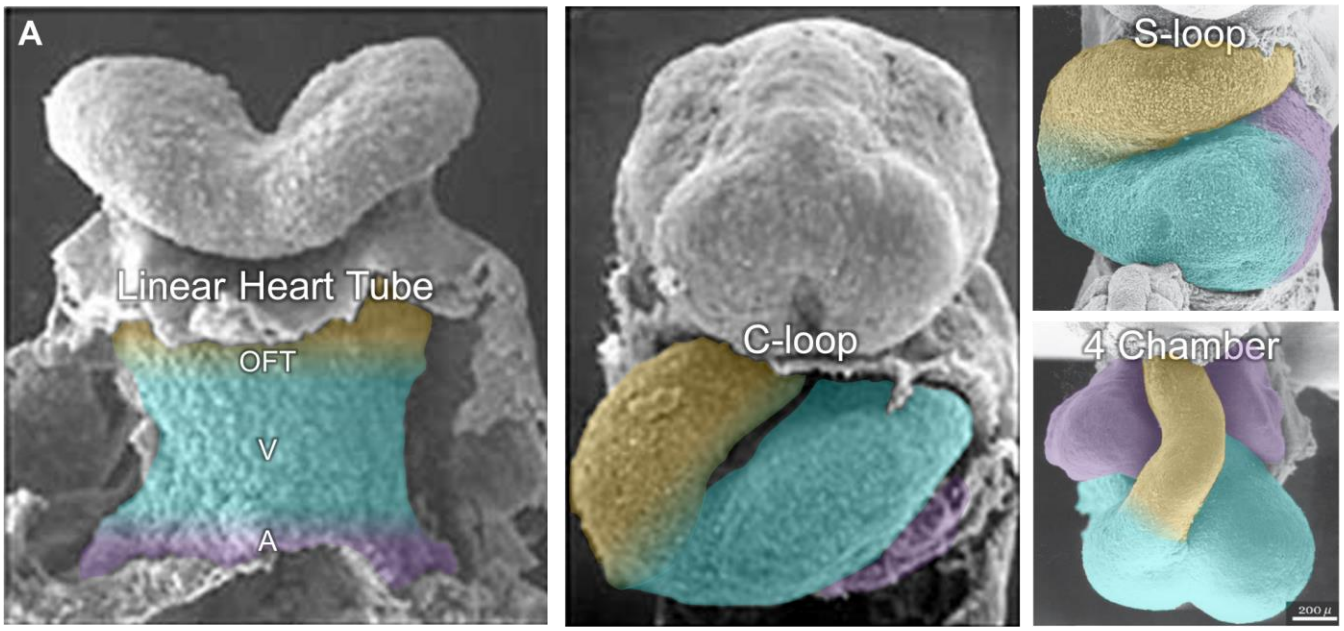

B

Comparative Development	Linear	C-loop	S-loop	4 Ch
Human (days)	22	24	28	33
Mouse (days)	8	8.5	9.5	12
Chicken (days)	1.5	2	2.25	3
Human (Carnegie stage)	10	11	12	14
Mouse (Thieler stage)	13	14	15	17
Chicken (HH stage)	10	13	16	18

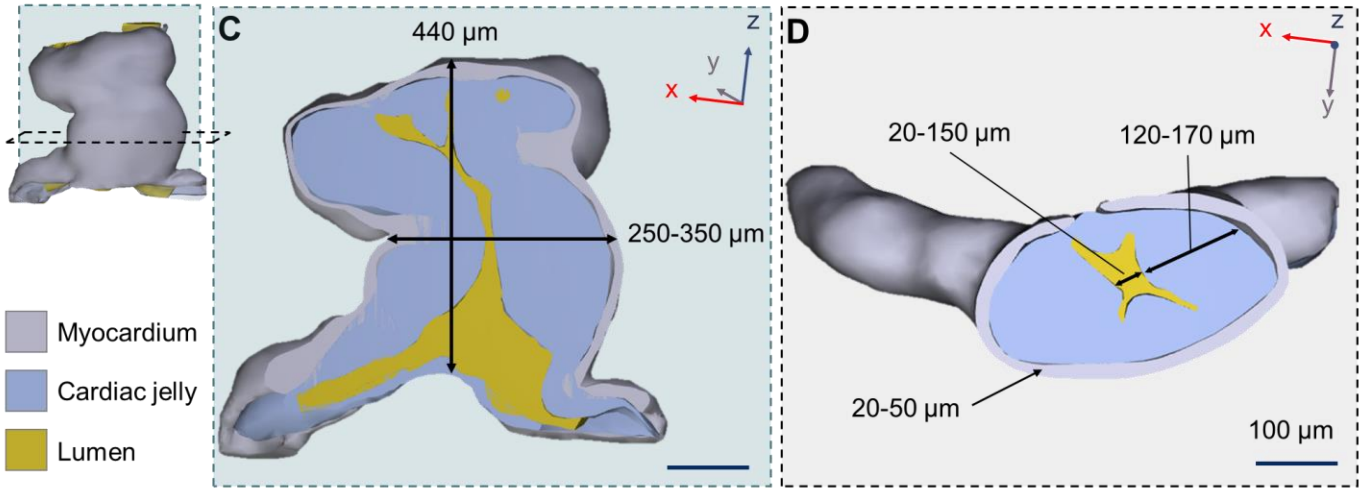

Figure 1.1. Human heart tube morphogenesis. (A) SEM images of the developing human heart tube from linear hear tube, C-looped, S-looped, and four-chambered heart (4 ch, bottom right). Future outflow tracts (OFT; yellow), ventricles (V; blue), and atria (A; purple) are color coded to highlight the complex structural transition the heart tube undergoes during morphogenesis. Color coding is a rough anatomical estimation and not exact. Images of the linear and C-loop heart tube stages were adapted from UNSW Embryology (https://embryology.med.unsw.edu.au), and S-loop and 4 chamber stages were adapted from[89]. **(B)** Comparison of the heart's developmental timeline in different vertebrates with days post-fertilization and corresponding developmental stages using the Carnegie, Thieler, and Hamburger-Hamilton (HH) stages for each species. Comparisons were based on whole embryo developmental stages and do not always reflect the relative stages of cardiac development for each species. **(C)** 3D reconstruction of the human linear heart tube at stage 10 viewed with a Z-axis or longitudinal cross-section. Measurements of the tube's height and diameter from the outer-most myocardial walls are overlaid. **(D)** Y-axis or crosswise section of the linear heart tube and thickness ranges of the myocardial wall (grey), lumen (yellow), and cardiac jelly (blue) layers. In each reconstruction, the surrounding coelomic walls, foregut, or neural tubes are excluded for clarity. All reconstructions and overlaid measurements in **(C)** and **(D)** are adapted with permission from the 3D Atlas of Human Embryology (specimen 6330)[87]. Multiple (n=5) measurements of each structure were taken along the z-axis from each cross-sectional view plane in (C) and (D) to create a range of size values. Measurements were taken from a 3D-rendered PDFs using the snap-to-edge tool which is not as accurate as using more precise 3D rendering software but are provided to give an approximate range.

1.3.2 Ventricular Tissue Architecture and Function

The heart is a never-resting pump that is responsible for efficiently moving blood out of the ventricles, through the lungs for oxygenation, and out through the extensive vascular network to deliver oxygen and nutrients to the body. To perform its function, the heart has developed over hundreds of millions of years to exhibit a unique pumping function where during contraction or systole, the muscle fibers shorten, thicken in diameter, and elicit a twisting motion of the whole organ. This twisting motion is like the wringing of a towel or the winding of a spring and is critical for suitable ejection of blood from the ventricles and therefore proper heart function (ejection fraction = 50-60%). Subsequently, when the mechanics of this motion are disrupted by disease or injury, heart function is compromised. For example, myocardial disarray is associated with several forms of cardiomyopathy (e.g. dilated or hypertrophic) and are often accompanied by fibrotic scaring throughout the muscle, even without an ischemic injury[90,91].

The heart's torsional motion is afforded by the distinctive double helical pattern of myofibrils throughout the thickness of the myocardium (**Figure 1.2**), where the orientation of muscle fibers exhibits a shift from a right-handed to a left-handed helix from the epicardium to the endocardium[92]. Relative to the short axis of the heart, the fibers are orientated starting at -60° on the epicardial surface and shift to a +60° at the endocardial surface (**Figure 1.2.A**)[93,94]. In other words, the fibers in the mid wall are oriented circumferentially (0°) and the fibers of the epicardium spiral downward toward the apex whereas the endocardial fibers spiral upwards toward the base of the heart. The majority (~53-59%) of the myocardial thickness is circumferentially oriented in the midwall whereas the epicardial (~25%) and endocardial (>20%) layers exhibit the greatest range

of directional change[91]. The change in fiber angle changes transmurally every four to five layers or sheets of myocytes, called myolaminae, and are separated by cleavage planes of perimysial collagen (**Figure 1.2.B**)[94]. The planes of perimysial collagen ensheathe the myolaminae and bear the shearing forces that occur between the differently angled fibers during contraction and relaxation[91].

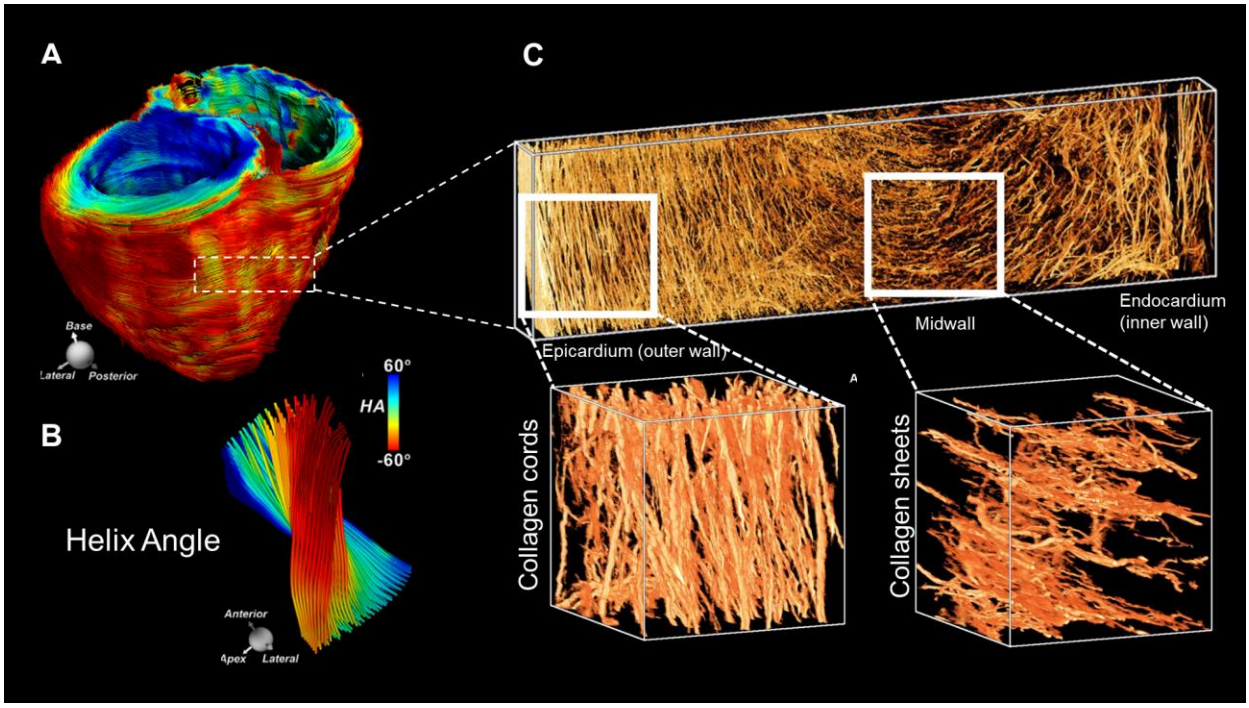

Figure 1.2. Helical myocardial organization. (A) Diffusion tensor magnetic resonance image (DT-MRI) of the adult human heart with the left ventricle forward facing. **(B)** Magnified section of the left ventricle myocardium demonstrating the shifting myofibril orientation angles within the myocardium. **(A)** and **(B)** were adapted from[92]. **(C)** Transmural 3D projections of the perimysial collagen network within the left ventricle myocardium. Inset images are magnified 3D sections of the perimysial collagen near the epicardium or midwall demonstrating differences in collagen bundling as cords or sheets, respectively. Adapted from[94].

Within each myolaminae, the cardiomyocytes are also ordered end-to-end and elongate in the direction of the collagen fibrils within the cleavage planes (**Figure 1.3.A & B**). Intercalated discs are formed between the ends of the connecting myocytes where desmosome and adherens junctions are used to tightly connect the cells together[95]. Intermediate and actin filaments within each cell also anchor onto and radiate from desmosomes and adherens junctions, respectively, to provide structural support and organization within the cytoskeleton and the contractile machinery of the sarcomere (**Figure 1.3.C & D**). Additionally, porous gap junctions are formed at the intercalated discs and connect the cytoplasm of neighboring cells together. Gap junctions and their ordered arrangement between myocytes are critical for fast propagation of action potentials by allowing the flow of ions (mainly Ca^{2+}) through the connected cells[96]. The end-to-end organization of cardiomyocytes and flow of ions through gap junctions facilitates the fast propagation of action potentials, and subsequently contraction, along the direction of the cellular alignment. Contraction patterns across the myocardium are ultimately orchestrated by electrical pulses from the pacemaker cells in the sinoatrial (SA) and atrioventricular (AV) nodes, which are innervated the parasympathetic and sympathetic nervous system to control the heart's beating rate[97]. The pulses from the pacemaker nodes are time-delayed such that the electrical signal propagates from the SA node to the AV node and along the Purkinje fibers which conduct the depolarization wave from the apex to the base of the heart. Contraction of the myocardium from apex to base elicits the twisting and squeezing motion of the heart to eject blood from the bottom of the ventricles and out towards to base and through the pulmonary artery and aorta.

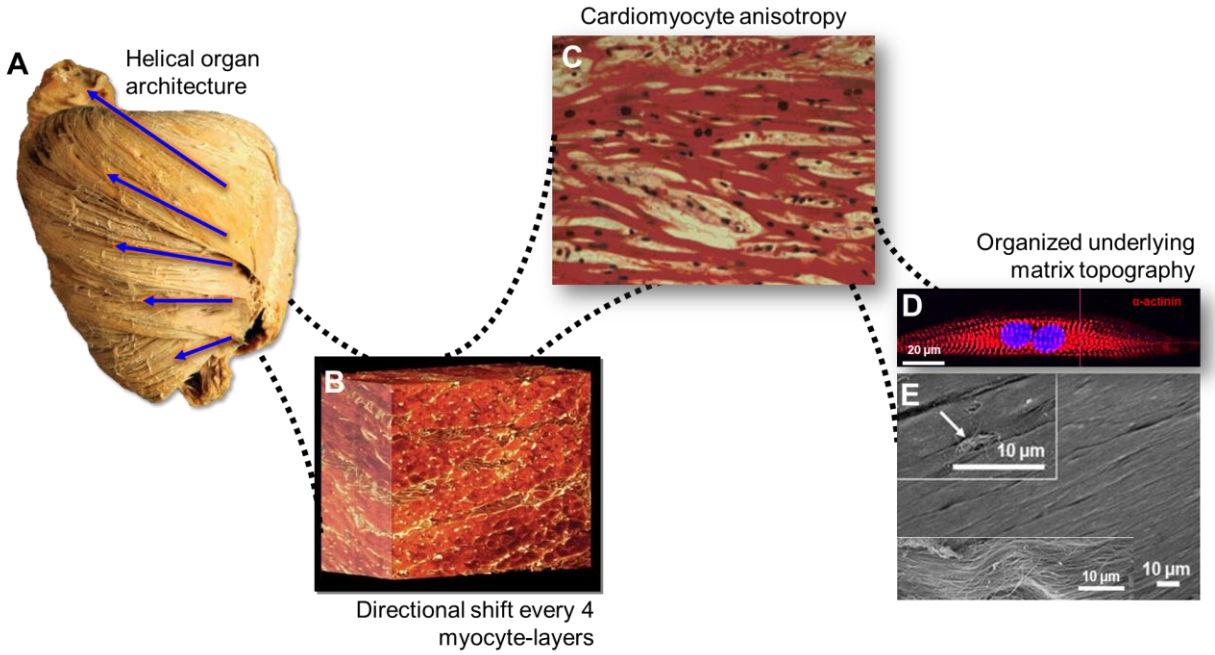

Figure 1.3. Complex multi-scale organization of the heart. (A) Decellularized canine heart dissected to reveal helical myocardial architecture. Adapted from[98]. **(B)** 3D projection confocal image of the rat ventricular myocardium highlighting layers of muscle sheets known as myolaminae. Adapted from[94]. **(C)** Histological section of myolaminae showing cardiomyocyte organization and connection within a single directional plane. Adapted from[98]. **(D)** Human iPSC-CM seeded on nanotopographical scaffolds has highly organized contractile machinery as demonstrated by ordered patterns of sarcomere proteins, α-actinin (red), surrounding two nuclei (DAPI, blue). **(E)** Scanning electron microscopy image of the rat myocardium demonstrating organized bundles of perimysial collagen fibers (inset). (D) and (E) were adapted from[99].

1.3.3 Evolution of Helical Myocardial Patterning

The counter-directional pattern of a helix is more energetically favorable and required to uniformly redistribute stresses and strain across the myocardium during systole as opposed to models where fibers are solely organized in a single direction [100,101]. Advantageous helical patterning of muscles has also been described in other vertebrates such as the body walls of the *Dermophis mexicanus*, a limbless amphibian, or species of acoelomate worms [102,103]. Helical patterns allow for more degrees of freedom in motion as the pitch angle between the counter-angled muscle fibers decreases with contraction and increases with relaxation, like the opening and closing angle of a pair of shears[103]. In the heart, the pitch angle between fibers decreases during systole such that the majority of the fibers are all circumferentially aligned (0°) around the ventricles' lumens[104].

Morphogenesis and patterning of the heart are conserved across vertebrates[105]. However, the mechanism through which the heart folds itself into a four-chambered structure while also developing helical myocardial patterning is poorly understood[106]. As the heart tube is forming in early embryonic development but before the first contractions occur, the cardiomyocytes and surrounding fibronectin matrix begin to organize into a circumferential pattern that encircles the heart tube's lumen[107,108]. Almost immediately after contraction begins, the heart tube begins it asymmetrical rightward C-looping (**Figure 1.1.A**). These observations suggest that the initial looping movements may be caused by twisting motions in the heart tube and might set up initial patterns of shear forces and strain for further helical development. Additionally, through diffusion tensor magnetic resonance imaging (DT-MRI) of fetal and adult hearts, the myocardial structure of the 10-week-old fetal heart is still predominantly circumferential in organization and

further develops helical patterning between 14-19 weeks of gestation and continues to evolve after birth[109]. However, it is unclear as to what happens in the heart tube to cause this initial twisting force in the first place[106].

Further investigation into the cardiac development is required to answer fundamental questions of myocardial patterning. However, there is already a great body of research surrounding heart morphogenesis that has been informed by over two centuries of studies in several species (e.g., chicken, mouse, human embryo)[15]. Animal models have provided a wealth of biological information on the most primitive structures of the developing heart through cell-fate mapping studies, histological sectioning, and three-dimensional (3D) reconstructions[7,110]. However, given the ethical concerns of studying human embryos, many aspects that govern the morphological development of the human heart remain unknown. Comparative biology has provided a window through which analogous heart morphogenesis can be observed but it has a limited capacity to precisely mirror human biology[111]. Therefore, there is a need to develop human models of heart development that allow for examination of innate cellular behavior and their contribution to cardiac morphogenesis and function. It is possible that cardiac tissue engineering approaches could provide a unique advantage to interrogate human development if combined with human iPSC-derived cardiac progenitors[85].

1.4 Multi-scale Cardiac Tissue Engineering Techniques

The heart has multi-scale organization that gives rise to its uniquely helical muscle architecture and twisting contractile pattern, as discussed

extensively above. This hierarchical structure is critical to the heart's proper function and when compromised can lead to disease and often organ failure. Given the importance of these structure-function relationships within the heart, it is logical to assume that their recapitulation within an engineered tissue system would be advantageous, or even required, to adequately assess cardiac function *in vitro.* However, recreating these complex structures on both the macro- and microscopic levels using even modern tissue engineering approaches has proven to be non-trial. Nonetheless, there have been great advancements in cardiac tissue engineering approaches to model several aspects of the functioning myocardium for study of cardiovascular development, biology, and disease.

1.4.1 Recapitulating Nano- and Microscale Cues

Within the myolaminae, sheets of cardiomyocytes are ordered end-to-end and elongate in the direction of similarly ordered perimysial collagen fibrils (**Figures 2B**). The adherence of the myocytes to the aligned collagen fibrils are known to act as a nanoscale organizational cue with the diameter of collagen bundles varying between 30 and 300 nm (**Figure 2E**)[112]. The myocytes and other cell types within the heart (e.g fibroblasts, smooth muscle, and endothelial cells) secrete and remodel this matrix, form focal adhesions with it, and align with its principle direction; potentially creating a positive feedback loop of structural organization[113]. Recapitulating these topographical alignment cues within an *in*

vitro system has been a core principle of many cardiac tissue engineering approaches. By controlling the composition and organization of underlying matrix topography, cellular organization and potentially functional output can be studied under defined conditions. For example, nanoscale ridge-groove features can be recreated using capillary force lithography techniques that can guide cellular alignment on 2D substrates[80,99,114–116]. When seeded with iPSC-CMs, the cells elongate in the direction of the nano ridge-groove pattern and with long-term culture (>65 days) begin to exhibit cellular width-length aspect ratios that near adult cardiomyocytes[117]. In this example, by encouraging myocyte alignment through focal adhesion organization, the cytoskeleton and contractile machinery can also be organized and further promote iPCS-CM maturation such that late on-set phenotype of dystrophic cardiomyopathy could be recapitulated.

Like nanoscale topography, microscale cues can be used to dictate cardiomyocyte organization in several ways. A popular approach is to confine cellular surface adhesions to different geometric shapes or patterns to control cellular aspect ratio and alignment[118,119]. The approaches work by patterning or stamping extracellular matrix (ECM) proteins such as fibronectin, laminin, or collagen onto a hydrophobic surface that encourages cell binding to only the protein-rich areas where cells can form focal adhesions. This approach can be used to confine single cells or monolayers into functionally advantageous organizations such as tissue strips or strain-sensing cantilevers[120,121]. This approach is particularly advantageous for studying the biomechanics of organized cardiac monolayers and even their force production with application of drug compounds[122].

Electrospinning has also become a popular approach for creating organized nano- and microscale matrix topographies for both 2D monolayer cultures[123]. In this technique, a polymer is dissolved in a liquid solvent and extruded from a nozzle onto a rotating collector, like a drum or rod, such that the polymer is pulled into strands of nano- or micrometer widths and the solvent is evaporated. By controlling the extrusion speed and the rotation speed, distance, angle, etc. of the collector, highly organized, large area (cm^2) scaffolding can be fabricated quickly. Additionally, the polymer makeup is highly tunable and can be made from synthetic or naturally derived biomatierals such as poly caprolactone or collagen, respectively. The composition can be tuned to match myocardial stiffnesses and organization as to recreate a microenvironment that is more biomimetic of native cardiac tissue.

1.4.2 Three-Dimensional Cardiac Tissue Engineering Approaches

Engineering functional monolayers of cardiac tissues has provided great advancement over conventional *in vitro* culture assays for applications in disease modeling and drug screening[79,80]. However, 2D models of cardiac tissue cannot ascertain how individual cellular behavior might affect larger 3D tissue function at the macroscopic level. To address this concern, there has been a large thrust in the cardiac tissue engineering field to develop novel methods for building cell dense, highly functional, 3D tissues[124]. The simplest evolution from 2D monolayers to 3D tissues, is to increase the number of cell layers in the z-dimension and release the tissue from the laminar confinement of the tissue culture dish. For example, cardiac patches with multiple cell layers of interconnected cells have been fabricated by first seeding multiple layers of

cardiomyocytes onto temperature responsive substrates and allowing them to from a syncytium with coordinated contractions. Second, the cardiac monolayers were then detached from the thermoresponsive scaffolding below by lowering the temperature of the culture bath. Finally, the cell sheets could then be layered on top of additional cell layers to create a tissue that was twice as thick. This process was repeated several times to fabricate dense, functional cardiac patches[125,126]. To fabricate more complex and biomimetic tissue geometries, contractile sheets could be rolled or casted into 3D tubular geometries with hollow lumens[127,128]. Additionally, the intraluminal pressure generated with each contraction of the cardiac sheets could be recorded using pressure-sensing catheters[127].

Tissue casting has become a widely used approach for creating 3D, functional cardiac tissues with relatively high throughput and reproducibility. In these approaches, a mixture of hydrogel material, such as fibrin or collagen, and iPSC-CMs are poured into a custom mold that confines the cells-in-gel mixture to polymerize into a desirable shape [129,130]. For example, Zhang and colleges developed 7 x 7 mm^2 polydimethylsiloxane (PDMS) molds with staggered hexagonal posts to fabricated cardiac patches from hESC-CMs and a mixture of fibrin and Matrigel matrix proteins[131]. Cells encapsulated in the polymerized hydrogel mixture were able to remodel and compact the surrounding matrix around the hexagonal posts to create a contractile tissue patch with oval-shaped holes. Due to the oblong shape of the hexagonal posts, the cells were forced to align with a strong axis of tension in the longitudinal direction leading to a global tissue organization. This approach yielded more mature cardiomyocytes with near physiological sarcomere lengths (1.9 – 2.3 μm), ratios of β-MHC:α-MHC expression (0.7), and contractile conduction velocities

(25.1 cm/sec) compared to that of traditional monolayer controls (1.5 – 1.9 μm, <0.1, and 19.5 cm/s, respectively). These phenotypic characteristics were great achievements over the existing cardiac tissue engineering platforms, but these values were still far from those of fetal or adult tissues[71].

Recently, a seminal study by K. Ronaldson-Bouchard and colleges developed tissue fabrication and culture protocols that yielded 3D engineered heart tissue (EHT) strips with the most advanced maturation obtained from an engineered system to date [23]. This approach utilized a tissue casting scheme which allowed cells in a hydrogel matrix to compact around two posts, one that is ridged and one that is flexible and can measure force deflections during contraction. This approach that was not new to the field [132], but they incorporated an electrical pacing protocol that challenged the tissues to contract and relax at increasingly faster frequencies over time. They found that in combination with relatively young cardiomyocytes (12 days since induction of differentiation), this intensity training scheme could produce cardiac tissues with phenotypic characteristics that were equivalent or even superior to fetal cardiac tissues. For example, intensity trained tissues had 30-35% of the cell volume occupied by mitochondria and could utilize fatty acids for metabolism, which is a hallmark of adult cardiac tissues whose metabolic demand is extremely high. Additionally, these tissues demonstrated extensive T-tubule invaginations and mature calcium-handling properties with positive ionotropic, lusitropic, and chronotropic responses to known drug compounds.

These studies have provided some of the most advanced tissue engineering platforms for the study of cardiac tissue mechanics[132], disease modeling[133], and drug testing[134,135]. However, these approaches are limited in their capacity to model organ level tissue

responses due to their relatively simplistic laminar or cylindrical shapes. These approaches would need to incorporate vascular networks and pro-angiogenic factors to surpass the physical limitations of natural nutrient and oxygen diffusion. This has also proven to be a challenging task and is actively being pursued across all areas of tissue engineering[120,126,136,137].

1.4.3 Engineering Cardiac Ventricular Geometries

There are few examples of tissue engineering approaches that have been used to recreate heart ventricle-like tissue geometries but the number of research groups attempting this has been on the rise. One relatively simple but high throughout approach is to utilize tissue casting techniques as described previously but incorporating negative and positive molds as to create lumens within a tissue[130,138]. For example, E.J. Lee and colleges created a reservoir that a cells and hydrogel mixture could be poured into and then an inflated balloon, like a balloon catheter, was inserted into the well and allowed the tissue to compact around the balloon[130]. After compaction, the balloon could be deflated and removed leaving behind a contractile hollow tissue that was then sutured onto the end of a flexible tube through which pressure-volume relationships could be assessed. This is a marked improvement over the 2D or laminar 3D tissue strips described previously. In this case, the contribution of cellular contraction to tissue-level function can be evaluated in a physiologically relevant manner. However, the global cellular organization of these tissues was isotropic and only showed some level of local organization.

More advanced approaches, such as electrospinning[139] or freeform reversible embedding of suspended hydrogels (FRESH)[140,141], have been employed to incorporate ventricular geometries with local and global tissue anisotropy. For example, L. MacQueen and colleges utilized electrospinning to collect collagen fibers onto a tapered or bullet-shaped collector to produce an anisotropic scaffolding for seeding iPSC-CMs[139]. Once incorporated, the cardiomyocytes elongated in the direction of the circumferentially aligned collagen fibers and penetrated through to create wall thicknesses three to four cell layers thick. These models could also create small pressures (0.04 mmHg) when measured with a pressure-volume catheter. However, the deformations were small relative to the size of the ventricle model and required an external pressure assist device to achieve inward tissue deformations when observed with ultrasound. Incorporation of more cells or softer scaffolding will be required to achieve greater pressure production.

Bioprinting approaches or FRESH techniques have been used to “print” cell-laden tissues or scaffolding that recreate real organ tissue structures by using 3D-rendered MRI scans of the human heart[141]. This approach offers distinct advantages over tissue casting or electrospinning approaches where intricate and hollow features can be recreated throughout a structure, such as the coronary vasculature or heart valves. However, these structures are still only capable of producing pressures or deformations that are only a small fraction of the human heart, relative to the cell number and tissue size. Nonetheless, three highlighted achievements have only been possible over the past seven years or less with the invention or application of new technologies for tissue engineering. The level of size, complexity, and function will only continue to increase as more efforts are put towards the goal of engineering more biomimetic tissues for endless applications.

1.5 Unmet Needs and Future Perspectives

Despite the great advancements detailed in this review, there is still a dire need for tissue engineering approaches that can restore failing heart function and accurately recapitulate characteristics of mature myocardium. With current tissue engineering approaches, it is difficult to ascertain how cellular-level function contributes to macroscopic heart function or failure. These shortcomings are likely due to their over-simplified configurations that offer a foreign extracellular environment and thus provoke a cellular response that is unrepresentative of their *in vivo* function. It is possible that for engineered cardiac tissues to accurately represent cardiac function and potentially gain physiological maturity, they may also need to incorporate structural cues that promote multiscale myocardial architecture, including helical fiber organization and the conical geometry of the heart's ventricles. There has been a targeted focus on developing bioengineering strategies for recreating native myocardial architectures, but still after almost three decades of progress there few approaches that can begin to incorporate micro- and macroscopic organization. In time, as biological questions inspire and precipitate technological advancements to answer them, this will lead to a deepened understanding of myocardial function in the context of development, health, and disease. In turn, this comprehension will likely lead to more physiologically representative models of the myocardium and provide immeasurable downstream applications.

1.6 Dissertation Specific Aims

The overarching goal of the research presented in this dissertation was to engineer the most biomimetic ventricular model to date by leveraging human iPSC-CMs, cardiac cell-sheet engineering, and 3D tissue fabrication. We sought to investigate the effects of tissue architecture on ventricular function using physiologically relevant endpoints such as pumping function. This was accomplished by pursuing the following specific aims:

Aim 1: Establish a robust biofabrication method for engineering 3D tissue models using nanopatterned cell-sheet stacking technology.

Tissues throughout the body have multiscale organization that dictates their biology and function. It was hypothesized that nanopatterned cell sheet stacking technology will allow for fabrication of functional multilayered 3D cardiac ventricular models with controllable architectures. To test this hypothesis, we developed novel flexible thermoresponsive nanofabricated substrates (fTNFS) for anisotropic cell-sheet engineering, layering, and casting to fabricate 3D tissue structures. We validated this approach by circumferentially patterning smooth, skeletal, and cardiac muscle in hollow tubular tissues. Tissues were examined for their cellular organization after several days in culture through immunocytochemistry and confocal microscopy.

Aim 2: Investigate structure-function relationships in 3D cardiac ventricular models.

We hypothesized that implementing anisotropic tissue architecture resembling the organization present within native myocardium within a cardiac tissue model will lead to

greater functionality compared to unrepresentative tissue structures. To test this hypothesis, the methods developed in Aim 1 were adapted to fabricate 3D organized cardiac ventricular models using hiPSC cardiomyocytes and endothelial cells and custom ventricular molds. Ventricular models with circumferential, angled, longitudinal, and isotropic tissue architectures were fabricated and characterized their cellular organization after several days in culture. We further evaluated the structure-function relationships of each configuration through catheterization and measurement of isovolumic pressure production and maximum capture rates with increasing electrical pacing frequencies.

1.7 References

1. Institute for Health Metrics and Evaluation. *Global Burden of Disease Comparison Tool* http://www.healthdata.org/results/country-profiles.
2. Laflamme, M. A. & Murry, C. E. Heart regeneration. *Nature* **473**, 326–35 (2011).
3. Benjamin, E. J. *et al. Heart Disease and Stroke Statistics-2019 Update: A Report From the American Heart Association*. *Circulation* vol. 139 (2019).
4. Tzahor, E. & Poss, K. D. Cardiac regeneration strategies: Staying young at heart. *Science* vol. 356 1035–1039 (2017).
5. Godwin, J. W., Debuque, R., Salimova, E. & Rosenthal, N. A. Heart regeneration in the salamander relies on macrophage-mediated control of fibroblast activation and the extracellular landscape. *npj Regen. Med.* **2**, 1–11 (2017).
6. Poss, K. D., Wilson, L. G. & Keating, M. T. Heart regeneration in zebrafish. *Science (80-.).* **298**, 2188–2190 (2002).
7. Günthel, M., Barnett, P. & Christoffels, V. M. Development, Proliferation, and Growth of the Mammalian Heart. *Mol. Ther.* **26**, 1599–1609 (2018).
8. Takasato, M. *et al.* Directing human embryonic stem cell differentiation towards a renal lineage generates a self-organizing kidney. *Nat. Cell Biol.* **16**, 118–126 (2014).
9. Paradis, A. N., Gay, M. S. & Zhang, L. Binucleation of cardiomyocytes: The transition from a proliferative to a terminally differentiated state. *Drug Discovery Today* vol. 19 602–609 (2014).

10. Miko, M. *et al.* Two nuclei inside a single cardiac muscle cell. More questions than answers about the binucleation of cardiomyocytes. *Biol.* **72**, 825–830 (2017).

11. Bergmann, O. *et al.* Evidence for cardiomyocyte renewal in humans. *Science (80-.).* **324**, 98–102 (2009).

12. Leenaars, C. H. C. *et al.* Animal to human translation: A systematic scoping review of reported concordance rates. *Journal of Translational Medicine* vol. 17 223 (2019).

13. DiMasi, J. A., Grabowski, H. G. & Hansen, R. W. Innovation in the pharmaceutical industry: New estimates of R&D costs. *J. Health Econ.* **47**, 20–33 (2016).

14. Van Der Worp, H. B. *et al.* Can Animal Models of Disease Reliably Inform Human Studies? doi:10.1371/journal.pmed.1000245.

15. Wallingford, J. B. The 200-year effort to see the embryo. *Science (80-.).* **365**, 758–759 (2019).

16. Tzatzalos, E., Abilez, O. J., Shukla, P. & Wu, J. C. Engineered heart tissues and induced pluripotent stem cells: Macro- and microstructures for disease modeling, drug screening, and translational studies. *Advanced Drug Delivery Reviews* vol. 96 234–244 (2016).

17. Smith, A. S. T., Macadangdang, J., Leung, W., Laflamme, M. A. & Kim, D.-H. Human iPSC-derived cardiomyocytes and tissue engineering strategies for disease modeling and drug screening HHS Public Access. *Biotechnol Adv* **35**, 77–94 (2017).

18. Ferri, N. *et al.* Drug attrition during pre-clinical and clinical development: Understanding and managing drug-induced cardiotoxicity. *Pharmacology and Therapeutics* vol. 138 470–484 (2013).

19. Redfern, W. S. *et al.* Relationships between preclinical cardiac electrophysiology, clinical QT interval prolongation and torsade de pointes for a broad range of drugs: Evidence for a provisional safety margin in drug development. *Cardiovascular Research* vol. 58 32–45 (2003).

20. Colatsky, T. *et al.* The Comprehensive in Vitro Proarrhythmia Assay (CiPA) initiative — Update on progress. *J. Pharmacol. Toxicol. Methods* **81**, 15–20 (2016).

21. Takahashi, K. & Yamanaka, S. Induction of Pluripotent Stem Cells from Mouse Embryonic and Adult Fibroblast Cultures by Defined Factors. *Cell* **126**, 663–676 (2006).

22. Kattman, S. J., Adler, E. D. & Keller, G. M. Specification of Multipotential Cardiovascular Progenitor Cells During Embryonic Stem Cell Differentiation and Embryonic Development. *Trends Cardiovasc. Med.* **17**, 240–246 (2007).

23. Ronaldson-Bouchard, K. *et al.* Advanced maturation of human cardiac tissue grown from pluripotent stem cells. *Nature* **556**, 239–243 (2018).

24. Lucey, B. P., Nelson-Rees, W. A. & Hutchins, G. M. *HeLa Cells and Cell Culture Contamination-Lucey et al 1463*. *Arch Pathol Lab Med* vol. 133 (2009).

25. Burridge, P. W., Keller, G., Gold, J. D. & Wu, J. C. Production of de novo cardiomyocytes: Human pluripotent stem cell differentiation and direct reprogramming. *Cell Stem Cell* vol. 10 16–28 (2012).

26. Kane, N. M. *et al.* Pluripotent stem cell differentiation into vascular cells: A novel technology with promises for vascular re(generation). *Pharmacology and Therapeutics* vol. 129 29–49 (2011).

27. Choi, K. D. *et al.* Identification of the Hemogenic Endothelial Progenitor and Its Direct Precursor in Human Pluripotent Stem Cell Differentiation Cultures. *Cell Rep.* **2**, 553–567 (2012).

28. Kennedy, M. *et al.* T Lymphocyte Potential Marks the Emergence of Definitive Hematopoietic Progenitors in Human Pluripotent Stem Cell Differentiation Cultures. *Cell Rep.* **2**, 1722–1735 (2012).

29. Panula, S. *et al.* Human germ cell differentiation from fetal-and adult-derived induced pluripotent stem cells. doi:10.1093/hmg/ddq520.

30. Ghodsizadeh, A. *et al.* Generation of Liver Disease-Specific Induced Pluripotent Stem Cells Along with Efficient Differentiation to Functional Hepatocyte-Like Cells. *Stem Cell Rev. Reports* **6**, 622–632 (2010).

31. Carri, A. D. *et al.* Developmentally coordinated extrinsic signals drive human pluripotent stem cell differentiation toward authentic DARPP-32+ medium-sized spiny neurons. *Dev.* **140**, 301–312 (2013).

32. Mizuno, Y. *et al.* Generation of skeletal muscle stem/progenitor cells from murine induced pluripotent stem cells. *FASEB J.* **24**, 2245–2253 (2010).

33. Bilousova, G. *et al.* Osteoblasts Derived from Induced Pluripotent Stem Cells form Calcified Structures in Scaffolds Both In Vitro and In Vivo. *Stem Cells* **29**, 206–216 (2011).

34. Andersen, P. *et al.* Precardiac organoids form two heart fields via Bmp/Wnt signaling. *Nat. Commun.* **9**, 3140 (2018).

35. Hinson, J. T. *et al.* Titin mutations in iPS cells define sarcomere insufficiency as a cause of dilated cardiomyopathy. *Science (80-.).* **349**, 982–986 (2015).

36. Liang, P. *et al.* Drug screening using a library of human induced pluripotent stem cell-derived cardiomyocytes reveals disease-specific patterns of cardiotoxicity. *Circulation* **127**, 1677–1691 (2013).

37. Liu, Y.-W. *et al.* Human embryonic stem cell–derived cardiomyocytes restore function in infarcted hearts of non-human primates. *Nat. Biotechnol.* **36**, 597–605 (2018).

38. Barreto, S., Hamel, L., Schiatti, T., Yang, Y. & George, V. Cardiac Progenitor Cells from Stem Cells: Learning from Genetics and Biomaterials. *Cells* **8**, 1536 (2019).

39. Richards, D. J. *et al.* Inspiration from heart development: Biomimetic development of functional human cardiac organoids. *Biomaterials* **142**, 112–123 (2017).

40. Fatehullah, A., Tan, S. H. & Barker, N. Organoids as an in vitro model of human

development and disease. *Nature Cell Biology* vol. 18 246–254 (2016).

41. Ma, Z. *et al.* Self-organizing human cardiac microchambers mediated by geometric confinement. *Nat. Commun.* **6**, 7413 (2015).

42. Voges, H. K. *et al.* Development of a human cardiac organoid injury model reveals innate regenerative potential. *Development* **144**, 1118–1127 (2017).

43. Park, I.-H. *et al.* Disease-Specific Induced Pluripotent Stem Cells. doi:10.1016/j.cell.2008.07.041.

44. Dick, E. *et al.* Exon Skipping and Gene Transfer Restore Dystrophin Expression in Human Induced Pluripotent Stem Cells-Cardiomyocytes Harboring *DMD* Mutations. *Stem Cells Dev.* **22**, 2714–2724 (2013).

45. Lin, B. *et al.* Modeling and study of the mechanism of dilated cardiomyopathy using induced pluripotent stem cells derived from individuals with Duchenne muscular dystrophy. *Dis. Model. Mech.* **8**, 457–66 (2015).

46. Guan, X. *et al.* Dystrophin-deficient cardiomyocytes derived from human urine: New biologic reagents for drug discovery. *Stem Cell Res.* **12**, 467–480 (2014).

47. Kim, Y. G., Cha, J. & Chandrasegaran, S. Hybrid restriction enzymes: Zinc finger fusions to Fok I cleavage domain. *Proc. Natl. Acad. Sci. U. S. A.* **93**, 1156–1160 (1996).

48. Christian, M. *et al.* Targeting DNA double-strand breaks with TAL effector nucleases. *Genetics* **186**, 756–761 (2010).

49. Mali, P. *et al.* RNA-guided human genome engineering via Cas9. *Science (80-.).* **339**, 823–826 (2013).

50. Young, C. S. *et al.* A Single CRISPR-Cas9 Deletion Strategy that Targets the Majority of DMD Patients Restores Dystrophin Function in hiPSC-Derived Muscle Cells. *Cell Stem Cell* **18**, 533–540 (2016).

51. Mosqueira, D. *et al.* CRISPR/Cas9 editing in human pluripotent stem cell-cardiomyocytes highlights arrhythmias, hypocontractility, and energy depletion as potential therapeutic targets for hypertrophic cardiomyopathy. doi:10.1093/eurheartj/ehy388.

52. Ben Jehuda, R., Shemer, Y. & Binah, O. Genome Editing in Induced Pluripotent Stem Cells using CRISPR/Cas9. *Stem Cell Reviews and Reports* vol. 14 323–336 (2018).

53. Smith, J. G. W. *et al.* Isogenic Pairs of hiPSC-CMs with Hypertrophic Cardiomyopathy/LVNC-Associated ACTC1 E99K Mutation Unveil Differential Functional Deficits. *Stem Cell Reports* **11**, 1226–1243 (2018).

54. Kilpinen, H. *et al.* Common genetic variation drives molecular heterogeneity in human iPSCs. *Nature* **546**, 370–375 (2017).

55. Leung, D. G. *et al.* Sildenafil does not improve cardiomyopathy in Duchenne/Becker muscular dystrophy. *Ann. Neurol.* **76**, 541–9 (2014).

56. Park, S. *et al.* A Comprehensive, Ethnically Diverse Library of Sickle Cell Disease-

Specific Induced Pluripotent Stem Cells. *Stem Cell Reports* **8**, 1076–1085 (2017).

57. Pashos, E. E. *et al.* Large, Diverse Population Cohorts of hiPSCs and Derived Hepatocyte-like Cells Reveal Functional Genetic Variation at Blood Lipid-Associated Loci. *Cell Stem Cell* **20**, 558-570.e10 (2017).

58. Germain, P. L. & Testa, G. Taming Human Genetic Variability: Transcriptomic Meta-Analysis Guides the Experimental Design and Interpretation of iPSC-Based Disease Modeling. *Stem Cell Reports* **8**, 1784–1796 (2017).

59. Streeter, I. *et al.* The human-induced pluripotent stem cell initiative-data resources for cellular genetics. *Nucleic Acids Res.* **45**, 691–697 (2016).

60. Carcamo-Orive, I. *et al.* Analysis of Transcriptional Variability in a Large Human iPSC Library Reveals Genetic and Non-genetic Determinants of Heterogeneity. *Cell Stem Cell* **20**, 518-532.e9 (2017).

61. Hartman, M. E., Dai, D. F. & Laflamme, M. A. Human pluripotent stem cells: Prospects and challenges as a source of cardiomyocytes for in vitro modeling and cell-based cardiac repair. *Advanced Drug Delivery Reviews* vol. 96 3–17 (2016).

62. Shiba, Y. *et al.* Human ES-cell-derived cardiomyocytes electrically couple and suppress arrhythmias in injured hearts. *Nature* **489**, 322–325 (2012).

63. Guo, R. *et al.* Stem cell-derived cell sheet transplantation for heart tissue repair in myocardial infarction. *Stem Cell Research and Therapy* vol. 11 19 (2020).

64. Laflamme, M. A. *et al.* Cardiomyocytes derived from human embryonic stem cells in pro-survival factors enhance function of infarcted rat hearts. *Nat. Biotechnol.* **25**, 1015–1024 (2007).

65. Ieda, M. *et al.* Direct reprogramming of fibroblasts into functional cardiomyocytes by defined factors. *Cell* **142**, 375–386 (2010).

66. Serpooshan, V. & Wu, S. M. Patching up broken hearts: Cardiac cell therapy gets a bioengineered boost. *Cell Stem Cell* vol. 15 671–673 (2014).

67. Miyagawa, S. *et al.* Phase I Clinical Trial of Autologous Stem Cell–Sheet Transplantation Therapy for Treating Cardiomyopathy. *J. Am. Heart Assoc.* **6**, (2017).

68. Gao, L. *et al.* Large Cardiac Muscle Patches Engineered From Human Induced-Pluripotent Stem Cell–Derived Cardiac Cells Improve Recovery From Myocardial Infarction in Swine. *Circulation* **137**, 1712–1730 (2018).

69. Ye, L., Zimmermann, W.-H., Garry, D. J. & Zhang, J. Patching the Heart. *Circ. Res.* **113**, 922–932 (2013).

70. Romagnuolo, R. & Laflamme, M. A. Programming cells for cardiac repair. doi:10.1016/j.copbio.2017.05.011.

71. Yang, X., Pabon, L. & Murry, C. E. Engineering Adolescence Maturation of Human Pluripotent Stem Cell–Derived Cardiomyocytes. *Circ. Res.* **114**, 511–523 (2014).

72. Romagnuolo, R. *et al.* Human Embryonic Stem Cell-Derived Cardiomyocytes Regenerate the Infarcted Pig Heart but Induce Ventricular Tachyarrhythmias. *Stem*

Cell Reports **12**, 967–981 (2019).

73. Srivastava, D. & DeWitt, N. In Vivo Cellular Reprogramming: The Next Generation. *Cell* vol. 166 1386–1396 (2016).
74. Cao, N. *et al.* Conversion of human fibroblasts into functional cardiomyocytes by small molecules. *Science (80-.).* **352**, 1216–1220 (2016).
75. Song, K. *et al.* Heart repair by reprogramming non-myocytes with cardiac transcription factors. *Nature* **485**, 599–604 (2012).
76. Qian, L. *et al.* In vivo reprogramming of murine cardiac fibroblasts into induced cardiomyocytes. *Nature* **485**, 593–598 (2012).
77. Vagnozzi, R. J. *et al.* An acute immune response underlies the benefit of cardiac stem cell therapy. *Nature* **577**, 405–409 (2020).
78. O'Rourke, S. A., Dunne, A. & Monaghan, M. G. The Role of Macrophages in the Infarcted Myocardium: Orchestrators of ECM Remodeling. *Frontiers in Cardiovascular Medicine* vol. 6 101 (2019).
79. Macadangdang, J. *et al.* Nanopatterned Human iPSC-Based Model of a Dystrophin-Null Cardiomyopathic Phenotype. *Cell. Mol. Bioeng.* **8**, 320–332 (2015).
80. Smith, A. S. T., Macadangdang, J., Leung, W., Laflamme, M. A. & Kim, D. H. Human iPSC-derived cardiomyocytes and tissue engineering strategies for disease modeling and drug screening. *Biotechnology Advances* vol. 35 (2017).
81. Guimarães, C. F., Gasperini, L., Marques, A. P. & Reis, R. L. The stiffness of living tissues and its implications for tissue engineering. *Nat. Rev. Mater.* doi:10.1038/s41578-019-0169-1.
82. Yang, X. *et al.* Tri-iodo-L-thyronine promotes the maturation of human cardiomyocytes-derived from induced pluripotent stem cells. (2014) doi:10.1016/j.yjmcc.2014.04.005.
83. Jackman, C. P. *et al.* Engineered cardiac tissue patch maintains structural and electrical properties after epicardial implantation. *Biomaterials* **159**, 48–58 (2018).
84. Moorman, A., Webb, S., Brown, N. A., Lamers, W. & Anderson, R. H. Development of the heart: (1) formation of the cardiac chambers and arterial trunks. *Heart* **89**, 806–14 (2003).
85. Mandrycky, C. J. *et al.* Engineering Heart Morphogenesis. *Trends Biotechnol.* (2020) doi:10.1016/j.tibtech.2020.01.006.
86. Przemeck, G. K. H., Heinzmann, U., Beckers, J. & Hrabé de Angelis, M. Node and midline defects are associated with left-right development in Delta1 mutant embryos. *Development* **130**, 3–13 (2003).
87. de Bakker, B. S. *et al.* An interactive three-dimensional digital atlas and quantitative database of human development. *Science* **354**, aag0053 (2016).
88. Van Vliet, P., Wu, S. M., Zaffran, S. & Pucéat, M. Early cardiac development: A view from stem cells to embryos. *Cardiovasc. Res.* **96**, 352–362 (2012).

89. Oostra, R.-J., Steding, G., Lamers, W. H. . & Moorman, A. F. M. . *Steding's and Virágh's Scanning Electron Microscopy Atlas of the Developing Human Heart*. *Steding's and Virágh's Scanning Electron Microscopy Atlas of the Developing Human Heart* (Springer New York, 2007). doi:10.1007/978-0-387-68272-3_1.

90. Garcia-Canadilla, P. *et al.* Myoarchitectural disarray of hypertrophic cardiomyopathy begins pre-birth. *J. Anat.* **235**, 962–976 (2019).

91. Yen Ho, S. Anatomy and myoarchitecture of the left ventricular wall in normal and in disease. doi:10.1093/ejechocard/jep159.

92. Mekkaoui, C. *et al.* Diffusion Tractography of the Entire Left Ventricle by Using Free-breathing Accelerated Simultaneous Multisection Imaging. *Radiology* **282**, 850–856 (2017).

93. Streeter, D. D. & Hanna, W. T. Engineering mechanics for successive states in canine left ventricular myocardium. II. Fiber angle and sarcomere length. *Circ. Res.* **33**, 656–64 (1973).

94. Pope, A. J., Sands, G. B., Smaill, B. H. & LeGrice, I. J. Three-dimensional transmural organization of perimysial collagen in the heart. *Am. J. Physiol. Circ. Physiol.* **295**, H1243–H1252 (2008).

95. Gutstein, D. E., Liu, F. Y., Meyers, M. B., Choo, A. & Fishman, G. I. The organization of adherens junctions and desmosomes at the cardiac intercalated disc is independent of gap junctions. *Journal of Cell Science* vol. 116 875–885 (2003).

96. 3D Cell Culture Systems for Cardiovascular Tissue Engineering: In Vitro Modelling and In Vivo Regenerative Therapies | Frontiers Research Topic. https://www.frontiersin.org/research-topics/12897/3d-cell-culture-systems-for-cardiovascular-tissue-engineering-in-vitro-modelling-and-in-vivo-regener.

97. Hasan, W. Autonomic cardiac innervation: Development and adult plasticity. *Organogenesis* vol. 9 176–193 (2013).

98. Anderson, R. H., Smerup, M., Sanchez-Quintana, D., Loukas, M. & Lunkenheimer, P. P. The three-dimensional arrangement of the myocytes in the ventricular walls. *Clin. Anat.* **22**, 64–76 (2009).

99. Kim, D.-H. *et al.* Nanoscale cues regulate the structure and function of macroscopic cardiac tissue constructs. *Proc. Natl. Acad. Sci. U. S. A.* **107**, 565–70 (2010).

100. Beladan, C. C., Călin, A., Roşca, M., Ginghină, C. & Popescu, B. A. Left ventricular twist dynamics: principles and applications. *Heart* **100**, 731–40 (2014).

101. Grosberg, A., Gharib, M. & Kheradvar, A. Effect of Fiber Geometry on Pulsatile Pumping and Energy Expenditure. *Bull. Math. Biol.* **71**, 1580–1598 (2009).

102. O'Reilly, J. C., Ritter, D. A. & Carrier, D. R. Hydrostatic locomotion in a limbless tetrapod. *Nature* **386**, 269–272 (1997).

103. Clark, R. B. & Cowey, J. B. *FACTORS CONTROLLING THE CHANGE OF SHAPE OF CERTAIN NEMERTEAN AND TURBELLARIAN WORMS*.

104. Costa, K. D., Takayama, Y., McCulloch, A. D. & Covell, J. W. Laminar fiber architecture and three-dimensional systolic mechanics in canine ventricular myocardium. *Am. J. Physiol. - Hear. Circ. Physiol.* **276**, (1999).

105. Victor, S., Nayak, V. M. & Rajasingh, R. *Evolution of the Ventricles*. *Evolution of the Ventricles Guest Editorial* vol. 26 (1999).

106. Grosberg, A. & Gharib, M. Physiology in Phylogeny: Modeling of Mechanical Driving Forces in Cardiac Development. *Heart Fail. Clin.* **4**, 247–259 (2008).

107. Shiraishi, Isao ;Takamatsu, Tetsuro ;Fujita, S. Three-dimensional observation with a confocal scanning laser microscope of fibronectin immunolabeling during cardiac looping in the chick embryo. *Anat. Embryol. (Berl).* **191**, 183–189 (1995).

108. Price, R. L., Chintanowonges, C., Shiraishi, I., Borg, T. K. & Terracio, L. Local and regional variations in myofibrillar patterns in looping rat hearts. *Anat. Rec.* **245**, 83–93 (1996).

109. Mekkaoui, C. *et al.* Diffusion MRI Tractography of the Developing Human Fetal Heart. *PLoS One* **8**, e72795 (2013).

110. Ivanovitch, K., Temiño, S. & Torres, M. Live imaging of heart tube development in mouse reveals alternating phases of cardiac differentiation and morphogenesis. *Elife* **6**, e30668 (2017).

111. Krishnan, A. *et al.* A detailed comparison of mouse and human cardiac development. *Pediatr. Res.* **76**, 500–507 (2014).

112. Ushiki, T. Collagen fibers, reticular fibers and elastic fibers. A comprehensive understanding from a morphological viewpoint. *Archives of Histology and Cytology* vol. 65 109–126 (2002).

113. Schroer, A. K. & David Merryman, W. Mechanobiology of myofibroblast adhesion in fibrotic cardiac disease. (2015) doi:10.1242/jcs.162891.

114. Jiao, A. *et al.* Thermoresponsive nanofabricated substratum for the engineering of three-dimensional tissues with layer-by-layer architectural control. *ACS Nano* **8**, 4430–9 (2014).

115. Kim, P. *et al.* Fabrication of nanostructures of polyethylene glycol for applications to protein adsorption and cell adhesion. *Nanotechnology* **16**, 2420–2426 (2005).

116. Kim, D.-H. *et al.* Nanopatterned cardiac cell patches promote stem cell niche formation and myocardial regeneration. *Integr. Biol.* **4**, 1019 (2012).

117. Manuel Pioner, J. *et al.* Absence of full-length dystrophin impairs normal maturation and contraction of cardiomyocytes derived from human-induced pluripotent stem cells. doi:10.1093/cvr/cvz109.

118. Falconnet, D., Csucs, G., Michelle Grandin, H. & Textor, M. Surface engineering approaches to micropattern surfaces for cell-based assays. *Biomaterials* vol. 27 3044–3063 (2006).

119. Moeller, J. *et al.* Controlling cell shape on hydrogels using lift-off protein patterning. *PLoS One* **13**, e0189901 (2018).

120. Rim, N. G. *et al.* Micropatterned cell sheets as structural building blocks for biomimetic vascular patches. *Biomaterials* **181**, 126–139 (2018).

121. Feinberg, A. W. *et al.* Controlling the contractile strength of engineered cardiac muscle by hierarchal tissue architecture. *Biomaterials* **33**, 5732–5741 (2012).

122. Grosberg, A. *et al.* Muscle on a chip: In vitro contractility assays for smooth and striated muscle. *J. Pharmacol. Toxicol. Methods* **65**, 126–135 (2012).

123. Badrossamay, M. R. *et al.* Engineering hybrid polymer-protein super-aligned nanofibers via rotary jet spinning q. *Biomaterials* **35**, 3188–3197 (2014).

124. Tzatzalos, E., Abilez, O. J., Shukla, P. & Wu, J. C. Engineered heart tissues and induced pluripotent stem cells: Macro- and microstructures for disease modeling, drug screening, and translational studies. *Advanced Drug Delivery Reviews* vol. 96 (2016).

125. Haraguchi, Y., Shimizu, T., Yamato, M. & Okano, T. Scaffold-free tissue engineering using cell sheet technology. *RSC Advances* (2012) doi:10.1039/c2ra00704e.

126. Sekine, H. *et al.* In vitro fabrication of functional three-dimensional tissues with perfusable blood vessels. *Nat. Commun.* **4**, (2013).

127. Kubo, H., Shimizu, T., Yamato, M., Fujimoto, T. & Okano, T. Creation of myocardial tubes using cardiomyocyte sheets and an in vitro cell sheet-wrapping device. *Biomaterials* **28**, 3508–3516 (2007).

128. Williams, N. P. *et al.* Engineering anisotropic 3D tubular tissues with flexible thermoresponsive nanofabricated substrates. *Biomaterials* **240**, 119856 (2020).

129. Valls-Margarit, M. *et al.* Engineered Macroscale Cardiac Constructs Elicit Human Myocardial Tissue-like Functionality. *Stem Cell Reports* **13**, 207–220 (2019).

130. Lee, E. J., Kim, D. E., Azeloglu, E. U. & Costa, K. D. Engineered Cardiac Organoid Chambers: Toward a Functional Biological Model Ventricle. *Tissue Eng. Part A* **14**, 215–225 (2008).

131. Zhang, D. *et al.* Tissue-engineered cardiac patch for advanced functional maturation of human ESC-derived cardiomyocytes. *Biomaterials* **34**, 5813–5820 (2013).

132. Leonard, A. *et al.* Afterload promotes maturation of human induced pluripotent stem cell derived cardiomyocytes in engineered heart tissues. *J. Mol. Cell. Cardiol.* (2018) doi:10.1016/j.yjmcc.2018.03.016.

133. Long, C. *et al. Correction of diverse muscular dystrophy mutations in human engineered heart muscle by single-site genome editing*. https://www.ncbi.nlm.nih.gov/pmc/articles/PMC5796795/pdf/aap9004.pdf (2018).

134. Abilez, O. J. *et al.* Passive Stretch Induces Structural and Functional Maturation of Engineered Heart Muscle as Predicted by Computational Modeling. *Stem Cells* **36**, 265–277 (2018).

135. Mannhardt, I. *et al.* Human Engineered Heart Tissue: Analysis of Contractile Force.

Stem Cell Reports **7**, 29–42 (2016).

136. Freedman, B. S. *et al.* Modelling kidney disease with CRISPR-mutant kidney organoids derived from human pluripotent epiblast spheroids. *Nat. Commun.* **6**, (2015).

137. Skylar-Scott, M. A. *et al.* Biomanufacturing of organ-specific tissues with high cellular density and embedded vascular channels. *Sci. Adv.* **5**, eaaw2459 (2019).

138. Kupfer, M. E. *et al.* In Situ Expansion, Differentiation and Electromechanical Coupling of Human Cardiac Muscle in a 3D Bioprinted, Chambered Organoid. *Circ. Res.* CIRCRESAHA.119.316155 (2020) doi:10.1161/CIRCRESAHA.119.316155.

139. MacQueen, L. A. *et al.* A tissue-engineered scale model of the heart ventricle. *Nat. Biomed. Eng.* 1 (2018) doi:10.1038/s41551-018-0271-5.

140. Hinton, T. J. *et al.* Three-dimensional printing of complex biological structures by freeform reversible embedding of suspended hydrogels. *Sci. Adv.* **1**, e1500758 (2015).

141. Lee, A. *et al. 3D bioprinting of collagen to rebuild components of the human heart*. http://science.sciencemag.org/.

Chapter 2. Engineering Anisotropic 3D Tubular Tissues with Flexible Thermoresponsive Nanofabricated Substrates

This chapter has been published in the following first-author manuscript:

N.P. Williams, M. Rhodehamel, C. Yan, A.S.T. Smith, A. Jiao, C.E. Murry, M. Scatena, D.-H. Kim, Engineering anisotropic 3D tubular tissues with flexible thermoresponsive nanofabricated substrates, Biomaterials. 240 (2020) 119856.

2.1 Abstract

Tissue engineering aims to capture the structural and functional aspects of diverse tissue types *in vitro*. However, most approaches are limited in their ability to produce complex 3D geometries that are essential for tissue function. Tissues, such as the vasculature or chambers of the heart, often possess curved surfaces and hollow lumens that are difficult to recapitulate given their anisotropic architecture. Cell-sheet engineering techniques using thermoresponsive substrates provide a means to stack individual layers of cells with spatial control to create dense, scaffold-free tissues. In this study, we developed a novel method to fabricate complex 3D structures by layering multiple sheets of aligned cells onto flexible scaffolds and casting them into hollow tubular geometries using custom molds and gelatin hydrogels. To enable the fabrication of 3D tissues, we adapted our previously developed thermoresponsive nanopatterned cell-sheet technology by applying it to flexible substrates that could be folded as a form of tissue origami. We demonstrated the versatile nature of this platform by casting aligned sheets of smooth and cardiac muscle cells circumferentially around the surfaces of gelatin

hydrogel tubes with hollow lumens. Additionally, we patterned skeletal muscle in the same fashion to recapitulate the 3D curvature that is observed in the muscles of the trunk. The circumferential cell patterning in each case was maintained after one week in culture and even encouraged organized skeletal myotube formation. Additionally, with the application of electrical field stimulation, skeletal myotubes began to assemble functional sarcomeres that could contract. Cardiac tubes could spontaneously contract and be paced for up to one month. Our flexible cell-sheet engineering approach provides an adaptable method to recapitulate more complex 3D geometries with tissue specific customization through the addition of different cell types, mold shapes, and hydrogels. By enabling the fabrication of scaled biomimetic models of human tissues, this approach could potentially be used to investigate tissue structure-function relationships, development, and maturation in the dish.

2.2 Introduction

Tissues throughout the body possess complex three-dimensional (3D) structures with many degrees of organization and function. For example, the vasculature, like many other tissues, is organized by stratification of several layers of different cell types that perform complementary functions to modulate blood pressure and tissue perfusion[1,2]. The endothelial cells in the lining of the blood vessel's lumen are oriented parallel to the direction of blood flow, whereas the surrounding smooth muscle cells that encircle the endothelium are aligned perpendicularly. Similar patterns of differential organization are observed in the helical fiber organization of the myocardium in the heart and in the radial

fan patterns seen in the trapezius and pectoral muscles of the trunk. The function of each of these tissues is highly dependent upon their structure and 3D geometry, and when their organization is compromised by disease it can be detrimental or potentially fatal[3–5]. To study tissue function and their associated diseases, advancements have been made in tissue engineering to recapitulate tissue micro- and macroenvironments *in vitro.* For example, cell-dense cardiac tissue patches made from induced pluripotent stem cell-derived cardiomyocytes (iPSC-CMs) can mimic action potential conduction velocities close to those of adult cardiac tissues[6–8]; vascular grafts have been made from cell-deposited matrix and then decellularized before implantation[9–11]; and bioprinting with cellularized-inks (or bioinks) has enabled fabrication of intricate 3D tissue-specific structures with corresponding function[12–15]. A challenge facing each of these approaches is that tissues often have complex 3D geometries, including curved surfaces and hollow lumens. Such structures have been difficult to recreate *in vitro* due to limitations of available fabrication techniques. Specifically, there are few fabrication approaches that allow for production of curved 3D geometries while also having control over spatial organization at the cell-layer level. The ability to recapitulate these structures would impart function that better mimics native tissues and organs.

To address this need, our group has previously established a nanofabrication technique to pattern sheets of organized cells and stack them to create multi-layered tissue patches using a novel gel-casting technique in conjunction with thermoresponsive substrates[16,17]. In the present study, we sought to improve upon this technology by introducing flexible substrates and custom molds to enable the fabrication of organized 3D tissue structures. We found that all three cell types could be patterned to form an intact

monolayer with a uniform orientation in the direction of the nanotopography. Each monolayer was lifted from the surface through temperature-mediated release provided by the thermoresponsive poly(N-isopropylacrylamide) (pNIPAM) functional layer. Multiple organized monolayers were stacked onto a single flexible film and were folded into a cylindrical shape, as a form of tissue origami, where the organized cell layers could be casted into free-standing a 3D tubular tissue. We demonstrated the diverse application of this technology by fabricating tubular tissues with curved surfaces from three muscle types: smooth, skeletal, and cardiac muscle. This approach enabled patterning of all three cell types in 3D multilayered tissues with circumferential alignment that was maintained for two weeks in culture. Additionally, with application of electrical field stimulation, skeletal myotubes assembled functional sarcomeres that could contract, and cardiac tubes could be paced for over one month. This flexible patterned film technology can readily be adapted to fabricate tissues with other complex geometries by changing the shape of the flexible film and custom mold, producing better tissues for the study of development and disease.

2.3 Materials and Methods

2.3.1 Fabrication of Flexible Thermoresponsive Nanofabricated Substrates (fTNFS)

To fabricate flexible films with nanotopographical cues and thermoresponsive properties, capillary force lithography was utilized as described in our previously established protocol[16–18]. Briefly, nanopatterned films were fabricated using 100 µL of a

polymer curable by ultraviolet light (UV), polyurethane acrylate (PUA, Norland Optical Adhesive #76) mixed with either 1% or 20% (w/w) glycidyl methacrylate (GMA). The UV-curable polymer was sandwiched and spread between a 23 μm-thick flexible poly-ethylene terephthalate (PET) film and a PUA master mold with parallel ridges and grooves

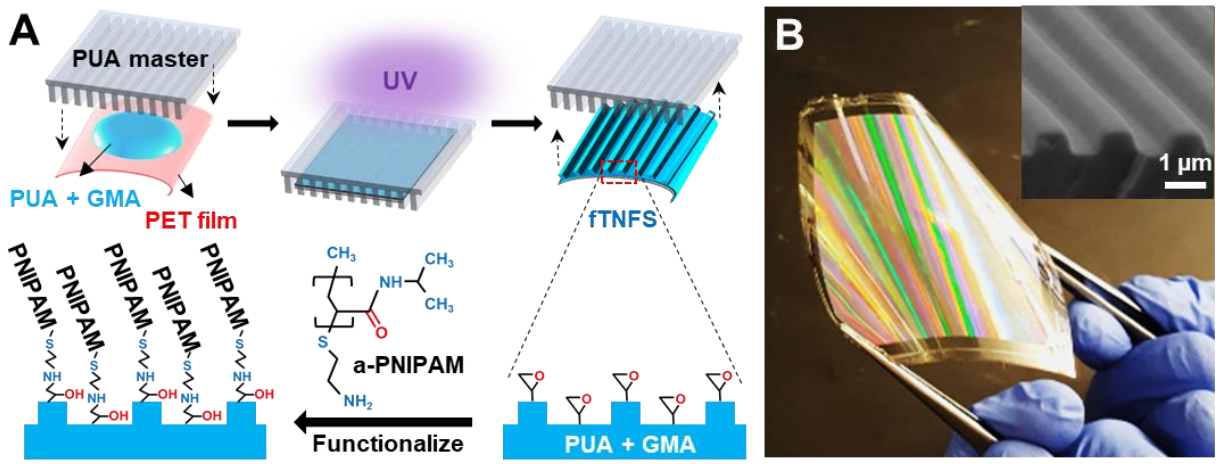

that were 800 nm in width and 600 nm in depth (**Figure 1A**).

Figure 2.1. Fabrication of anisotropic multilayered tissues using flexible thermoresponsive nanofabricated substrates (fTNFS). (A) Fabrication of flexible nanopatterned substrates (fTNFS) using capillary force lithography and subsequent thermoresponsive functionalization with amine-terminated pNIPAM. **(B)** Image of flexible-TNFS after curing and a-PNIPAM functionalization. Rainbow coloring is caused by the nanotopography diffracting light. (Inset) Scanning electron micrograph of fTNFS surface demonstrating high fidelity fabrication of the ridge-groove nanotopography.

The mold and film construct were exposed to high intensity 365 nm wavelength UV light for 1 minute to polymerize the PUA-GMA solution. After initial polymerization of the sandwiched polymer layer, the flexible film and adhered nanopatterned polymer layer were carefully removed from the master mold using forceps (**Figure 1B**). The newly constructed nanopatterned film was placed under low intensity 365 nm UV light for 24 hours to ensure complete polymerization of the PUA-PGMA polymer. To provide thermoresponsive functionality, nanopatterned substrates were then dip-coated with an amine-terminated poly(N-isopropylacrylamide) (pNIPAM) solution (13 μM in H_2O, M_n =

2500 Sigma-Aldrich) for 24 hours on a tabletop rocker (55 rpm, room temperature). After 24 hours, excess pNIPAM was removed from the flexible thermoresponsive nanofabricated substrates (fTNFS) through three 5-minute washes with deionized water and allowed to dry overnight. The films were cut into rectangular sheets (1.25 cm x 1.5 cm) using a die cutter. The fTNFS were dipped in 70% ethanol and exposed to 294 nm UV light for one hour in a biosafety cabinet for sterilization prior to use.

In order to restrict cell-seeding to the fTNFS surface and minimize cell waste, two fTNFS were temporarily affixed into the bottoms of custom polydimethylsiloxane (PDMS, Sylgard 181) rectangular wells (13.5 mm x 30 mm) using porcine gelatin (7.5% w/v, Sigma) crosslinked with transglutaminase (MooGloo^{TM} TI-TG, Modernist Pantry) as an adhesive. Flexible TNFS were incubated with fetal bovine serum (FBS, Sigma) overnight at 4°C before cell seeding to deposit a thin protein layer to promote cell adhesion to the surfaceScanning Electron Microscopy of fTNFS

Poly-NIPAM-functionalized fTNFS were sputter-coated with Au/Pd alloy prior to imaging using scanning electron microscopy (Sirion XL30, FEI, OR, USA). Images were taken with an acceleration voltage of 5 kV and spot size of 2.

2.3.2 Cell Culture and Cell Seeding of fTNFS

Mouse aortic smooth muscle cells (SMCs) were generously provided by Dr. Marta Scatena's group[19]. Mouse SMCs were cultured on tissue-culture treated plastic dishes with Dulbecco's Modified Eagle's Medium (DMEM, Gibco) supplemented with 1% penicillin-streptomycin (p/s, Sigma), 10% FBS. Cells were passaged at 80% confluency during expansion and only passages 30 and below were used to minimize confounding

effects of cell senescence on tissue fabrication. Cells were split and seeded onto fTNFS at a density of 175,000 cells/cm^2 in 1 mL of medium and allowed to adhere overnight at 37°C and 5% CO_2. Seeded cells were cultured for 5-7 days before cell sheet stacking and tissue fabrication to allow a highly confluent monolayer of cells to form. Observation of cell growth was conducted using a bright-field microscope (Nikon TS100).

C2C12 mouse muscle myoblasts (C2C12s; ATCC) were cultured under the same conditions as the SMCs as described above and seeded at 175,000 cells/cm^2 onto fTNFS. However, seeded cells were cultured for 2-3 days before cell sheet stacking and tissue fabrication as C2C12 cells were found to proliferate at a faster rate than SMCs. Three to four days after tissue fabrication, tissue constructs were cultured in a low-serum containing medium (DMEM, 2% horse serum (HS), 1% p/s) to promote fusion and differentiation of myoblasts into myotubes. To promote further functional and structural maturation of myotubes, chronic broad-field electrical stimulation was applied (1 Hz, 3V, 24 ms; IonOptix C-Pace) after 3-4 days of culturing tissues with low-serum differentiating medium and once myotube formation was observed over the entire tissue surface area.

Cardiomyocytes (CMs) and endocardial-like endothelial cells (ECs) were differentiated from human induced pluripotent stem cells (hiPSCs, UC 3-4) derived from patient urine samples [20]. Endothelial cells were included to promote cell sheet formation as monolayers of pure cardiomyocytes were found to clump during tissue fabrication (**Figure 2.2**).

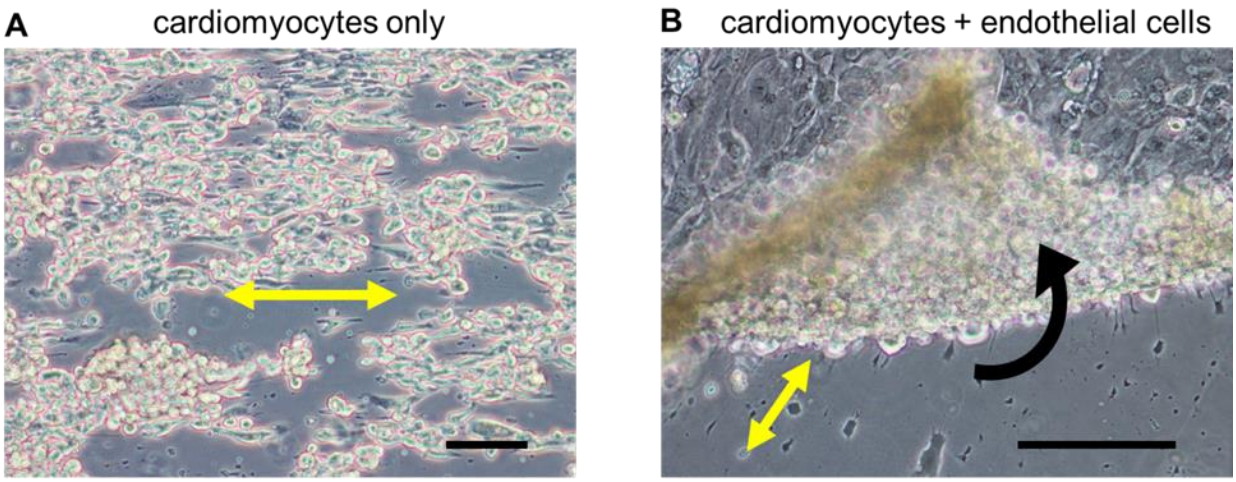

Figure 2.2. Incorporation of endothelial cells promotes cardiac sheet formation and detachment. Representative brightfield microscope images of detaching nanopatterned cardiac sheets without incorporation of stromal cells **(A)** and with incorporation of endothelial cells **(B)** demonstrating intact, spontaneous cardiac sheet detachment only in the co-culture condition. Direction of cell sheet detachment is labeled by the black arrow. Double headed yellow arrows in **(A)** and **(B)** denote the orientation of the nanotopography on the scaffold below. Scale bars, 100µm.

Established monolayer-based differentiation protocols were used that modulate Wnt-signaling pathways with small molecules to specify cardiac mesoderm lineages [21,22]. In brief, UC 3-4 hiPSC colonies were maintained on Matrigel (1:60, Corning) coated tissue-culture plates in mTeSR medium until 80% confluency. Colonies were then replated into a monolayer at 250,000 cells/cm^2 (high density) or 100,000 cells/cm^2 (low density) for directed differentiation of cardiomyocytes (CMs) or endothelial cells (ECs), respectively [22,23]. To drive differentiation toward the cardiomyocyte lineage, high density monolayers were exposed to CHIR-99021 (Fischer Technologies) in Roswell Park Memorial Institute 1640 (RPMI) medium with B27 without insulin (Gibco) on day 0 (induction) to activate the Wnt signaling pathway and specify mesoderm gene expression. High-density monolayers were exposed to the Wnt-inhibitor IWP4 (Stemgent) on day 3 to further specify cardiac mesoderm and were then cultured in RPMI-B27 medium with insulin from day 7 and

onward. Beating monolayers of cardiomyocytes were observed as early as day 9. Cardiac-differentiated populations were then subjected to a lactate-rich glucose-poor selection medium at day 14 for 3 days to enrich the cardiomyocyte population [24]. Cells were harvested on day 17 and fixed in 4% paraformaldehyde as a single-cell solution and prepared for flow cytometry to determine cardiomyocyte purity. Cells were stained with a mouse-anti-cardiac troponin T (cTnT) antibody (1:100, Thermo-Scientific) and counterstained with a goat-anti-mouse Alexa Fluor 488-counjugated antibody (1:200, Invitrogen). Cell populations used for this study were at least 95% cTnT-positive when analyzed by flow cytometry (**Figure 2.3.**).

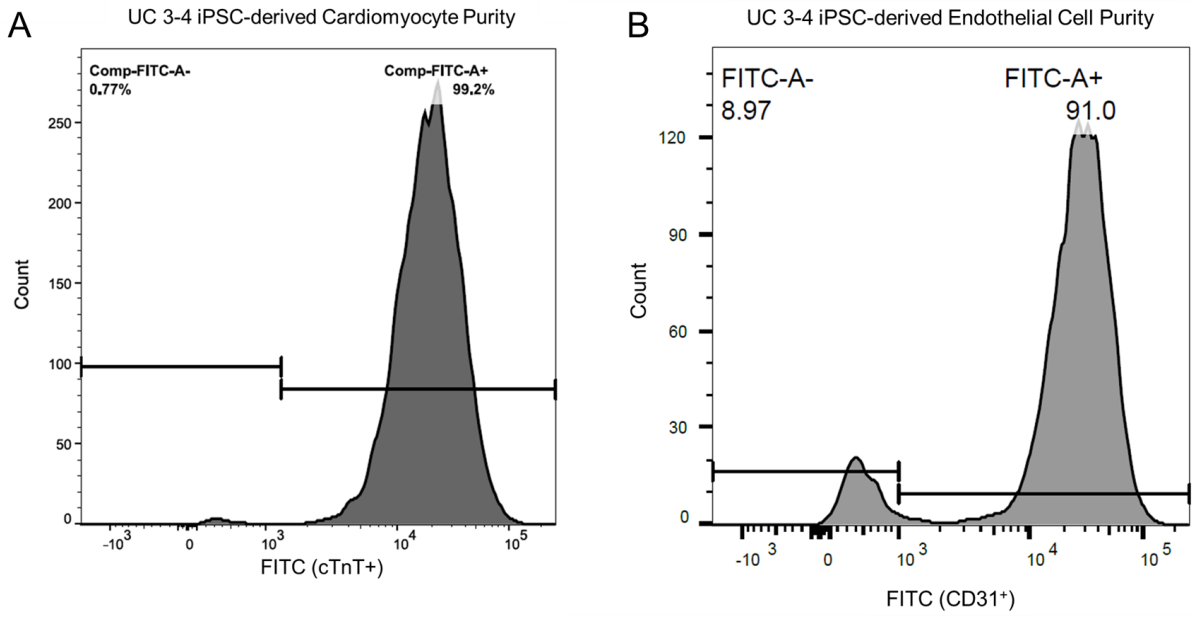

Figure 2.3. Characterization of iPSC-derived cardiomyocytes and endocardial-like endothelial cells with flow cytometry. Cardiomyocytes were subjected to lactate selection medium for 3 days and then harvested on day 17 for flow cytometry. 99.2% of cells were identified as positive for cTnT. Endothelial cells were live-stained for CD31 surface markers on day 12. 91.0% of cells were identified as positive for CD31 surface markers.

Similarly, to drive differentiation towards the cardiac endothelial lineage, low density monolayers were exposed to activin-A (R&D Systems) and Matrigel in RPMI with B27 on

day 0 (induction). On day 1 post induction, low-density monolayers were exposed to bone morphogenic protein-4 (BMP-4; R&D Systems) and CHIR-99021 in RPMI-B27 medium. To specify the endothelial lineage, low-density monolayers were switched into StemPro-34 medium, containing vascular endothelial growth factor (VEGF; PeproTech), BMP-4, basic fibroblast growth factor (bFGF; R&D Systems), ascorbic acid, and monothioglycerol. On day 5, the low-density monolayers were re-plated at 13k/cm^2 into gelatin-coated tissue culture plates and expanded in Endothelial Growth Medium-2 (EGM-2, Lonza) supplemented with VEGF, bFGF, and CHIR-99021 until day 11. Live cells were stained with a mouse-anti-CD31 antibody pre-conjugated with an Alexa Fluor 488 fluorophore (R&D Systems) for 1 hour on ice and flow cytometry was performed immediately. All EC populations used in this study were at least 90% CD31-positive when analyzed by live-cell flow cytometry on day 11. ECs were then seeded with cardiomyocytes immediately or cryopreserved for later use.

To limit possible confounding factors associated with age variation in the CM or EC population, CMs were used within 17-30 days post-induction and ECs used between 12-15 days post-induction for tissue fabrication. Purified CMs and ECs were seeded onto fTNFS such that the final proportion of CMs and ECs was 88% and 12% (~7:1 CMs:ECs) of the total cell number, respectively. This CM:EC ratio was optimized during preliminary experiments to yield highly aligned and confluent cell sheets that could withstand our previously published cell-sheet detachment and stacking process[16,17]. Cardiac cell sheets were cultured for 10-14 days in cardiac growth medium (75% RPMI-B27 + insulin, 25% EGM-2, 10% FBS, 1% p/s) before cell sheet stacking and tissue fabrication to allow for the formation of highly dense and confluent monolayers.

2.3.3 Cell Sheet Stacking

Cell sheets that form dense monolayers through cell-cell connection and ECM deposition exhibit a tendency to clump or fold inward on themselves once detached from cell culture surfaces. To prevent this, we previously developed a gel casting method for stacking aligned cell sheets that conferred layer-by-layer control over tissue architecture (**Figure 2.4**)[16,17].

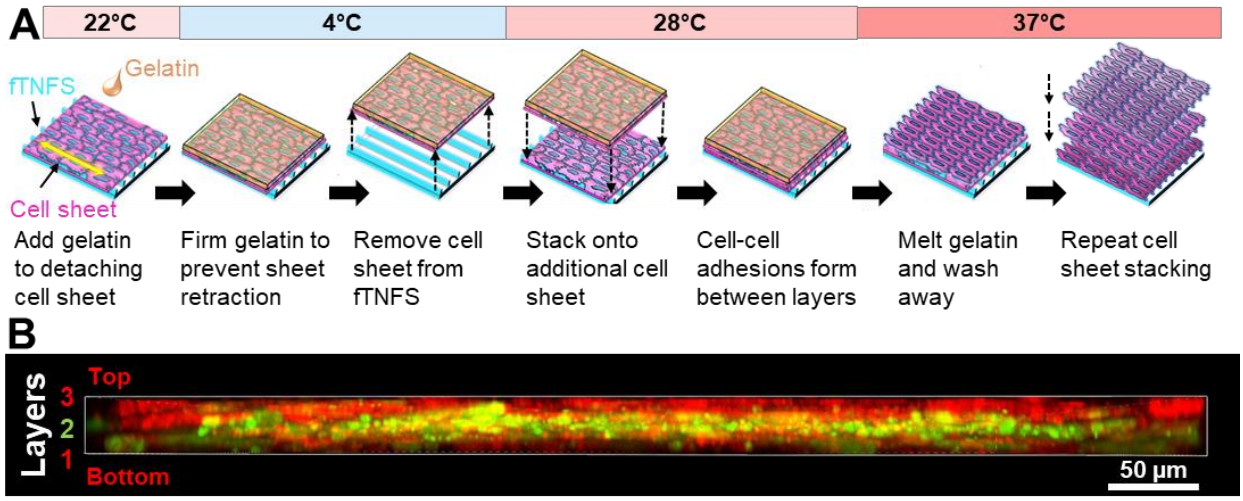

Figure 2.4. Nanopatterned cell sheet gel casting and stacking tehcnique. (A) Schematic of gel casting and stacking of organized cell monolayers from flexible TNFS. **(B)** Z-stack cross-sectional image of smooth muscle cell tri-layer tissue stack 24 hours after stacking. Top and bottom sheets were membrane-dyed red (Cell Tracker Red) and middle sheet was membrane-dyed green (Cell Tracker Green) before stacking.

Briefly, patterned cell sheets were detached from the fTNFS by lowering the culture temperature to 22°C (room temperature), below the lower critical solution temperature point of pNIPAM (32°C), where the hydrophobicity of pNIPAM abruptly and dramatically switches to a hydrophilic hydrogel. This hydrogel polymer then swells and dislodges intact cell sheets[25,26]. After incubation for 30 minutes (for C2C12 and cardiac sheets) or 1 hour

(SMC sheets) at room temperature, and just before complete detachment, cell sheets were cast in a 7.5% w/v gelatin solution at 4°C for 30 minutes to maintain the anisotropic organization of the cell sheet and prevent sheet retraction. The gel-casted cell sheets were moved into a 28°C incubator for one hour to further promote cell detachment from the fTNFS without melting the gelatin that maintains the cellular alignment. The gel-casted sheets were then incubated at 4°C for 15 minutes to allow the gelatin to further solidify for better handleability. The gel-casted cell sheet was then removed from the fTNFS with forceps and stacked on top of another cell sheet with parallel cellular orientation to produce an aligned, bi-layered laminar tissue. Once stacking was complete, the gelatin was completely dissolved 37°C and the construct washed with warm (37°C) medium to ensure the remaining tissue structure constitutes a scaffold-free, bi-layered cell sheet construct on top of an fTNFS. This process was then repeated to add a third and final cell layer with parallel orientation. To visualize maintenance of three discrete cell layers, each cell sheet was labeled prior to stacking by incubating with either a red or green cell dye (2 μM CellTracker CMFDA Green or 2 μM CellTracker Red CMTPX, Invitrogen) for 30 minutes. Z-stacks were then taken with a confocal microscope (Nikon A1R, 10x objective) to visualize the alternately layered red, green, then red cell sheets (**Figure 2.4.B**).

2.3.4 Flexible TNFS Manipulation

After stacking three-layered tissues as described above (**Figure 2.4.A**), tri-layered tissue constructs were then cast into a 3D tubular geometry using polystyrene cylindrical molds and custom 3D-printed casting implements (**Figure 2.5.A-D**).

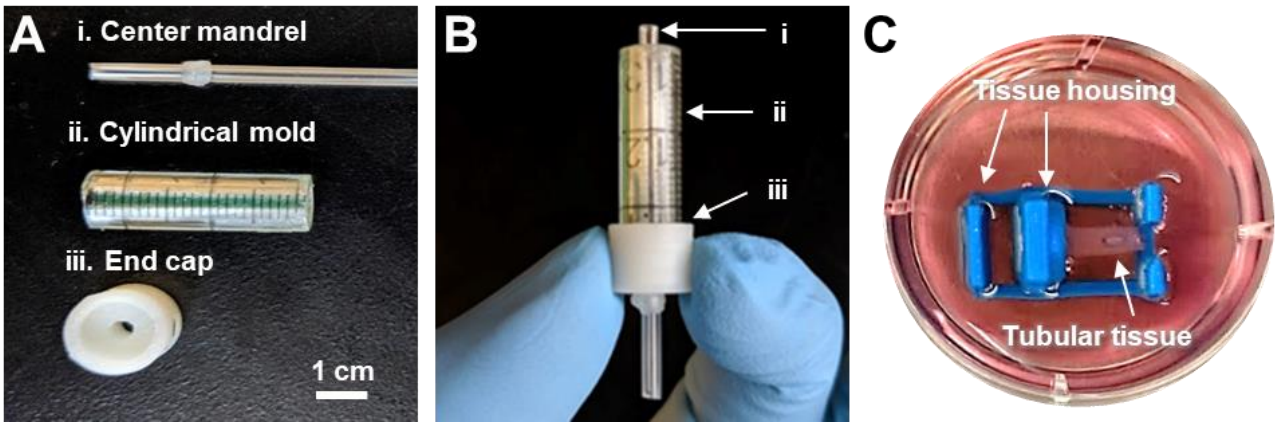

Figure 2.5. Casting mold implements for fabrication of tubular tissues. (A) Image of tissue casting implements. **(i)** Mandrel that is inserted through the 3D-printed end cap **(iii)** into the cylindrical mold **(ii)** to create a hollow lumen through the center of the resulting tubular tissue. **(B)** Casting mold pieces in B assembled as during tissue casting. The fTNFS and cell layers are manipulated into the cylindrical mold **(ii)**, the cap end **(iii)** is fastened over one end of the cylindrical mold (**ii**), and the mandrel **(i)** is inserted through the bottom of the end cap **(iii)**, and the hydrogel is pipetted into the open end of the mold **(ii)** to cast the cell sheets around a hydrogel tube. **(C)** Image of resulting tubular tissue attached to a custom 3D-printed housing in a culture well after removal from the casting mold.

The tri-layered tissue and fTNFS were first incubated in room temperature phosphate buffered saline (PBS, Gibco) for 30 minutes to promote the basement layer to detach from the fTNFS. Simultaneously, the polystyrene center mandrel (**Figure 2.5.A.i.**), cylindrical mold (**Figure 2.5.A.ii.**), and 3D-printed end cap (**Figure 2.5.A.iii.**) were coated with a 1% bovine serum albumin in PBS (BSA, Sigma) solution to prevent the final tissue construct from sticking upon removal from the mold. The fTNFS with cell sheets were manipulated with forceps into a cylindrical shape with the cell layers facing inward and inserted into the cylindrical mold (**Figure 2.4 & 2.5.A.ii.**). The end cap (**Figure 2.5.A.iii.**) was then placed on the end of the cylindrical mold and the center mandrel (**Figure 2.5.A.i.**) was inserted into the assembly through the hole in the end cap. The final casting assembly (**Figure 2.5.B**) ensured that the lumen created in the tissue construct was straight and the resulting tissue walls were of uniform thickness on all sides. The

remaining negative space within the casting tube was then filled with 200 µL of warmed gelatin and transglutaminase crosslinker (10% TG in PBS, MooGloo^{TM} TI-TG; 10% porcine gelatin w/v in DMEM, Sigma) and allowed to crosslink at 28°C for 1 hour; the final concentration of crosslinked gelatin was 5%. After the gelatin was crosslinked, the molded tissue constructs were incubated at 4°C for 30 minutes to allow the basement layer of cells connected to the fTNFS to detach. The fTNFS and tubular tissue with cells was then carefully removed from the casting assembly with forceps and the fTNFS was unwrapped from the tubular tissue. The final tubular tissue was attached to a custom 3D printed tissue housing (**Figure 2.5.C**) to prevent tissue damage and placed into a culture well with medium.

2.3.5 Tissue Histology and Dimensional Measurements

To visualize cellular orientation and quantify tissue dimensions after 7 days in culture, SMC tubular tissues were fixed in 4% paraformaldehyde (PFA in PBS) for 30 minutes at room temperature and washed with PBS. Tissues were then dehydrated by serial washes in ethanol (50%, 60%, and 70%) for 20 minutes before embedding in paraffin blocks for sectioning. Tubular tissues were cut using a cryostat (Leica CM1950) to make 4 µm cross-sections along the short access of the tube allowing for visualization of the center lumen, tissue wall thickness, and cell layer thickness (**Figure 2.6.A-C**). Sections were stained with hematoxylin and eosin to visualize extracellular matrix and cytoplasm (pink) and DNA (blue). ImageJ (National Institutes of Health) measurement tools were used to measure tissue wall thickness, cell layer thickness, lumen diameter, and outer diameter across 30

sections. Measurements of each dimension were averaged and standard deviation was calculated (GraphPad, Prism).

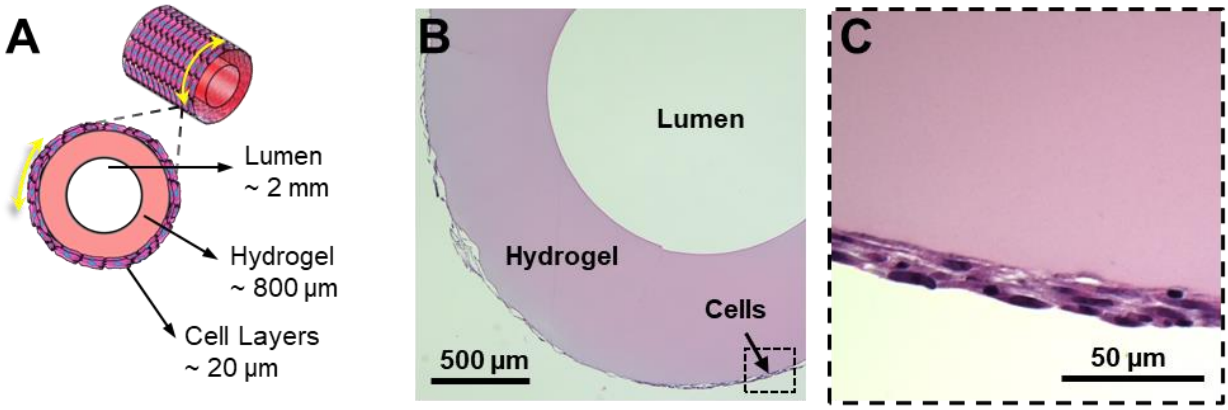

Figure 2.6. Fabrication of 3D tubular tissues with circumferential cellular alignment. (A) Cross-sectional schematic of expected tissue dimensions and structure. Thickness of cell layers is dependent on cell type and number of layers. **(B)** Histological cross-section of SMC tube stained with hematoxylin and eosin showing a hollow central lumen encircled by a gelatin hydrogel layer and cell layers. **(C)** Boxed inset of **(B)** demonstrating three layers of SMCs with elongated nuclei along the curvature of the tube's outer edge.

2.3.6 Immunostaining and Confocal Imaging

Tubular tissues were cultured for 7 days after casting and fixed in 4% paraformaldehyde (PFA in PBS) for 30 minutes at room temperature and washed with PBS. To visualize intercellular proteins, tissues were permeabilized in 0.2% Triton-X 100, 0.5% BSA, and 5% goat serum in PBS at room temperature for 1 hour and transferred into a blocking solution of 5% goat serum with 0.5% BSA in PBS for 2 hours to prevent non-specific antibody binding. Primary antibodies (mouse-anti-smooth muscle α-actin (1:200, SMα-actin, Abcam), mouse-anti-myosin heavy chain (1:50, MYH, A4.1025 Developmental Studies Hybridoma Bank, The University of Iowa, Department of Biology; deposited by the Baxter Lab for Stem Cell Biology at Stanford University), rabbit-anti-titin (1:300,

Myomedix)) were diluted in a staining solution of 1.5% goat serum in PBS and incubated with the respective tissues overnight at 4°C. Excess primary antibodies were washed away through three 5-minute washes with PBS before corresponding secondary antibodies (1:400, Alexa 488, 594, or 647, Invitrogen) and conjugated phalloidin (1:200, F-actin, 488 or 647, Invitrogen) were applied in 0.5% BSA in PBS for 2 hours at room temperature. Excess secondary antibodies were washed away through three 5-minute washes with PBS before a nuclear counterstain (DAPI, Invitrogen) was applied.

Given the relatively large 3D geometry of the tubular tissues, custom mounting chambers were developed by placing a square 3 mm-thick PDMS frame around the tissue and sandwiching them between two rectangular cover-glasses (0.17 mm thickness, Fisher Scientific). The tissues were stored in anti-fade mounting medium (VECTASHIELD, Vector Laboratories) within the PDMS mounting chambers. The rounded surfaces of the tubular tissues were slightly flattened to visualize their cellular layers with a confocal microscope, but the overall curvature of the tissue was maintained. Confocal z-stacks were taken of tubular tissues using either a Nikon A1R and or a Yokogawa W1 spinning-disk confocal microscope, and 10x-dry, 20x-dry, or 40x oil-immersion objectives.

2.3.7 Cellular Orientation Analysis

To quantify cellular orientation in 3D tubular tissues, confocal images of cytoskeletal filamentous actin (F-actin) for SMC, C2C12, and cardiac tubes were taken of three different areas using a 40x oil-immersion objective. These images were analyzed using a modified MATLAB script (MathWorks) that utilizes pixel gradient analysis to

determine the distribution of orientation angles within an image [16,27]. Briefly, a Gaussian low pass filter and Sobel horizontal edge-emphasize filter are applied (as predefined by the MATLAB Image Analysis Toolbox) to create a 2D convolution. The Sobel filter is then transposed to extract horizontal and vertical edges and then used to calculate the gradient magnitude of each pixel within the image. The images were then thresholded to define the edges of single cells and calculate their orientation angles relative to the x-axis at 0°. These orientation angles were then binned and plotted as histograms to represent the overall cell alignment of the 3D tissue.

2.4 Results

2.4.1 Flexible TNFS Fabrication and Cell Sheet Stacking

To develop a tissue engineering platform that would enable fabrication of 3D tissue geometries with control over local and global cellular patterning, we sought to adapt our established capillary force lithography techniques [16–18,28] and amine-terminated poly(N-isopropylacrylamide) (pNIPAM)-mediated surface chemistry to produce flexible thermoresponsive nanofabricated substrates (fTNFS). Thermoresponsive functionalization was included to mediate the release of organized cell sheets from the nanopatterned surfaces without the use of digestive enzymes, such as trypsins, which are required to detach cells from traditional culture surfaces. Flexible films were chosen in this study to enable the fabrication of 3D tissues with curved surfaces by their capacity to be folded into a cylindrical shape. Large area flexible films (5 cm x 5 cm) were patterned using a stiff polyurethane (PUA, 19.8 MPa) master mold with 800 nm ridges

and groves and 600 nm depth (**Figure 1A,B**). When examined by scanning electron microscopy, fTNFS were found to have high pattern fidelity even after functionalization with a pNIPAM layer and bending with forceps (**Figure 1B, inset**).

The speed and ease of cell-sheet detachment were optimized for each cell type by modulating the percentage of bound pNIPAM groups through increasing or decreasing the amount of glycidyl methacrylate (GMA) that is incorporated into the PUA layer during fTNFS fabrication[16,17]. We found that smooth muscle cell (SMC) sheets required more pNIPAM-mediated release from the fTNFS using our gel-casting method (**Figure 1C**) and 20% GMA was therefore blended into the PUA layer of the scaffolds. In contrast, skeletal myoblast (C2C12s) and cardiac sheets exhibited a tendency to spontaneously detach from fTNFS with higher GMA concentrations, and required much lower (1% GMA) levels of pNIPAM-mediated release. These differences in detachment may be due to the spontaneously contractile behavior of cardiomyocytes and the migration and fusion of muscle myoblasts during differentiation into myotubes. After optimization of GMA content, all cell sheet types could be detached and stacked to form multilayered tissues with maintenance of three discrete cell layers (**Figure 2.4**).

2.4.2 Fabrication of 3D Smooth Muscle Tissues

To demonstrate how the flexible nature of fTNFS allows for fabrication of 3D tissues with control over global cellular orientation, we first aimed to model a simplified tubular structure to mimic the geometry of vascular structures. In blood vessels, vascular tone and blood flow are regulated by SMC contraction and relaxation. Smooth muscle cells make up the medial layer of blood vessels, the *tunica media*, and are organized in a

circumferential pattern [1,29]. To recapitulate architecture of the *tunica media*, we patterned the fTNFS such that the nanogrooves and ridges were parallel to the long axis of the rectangular scaffold. To form a cylinder with circumferentially layered SMC-sheets, the fTNFS were then rolled along the short axis with the cell layers on the inside of the lumen (**Figure 2.7**).

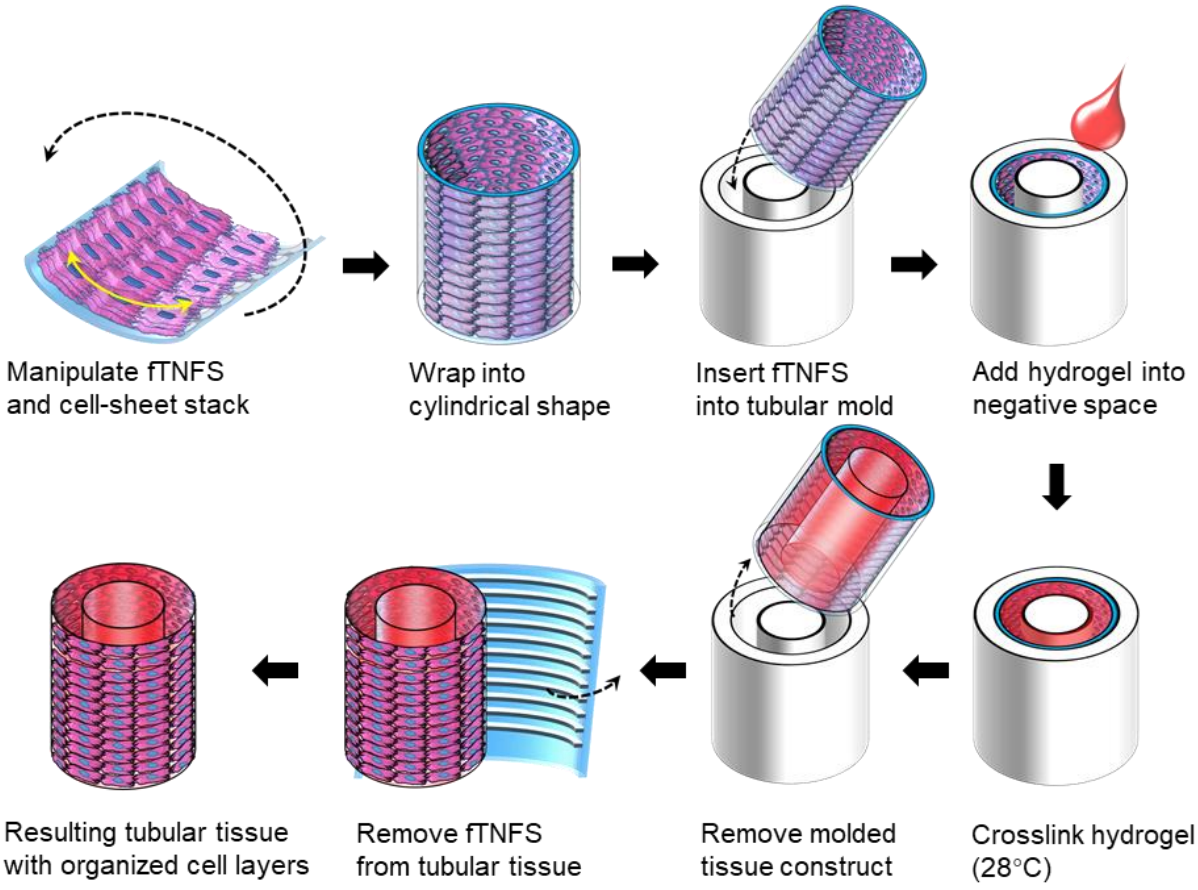

Figure 2.7. Schematic of tubular tissue casting process using multilayered cell-sheet stacks with fTNFS and cylindrical molds.

This cylinder was then inserted into a cylindrical mold with a capped end and center mandrel (**Figure 2.5.A,B**). The void space between the mandrel and the SMC-sheet cylinder was filled with a crosslinking gelatin hydrogel to provide a structured tubular

shape of the final tissue. Finally, the SMC-sheet cylinder and crosslinked hydrogel were removed from the mold followed by the unwrapping of the fTNFS. The resulting tubular tissue possessed a hollow lumen (diameter = 2.0 +/- 0.9 mm) surrounded by hydrogel walls (thickness ~ 800 µm) (**Figure 2.6.A**). The cell layers were wrapped around the outer edge of the hydrogel tube (cell layer thickness = 17 +/- 3 µm) and were not encased by the hydrogel during the casting process (**Figure 2.6.B-C**). The tissue was then gently manipulated with forceps onto a custom tissue housing for culture and visualization with an inverted microscope (**Figure 2.5.C**). After 7 days in culture, SMC tubes were cross-sectioned and histologically stained. Three distinct cell layers were maintained around the outer edge of the hydrogel walls with the center lumen still intact (**Figure 2.6.C**). Furthermore, the cell bodies and their nuclei had maintained circumferential alignment and elongation along the hydrogel's edge after several days in culture.

2.4.3 Fabrication of 3D Cardiac and Skeletal Muscle Tissues

The muscle structures throughout the body have multiple stratified layers of organized cells and varying curved 3D geometries. For example, limb muscles have a spindled shape with tapered ends, while trunk muscles, such as the transvers abdominis and oblique muscles, are curved around the side of the body. Furthermore, cardiovascular and digestive organs possess hollow lumens with layers of organized muscle, such as the stomach and intestines and the chambers of the heart. There have been several approaches to modeling these tissue organizations *in vitro,* such as seeding engineered scaffolds[30–32], 3D bioprinting[13,33], cell sheet layering[26,34–37], and tissue casting[38–41]. However, few of these approaches can recapitulate the anisotropic layering

of organized cell-sheets that ultimately gives rise to tissue functionality. To address this limitation, we sought to apply our fTNFS technology and tissue casting process to fabricating organized multilayered skeletal and cardiac muscle tubes with curved surfaces.

The fTNFS were seeded with either mouse skeletal muscle myoblasts (C2C12 cells) or hiPSC-derived cardiomyocytes and endothelial cells to form organized monolayers. Endothelial cells were included in cardiac monolayers as a stromal cell component which improves the integrity of formed and detached cell sheets through a combination of increased intercellular coupling and additional ECM deposition. In contrast, monolayers of cardiomyocytes alone did not maintain a contiguous cell-sheet during detachment, but rather individual cells pulled away from one another, resulting in the detachment of small clusters (**Figure 2.2**). Skeletal and cardiac monolayers were detached and stacked to create multilayered constructs using our gel-casting process and subsequently cast into tubular geometries as described above. Upon removal from the casting mold and unwrapping of the fTNFS, skeletal and cardiac tubes were found to have global cell coverage on the curved outer edges of the tissues and possessed hollow lumens, similar to the SMC tubes (**Figure 2.8**). Cardiac tubes began coordinated, spontaneous contractions after 1-2 days in culture, demonstrating that the cell-cell connections had been maintained within the cardiac sheets after the casting process.

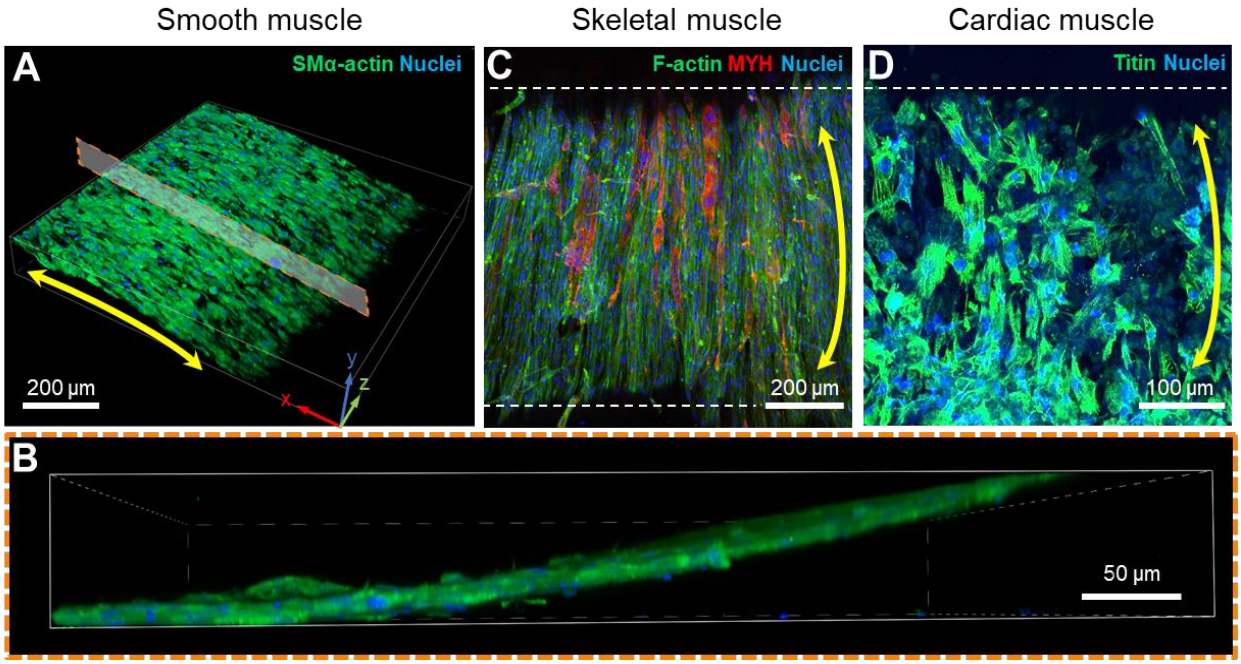

Figure 2.8. Fabrication of patterned 3D tubular tissues with three muscle cell types. (A) 3D rendered image of a confocal z-stack of a smooth muscle cell tube. Image was rotated to show the curvature of the tubular tissue's outer surface. **(B)** Boxed inset of **(A)** showing a cross-sectional view of confocal z-stack demonstrates cell layers are wrapped around the tube's outer edge of the hydrogel. **(C)** Maximum intensity projection of a confocal z-stack taken of a tubular tissue circumferentially patterned with mouse muscle myoblasts (C2C12s) and cultured in differentiation medium to promote fusion of myoblasts into elongated myotubes (MYH, all isoforms). **(D)** Maximum intensity projection of a confocal z-stack taken of a tubular tissue circumferentially patterned with iPSC-derived cardiomyocytes. **(E)** The double-headed yellow arrows denote global circumferential cellular alignment perpendicular to the tube's long axis. Dashed white lines outline the edges of the tubular constructs in **(C)** and **(D)**.

In the case of skeletal muscle tubes, tissues were cultured in a serum-rich (20% FBS) medium for 3-4 days after fabrication to promote additional cell growth before switching into a serum-poor (2% HS) medium. Once is low serum conditions, myoblasts began to fuse into multinucleated myotubes that elongated circumferentially around the tube's curved surface (**Figure 2.8.C**). This result suggests that pre-patterning individual myoblast cell sheets before incorporation into 3D tissues is sufficient to provide robust organizational cues from within the cell-sheet's structure and does not require sustained external cues to generate aligned myotubes. We hypothesize that the deposited ECM

during cell-sheet formation was also organized and provided robust directional cues that promote consistent cellular alignment after casting into a 3D tissue.

We have investigated this hypothesis in a previous study where sheets of aligned C2C12 myoblasts were transferred onto another sheet with either parallel or orthogonal alignment[17]. We found that the alignment of the deposited ECM within each sheet while cultured on fTNFS was maintained after stacking and promoted the formation of parallel or orthogonally organized myotubes within each layer, respectively. Furthermore, in our previous study, sheets of myoblasts stacked in parallel alignment were found to have longer myotubes and higher fusion indices compared to sheets stacked in an orthogonal orientation[17]. Our previous results[17] taken together with those described in this study demonstrate the significant influence that the ECM has on tissue development and structure.

2.4.4 Cellular Organization is Maintained in 3D Tubular Tissues

To investigate if circumferential patterning of cellular alignment was maintained over longer culture periods, smooth, skeletal, and cardiac muscle tubes were cultured for 7 or 14 days. Each engineered tissue was stained for filamentous actin (F-actin) and its organization was quantified using alignment analysis MATLAB scripts as described previously (**Figure 2.9**) [16,27]. Smooth, skeletal, and cardiac muscle tubes demonstrated similar levels of circumferential cellular alignment around the tubes' surfaces (**Figure 6D-I**).

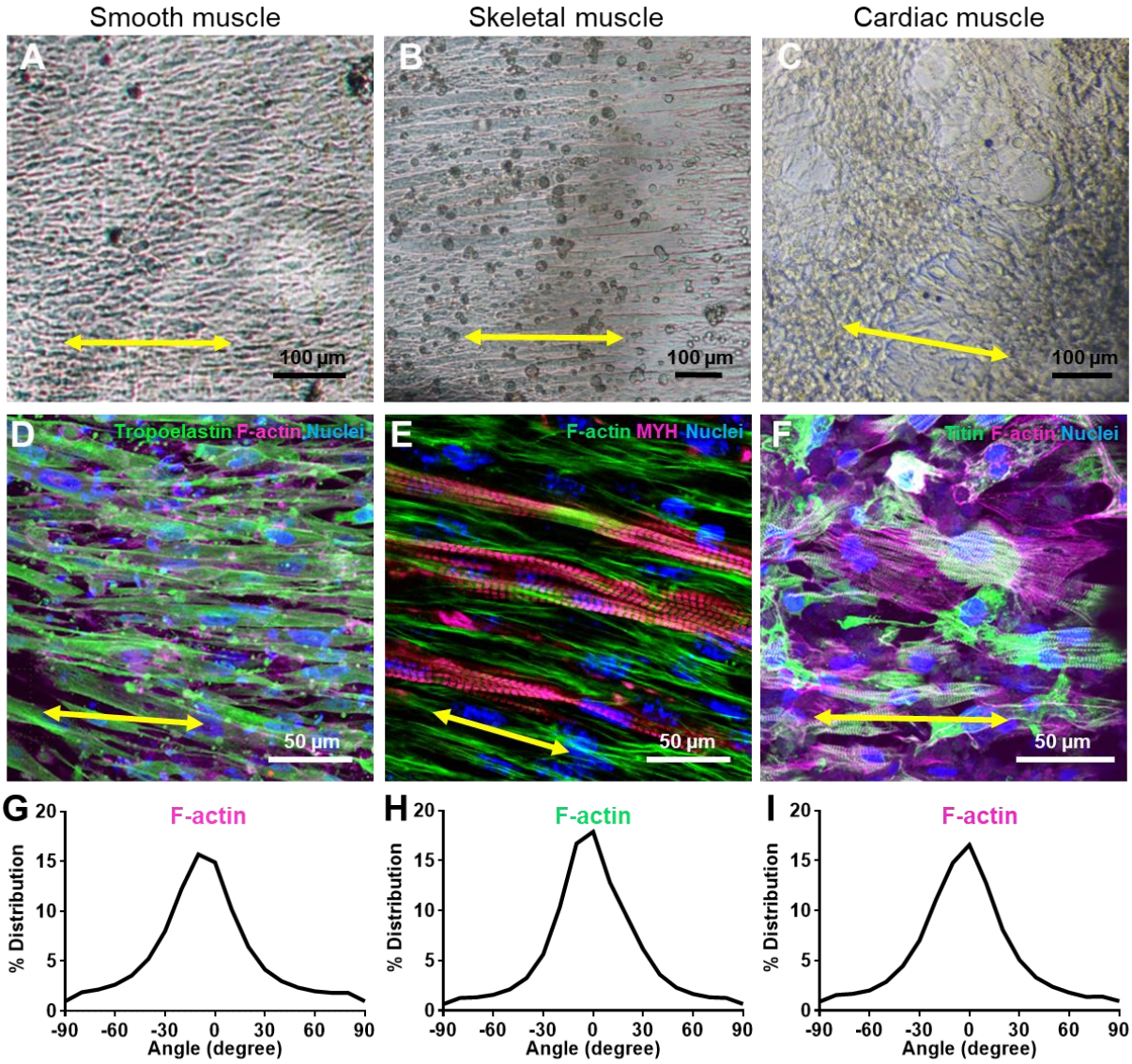

Figure 2.9. Patterned cellular orientation in tubular tissues is maintained after 7 days in culture. (A-C) Brightfield images of smooth **(A)**, skeletal **(B)**, and cardiac **(C)** muscle tubes after 7, 14, or 7 days in culture, respectively. **(D-F)** Confocal images of each tubular tissues imaged in A-C, respectively. Each tissue was immunostained for cytoskeletal and or contractile proteins as listed in the upper right corner of each panel. **(G-I)** Quantitative analysis of filamentous-actin (F-actin) cytoskeletal alignment of cells in each tissue type.

Skeletal muscle tubes showed formation of elongated circumferential myotubes after 3-4 days in culture with medium containing low-serum, which promotes fusion and differentiation of myoblasts [33,42,43]. We observed that myosin heavy chain (MYH, all

isoforms) was expressed throughout fused myotubes at earlier timepoints (**Figure 5C**). However, with application of broad-field electrical stimulation (1 Hz, 10V, 24 ms pulses) no myotube contraction was observed suggesting contractile proteins had not yet been assembled into functional sarcomeres. To promote the formation of functional sarcomeres, we applied chronic broad field stimulation at lower voltages (1 Hz, 3V, 24 ms) 3-5 days after myotube fusion was apparent in differentiation medium conditions, as shown by others [44,45]. As early as 2-3 days after application of chronic electrical stimulation, myotube twitching followed by robust contraction was visualized in sync with the 1 Hz stimulation pacing and halted in the absence of an electrical pulse (**Supplemental video 2.1**). After 9 days of chronic electrical stimulation, registered sarcomeres were easily detectable within myotubes when visualized with immunocytochemistry (**Figure 2.9.E**). Other groups have also substantiated the role of electrical stimulation in the formation of functional skeletal myotubes *in vitro* and have demonstrated that sodium and calcium flux, through voltage-gated ion channels, may be required for Z- and A-band formation [44–47]*.* Together, these data support observations made in this study and suggest that incorporation of both internal and external developmental cues may be required in tissue engineering approaches to recapitulate *in vivo*-like environments and to promote functional maturation.

Cardiac tubes were also subjected to chronic stimulation pulses (1 Hz, 3V, 8 ms) for up to 37 days in culture. After 37 days in stimulated culture, cross-sectional videos of cardiac tubes contracting under broad-field electrical stimulation showed that the hydrogel walls could be deformed during contraction (**Supplemental Video 2.2**). This result demonstrated that patterning and layering aligned cardiomyocytes onto curved three-

dimensional tissues was possible and that their contractile function was maintained in long term culture. In future applications of this technology, long term electrical stimulation protocols with increasingly challenging pacing frequencies could be applied to promote maturation of cardiac tubes as shown by other groups [6,48,49]. It would be interesting to explore if pre-patterning of cardiomyocyte architecture within 3D ventricular models would enhance or accelerate maturation when combined with electrical and or mechanical conditioning. Additionally, this technique provides a novel approach for recapitulating more complex myocardial architectures. For example, in the myocardium of the left ventricle, every four to five layers of cardiomyocytes (or myolaminae) are aligned in a single plane but the alignment direction of each myolamina shifts by approximately 10°. This allows the myocardium to encompass a helical fiber architecture with a 180° range of orientations and efficiently maximize its ejection fraction of blood from the ventricles with each contraction of the heart [50–52]. By patterning and stacking individual sheets of cardiomyocytes, this approach could be used to model microenvironments that cardiomyocytes experience at cleavage planes during contraction. Furthermore, if wrapped into a 3D ventricle shape, this platform could be used to study how varied cardiac tissue organizations contribute to ventricle-level function.

2.5 Discussion

In this study, we developed a novel method for patterning and layering individual cell sheets and casting them into 3D tubular geometries with curved surfaces. We used fabricated custom molds to cast tubular tissues inspired by the vasculature and the curved

tissue structures of the heart ventricles and skeletal muscles in the body's trunk. We found that pre-patterning individual cell sheets promoted cellular alignment in 3D tissues for several weeks after tissue casting. In addition to providing tissue-level alignment cues, we provided broad-field electrical stimulation for skeletal tubes and found that electrical conditioning was required to promote contractile function. These results suggest that a combination of internal and external conditioning cues may be required to further mature tissues fabricated using fTNFS-enabled cell-sheet casting.

Given the versatile nature of our fTNFS platform, this approach be adapted to fabricate uniquely shaped flexible films and tissue-specific shaped molds for even more complex tissue architectures, such as the conical ventricles of the heart. In this study, we created tissues with thicknesses of 3 – 4 cell layers. However, we could also generate thicker tissues that surpass the limits of nutrient and oxygen diffusion and prevent tissue necrosis, by incorporating vascular networks or proangiogenic factors [53]. Providing vascular networks could enable long-term culture of thicker tissues for maturation studies. Additionally, this system could be further adapted by incorporating biochemically tunable hydrogels (e.g. fibrin, photo-crosslinking gels, decellularized-ECM, etc.) for tissue specific customization and or presentation of embedded signaling factors for developmental and maturation studies. Flexible TNFS could enable the fabrication of more advanced engineered tissues that could be used to investigate complex structure-function relationships, development, and maturation in the dish.

2.6 References

1. Patel, A., Fine, B., Sandig, M. & Mequanint, K. Elastin biosynthesis: The missing link in tissue-engineered blood vessels. *Cardiovasc. Res.* **71**, 40–49 (2006).
2. Roostalu, U. & Wong, J. K. Arterial smooth muscle dynamics in development and repair. *Dev. Biol.* **435**, 109–121 (2018).
3. Domenga, V. *et al.* Notch3 is required for arterial identity and maturation of vascular smooth muscle cells. *Genes Dev.* **18**, 2730–5 (2004).
4. Phillips, H. M. *et al.* Disruption of Planar Cell Polarity Signaling Results in Congenital Heart Defects and Cardiomyopathy Attributable to Early Cardiomyocyte Disorganization. *Circ. Res.* **101**, 137–145 (2007).
5. Weinstein, B. M., Stemple, D. L., Driever, W. & Fishman, M. C. gridlock, a localized heritable vascular patterning defect in the zebrafish. *Nat. Med.* **1**, 1143–1147 (1995).
6. Ronaldson-Bouchard, K. *et al.* Advanced maturation of human cardiac tissue grown from pluripotent stem cells. *Nature* **556**, 239–243 (2018).
7. Liau, B., Christoforou, N., Leong, K. W. & Bursac, N. Pluripotent stem cell-derived cardiac tissue patch with advanced structure and function. *Biomaterials* **32**, 9180–9187 (2011).
8. Nunes, S. S. *et al.* Biowire: a platform for maturation of human pluripotent stem cell–derived cardiomyocytes. *Nat. Methods* **10**, 781–787 (2013).
9. Syedain, Z. H., Meier, L. A., Lahti, M. T., Johnson, S. L. & Tranquillo, R. T. Implantation of completely biological engineered grafts following decellularization into the sheep femoral artery. *Tissue Eng. Part A* **20**, 1726–34 (2014).
10. Quint, C., Arief, M., Muto, A., Dardik, A. & Niklason, L. E. Allogeneic human tissue-engineered blood vessel. *J. Vasc. Surg.* **55**, 790–798 (2012).
11. Dahl, S. L. M. *et al.* Readily available tissue-engineered vascular grafts. *Sci. Transl. Med.* **3**, 68ra9 (2011).
12. Skardal, A., Zhang, J. & Prestwich, G. D. Bioprinting vessel-like constructs using hyaluronan hydrogels crosslinked with tetrahedral polyethylene glycol tetracrylates. *Biomaterials* **31**, 6173–6181 (2010).
13. Hinton, T. J. *et al.* Three-dimensional printing of complex biological structures by freeform reversible embedding of suspended hydrogels. *Sci. Adv.* **1**, e1500758 (2015).
14. Lee, A. *et al.* 3D bioprinting of collagen to rebuild components of the human heart. *Science (80-.).* **365**, 482–487 (2019).
15. Miri, A. K. *et al.* Multiscale bioprinting of vascularized models. *Biomaterials* **198**, 204–216 (2019).
16. Jiao, A. *et al.* Thermoresponsive nanofabricated substratum for the engineering of

three-dimensional tissues with layer-by-layer architectural control. *ACS Nano* **8**, 4430–9 (2014).

17. Jiao, A. *et al.* Regulation of skeletal myotube formation and alignment by nanotopographically controlled cell-secreted extracellular matrix. *J. Biomed. Mater. Res. Part A* (2018) doi:10.1002/jbm.a.36351.

18. Penland, N., Choi, E., Perla, M., Park, J. & Kim, D.-H. Facile fabrication of tissue-engineered constructs using nanopatterned cell sheets and magnetic levitation. *Nanotechnology* **28**, 075103 (2017).

19. Callegari, A., Coons, M. L., Ricks, J. L., Rosenfeld, M. E. & Scatena, M. Increased calcification in osteoprotegerin-deficient smooth muscle cells: Dependence on receptor activator of NF-κB ligand and interleukin 6. *J. Vasc. Res.* **51**, 118–31 (2014).

20. Guan, X. *et al.* Dystrophin-deficient cardiomyocytes derived from human urine: New biologic reagents for drug discovery. *Stem Cell Res.* **12**, 467–480 (2014).

21. Lian, X. *et al.* Directed cardiomyocyte differentiation from human pluripotent stem cells by modulating Wnt/β-catenin signaling under fully defined conditions. *Nat. Protoc.* **8**, 162–175 (2012).

22. Palpant, N. J. *et al.* Inhibition of -catenin signaling respecifies anterior-like endothelium into beating human cardiomyocytes. *Development* **142**, 3198–3209 (2015).

23. Palpant, N. J. *et al.* Generating high-purity cardiac and endothelial derivatives from patterned mesoderm using human pluripotent stem cells. *Nat. Protoc.* **12**, 15–31 (2017).

24. Hemmi, N. *et al.* A Massive Suspension Culture System With Metabolic Purification for Human Pluripotent Stem Cell-Derived Cardiomyocytes. *Stem Cells Transl. Med.* **3**, 1473–1483 (2014).

25. Nagase, K., Yamato, M., Kanazawa, H. & Okano, T. Poly(N -isopropylacrylamide)-based thermoresponsive surfaces provide new types of biomedical applications. *Biomaterials* **153**, 27–48 (2018).

26. Takahashi, H. & Okano, T. Thermally-triggered fabrication of cell sheets for tissue engineering and regenerative medicine. *Advanced Drug Delivery Reviews* (2019) doi:10.1016/j.addr.2019.01.004.

27. Cho, H. *et al.* Self-Organization in High-Density Bacterial Colonies: Efficient Crowd Control. *PLoS Biol.* **5**, e302 (2007).

28. Kim, D.-H. *et al.* Guided Cell Migration on Microtextured Substrates with Variable Local Density and Anisotropy. *Adv. Funct. Mater.* **19**, 1579–1586 (2009).

29. Owens, G. K., Kumar, M. S. & Wamhoff, B. R. Molecular Regulation of Vascular Smooth Muscle Cell Differentiation in Development and Disease. *Physiol. Rev.* **84**, 767–801 (2004).

30. Chen, Y. *et al.* Robust bioengineered 3D functional human intestinal epithelium.

Sci. Rep. **5**, 13708 (2015).

31. MacQueen, L. A. *et al.* A tissue-engineered scale model of the heart ventricle. *Nat. Biomed. Eng.* 1 (2018) doi:10.1038/s41551-018-0271-5.
32. Finkbeiner, S. R. *et al.* Generation of tissue-engineered small intestine using embryonic stem cell-derived human intestinal organoids. *Biol. Open* **4**, 1462–1472 (2015).
33. Merceron, T. K. *et al.* A 3D bioprinted complex structure for engineering the muscle–tendon unit. *Biofabrication* **7**, 035003 (2015).
34. Sasaki, D. *et al.* Contractile force measurement of human induced pluripotent stem cell-derived cardiac cell sheet-tissue. *PLoS One* **13**, e0198026 (2018).
35. Sakaguchi, K., Shimizu, T. & Okano, T. Construction of three-dimensional vascularized cardiac tissue with cell sheet engineering. *J. Control. Release* **205**, 83–88 (2015).
36. Juthani, N. *et al.* Infused polymers for cell sheet release. *Sci. Rep.* (2016) doi:10.1038/srep26109.
37. Haraguchi, Y., Shimizu, T., Yamato, M. & Okano, T. Scaffold-free tissue engineering using cell sheet technology. *RSC Advances* (2012) doi:10.1039/c2ra00704e.
38. Tiburcy, M. *et al.* Defined Engineered Human Myocardium With Advanced Maturation for Applications in Heart Failure Modeling and Repair. *Circulation* **135**, 1832–1847 (2017).
39. Li, R. A. *et al.* Bioengineering an electro-mechanically functional miniature ventricular heart chamber from human pluripotent stem cells. *Biomaterials* (2018) doi:10.1016/j.biomaterials.2018.02.024.
40. Maffioletti, S. M. *et al.* Three-Dimensional Human iPSC-Derived Artificial Skeletal Muscles Model Muscular Dystrophies and Enable Multilineage Tissue Engineering. *Cell Rep.* **23**, (2018).
41. Zhou, W. *et al.* Multifunctional Bioreactor System for Human Intestine Tissues. *ACS Biomater. Sci. Eng.* **4**, 231–239 (2018).
42. Matsumoto, T. *et al.* Three-Dimensional Cell and Tissue Patterning in a Strained Fibrin Gel System. *PLoS One* **2**, e1211 (2007).
43. Xu, B. *et al.* Nanotopography-responsive myotube alignment and orientation as a sensitive phenotypic biomarker for Duchenne Muscular Dystrophy. *Biomaterials* **183**, 54–66 (2018).
44. Fujita, H., Nedachi, T. & Kanzaki, M. Accelerated de novo sarcomere assembly by electric pulse stimulation in C2C12 myotubes. *Exp. Cell Res.* **313**, 1853–1865 (2007).
45. De Deyne, P. G. Formation of sarcomeres in developing myotubes: role of mechanical stretch and contractile activation. *Am. J. Physiol. Physiol.* **279**, C1801–C1811 (2000).

46. Hara, M. *et al.* Calcium influx through a possible coupling of cation channels impacts skeletal muscle satellite cell activation in response to mechanical stretch. *Am. J. Physiol. Physiol.* **302**, C1741–C1750 (2012).

47. Cooper, S. T. *et al.* C2C12 Co-culture on a fibroblast substratum enables sustained survival of contractile, highly differentiated myotubes with peripheral nuclei and adult fast myosin expression. *Cell Motil. Cytoskeleton* **58**, 200–211 (2004).

48. Physiologic force-frequency response in engineered heart muscle by electromechanical stimulation. *Biomaterials* **60**, 82–91 (2015).

49. Radisic, M. *et al.* Functional assembly of engineered myocardium by electrical stimulation of cardiac myocytes cultured on scaffolds. *Proc. Natl. Acad. Sci. U. S. A.* **101**, 18129–34 (2004).

50. Streeter, D. D. & Bassett, D. L. An engineering analysis of myocardial fiber orientation in pig's left ventricle in systole. *Anat. Rec.* **155**, 503–511 (1966).

51. Pope, A. J., Sands, G. B., Smaill, B. H. & LeGrice, I. J. Three-dimensional transmural organization of perimysial collagen in the heart. *Am. J. Physiol. Circ. Physiol.* **295**, H1243–H1252 (2008).

52. Ae, D. J. H. & Anderson, R. H. The Development and Structure of the Ventricles in the Human Heart. doi:10.1007/s00246-009-9390-9.

53. Sekine, H. *et al.* In vitro fabrication of functional three-dimensional tissues with perfusable blood vessels. *Nat. Commun.* **4**, (2013).

Chapter 3. Engineered 3D Human Cardiac Ventricular Models with Controllable Architecture for Study of Myocardial Structure-Function Relationships

3.1 Abstract

Tissue engineering combined with human induced pluripotent stem cell derived cardiomyocytes (hiPSC-CMs) poses unique opportunities for modeling cardiac tissue function and disease in the dish. However, there are few approaches available that can recapitulate the complex structure-function relationships that govern cardiac function at the macroscopic organ level. Here, we report a scaled human 3D ventricular model using patterned cardiac sheets, where the global organization of each model was engineered to mimic either the longitudinal, diagonal (angled), or circumferential cellular alignment present within the different layers of native heart muscle. Surprisingly, in ventricular models pre-patterned with circumferential orientation, but not in those with longitudinal, diagonal, or random organizations, we observed spontaneous cellular remodeling from circumferential to longitudinal alignment over time. We further explored this effect through finite element model analysis and found that cellular remodeling might occur to avoid high longitudinal shear forces that are perpendicular to the initial circumferential cellular orientation. Furthermore, cells may align parallel with the high longitudinal shear stress to reduce perpendicular shear stress. This study provides an advanced platform for examination of human cardiac biomechanics in a 3D physiological setting and could offer insight into how the embryonic heart establishes its helical muscle architecture.

3.2 Introduction

With every contraction, the heart exhibits a unique pumping function where the muscle fibers shorten, thicken in diameter, and elicit a twisting motion of the whole organ. Torsional movement is afforded by the distinctive double helix pattern of myofibrils throughout the thickness of the myocardium, where the orientation of muscle fibers exhibits a shift from a right-handed to a left-handed helix from the epicardium to the endocardium[92]. This twisting motion is like the energetic winding of a spring and is critical for suitable ejection of blood from the ventricles and therefore proper heart function. Subsequently, when the mechanics of this motion are disrupted by disease or injury, heart function is compromised. For example, myocardial disarray is associated with several forms of cardiomyopathy (e.g. dilated, hypertrophic, or infarction) and is often accompanied by structurally disruptive fibrotic scaring throughout the muscle[90,91,187].

Tissue engineering strategies combined with human induced pluripotent stem cell (hiPSC) technology have enabled the development of diverse approaches for modeling structural and functional characteristics of cardiac tissue[17]. These efforts have provided complementary platforms to animal models for modeling human cardiomyopathies and drug cardiotoxicity testing in the dish[16]. However, most approaches yield two-dimensional (2D) laminar tissues or 3D structures that the lack structural complexity of the myocardium. It is possible that by recapitulating heart's anisotropic organization will produce cardiac tissues with greater physiological maturity and therefore superior models for the study of cardiovascular development, function, and disease. However, there are few approaches that can recapitulate numerous aspects of the heart's multi-scale

organization within a single platform[130,138,139,153], such as cardiomyocyte anisotropy and the 3D conical geometry of the ventricles.

To address this gap of suitable technologies, we previously developed a cell-sheet engineering approach utilizing flexible thermoresponsive nanofabricated substrates (fTNFS) to enable production of 3D tissues with organized cellular architecture[128]. In this study, we adapted this platform to engineer scaled cardiac ventricular models with controllable architecture for study of the structure-function relationships within the myocardium. Relative to the short axis of the heart, the myofibers are orientated starting at -60° on the epicardial surface and shift to a +60° at the endocardial surface[93,94]. We chose to recapitulate three main structural patterns of the myocardial helix within our 3D tissue models: circumferential (0°), angled (45°), and longitudinal (90°) cell orientations, and compare their function to an isotropic control group with random cellular patterning. We hypothesized that anisotropic tissue architectures would outperform isotropic ones due to cellular organization and more efficient distribution of force produced during contraction. We found that each of the tissue patterning schemes was possible with this approach and that the tissues were spontaneously active. Interestingly, we observed a striking transmural remodeling effect in the circumferentially patterned group, where the innermost cell layers of the tissue reoriented perpendicularly to their original orientation. Computational modeling using finite element analysis revealed gradient patterns of transmural shear stress and strains perpendicular to circumferential tissue organizations, but not in the other groups. These large opposing or perpendicular shear forces may be drivers of this remodeling behavior. Upon further functional evaluation using pressure-sensing catheters, we found that the remodeled and longitudinally patterned tissues were

functionally superior to isotropic and angled tissues. Taken together, these results supported the hypothesis that 3D anisotropic tissue organization affords functional benefit and creates complex patterns of mechanical cues that promote coordinated cellular remodeling. These findings have implications for how spatial patterns of mechanical forces present in 3D tissue microenvironments and might provide organizational cues during cardiac morphogenesis and development.

3.3 Materials and Methods

3.3.1 Fabrication of Flexible Thermoresponsive Nanofabricated Substrates (fTNFS)

To enable the production of cardiac ventricular models with anisotropic cellular organization, flexible films with nanoscale topographical cues and thermoresponsive properties were fabricated as previously described [11,30]. Briefly, 100 µL of a UV-curable polyurethane acrylate (PUA) polymer (Norland Optical Adhesive #76) mixed with 1% w/w glycidyl methacrylate (GMA) was sandwiched and spread between a flexible polyethylene terephthalate (PET) film (5 x 5 cm) and a PUA master mold with nanoscale parallel ridges and grooves (800 x 800 x 600 nm, w x h x d). The PUA-GMA polymer mixture was flash cured under high-intensity UV light (365 nm) and the flexible film now with nanoscale features was removed from the master mold and placed under low-intensity UV bulbs overnight for final curing. The nanopatterned flexible films were then washed with an amine-terminated poly(N-isopropylacrylamide) (pNIPAM) solution (13 µM in H_2O, M_n = 2500 Sigma-Aldrich) for 24 hours on a tabletop rocker (55 rpm, room temperature) to

provide thermoresponsive surface functionalization. The flexible thermoresponsive nanofabricated substrates (fTNFS) were then rinsed in deionized water (DI-H_2O) to remove excess pNIPAM).

Flexible TNFS were cut into fan shapes (radius = 12 mm, θ = 135°, area = 1.17 cm^2) using a die cutter to produce substrates with nanogrooves aligned at either a 0°, 45°, or 90° angle relative to the x-axis (**Figure 1B**). Cut fTNFS were affixed to custom fan-shaped polydimethylsiloxane wells (PDMS, Sylgard 181) using a UV curable adhesive (Norland Optical Adhesive #83H). Wells were made only 10% larger in dimension than the fTNFS to control the cell seeding area and minimize superfluous cell waste by seeding unusable surface area. Culture wells were rinsed with DI-H_2O before UV sterilization (294 nm) for 4+ hours in a biosafety cabinet. Sterilized culture wells were treated with fetal bovine serum (FBS, Sigma) overnight at 37°C before cell seeding to promote cellular attachment.

3.3.2 Pluripotent Stem-Cell Culture and Differentiation

A human urine-derived induced pluripotent stem cell line (hiPSC UC 3-4, wild-type, male) was generously developed and donated by David Mack for differentiation of cardiomyocytes (CMs) and endocardial-like endothelial cells (ECs)[31]. Production CMs and ECs was performed using well established monolayer-based directed differentiation protocols[32,33]. Briefly, hiPSC colonies were expanded to 80% confluency on Matrigel-coated plates (1:60, Corning), dissociated, and re-plated at either a high (270 k/cm^2) or low (100 k/cm^2) density for directed differentiation of CMs or ECs, respectively. High-density monolayers were cultured for 48 hours in mTeSR medium (STEMCELL

Technologies) before induction (day 0) of mesoderm specification with 10 μm CHIR-99021 (Fischer Technologies) in Roswell Park Memorial Institute 1640 (RPMI) medium with B27 supplement without insulin (Gibco). To further specify cardiomyocyte lineage, high-density monolayers were exposed to the Wnt-inhibitor IWP4 (Stemgent) on day 3 in RPMI + B27 without insulin and cultured with RPMI + B27 with insulin from day 7 onwards. To purify differentiation populations for CMs, cardiac differentiated cultures re-plated and exposed to a glucose-poor and lactose-rich medium on day 14 for two days or until only beating cells remained. Cells were harvested on day 17 or later and stained for cardiac-specific markers using a fluorescently conjugated antibody (anti cardiac troponin T (cTnT) – Alexa fluor 488, 1:100, Thermo-Scientific) for flow cytometry. Only populations of ≥ 95% cTnT-positivity were used for this study.

Simultaneously, low-density hiPSC monolayers were cultured for 24 hours in mTeSR medium with 1 μm CHIR-99021 after re-plating before induction with activin-A (R&D Systems) and Matrigel (1:60) in RPMI + B27. 18 hours post-induction, low-density cultures were exposed to bone morphogenic protein-4 (BMP-4; R&D Systems) and CHIR-99021 in RPMI-B27 medium to specify for cardiac mesoderm lineages. To further select for cardiac endothelial populations, cells were incubated with StemPro-34 medium from days 2 to 5 with a cocktail of growth factors: vascular endothelial growth factor (VEGF; PeproTech), BMP-4, basic fibroblast growth factor (bFGF; R&D Systems), ascorbic acid, and monothioglycerol. On day 5, monolayers were dissociated and r-plated at a lower density (13k/cm^2) on 0.1% gelatin-coated plates in Endothelial Growth Medium-2 (EGM-2, Lonza) supplemented with VEGF, bFGF, and CHIR-99021 until day 11/12. EC population purity was evaluated on day 11/12 via live-cell flow cytometry using an anti-

CD31 – Alex 488 conjugated antibody (1:100, R&D Systems). Only EC populations with ≥ 90% CD31-positivity were used for this study.

3.3.3 Serial-seeding of fTNFS with hiPSC-CMs and ECs

To eliminate confounding factors of cell age and maturation, CMs and ECs used between days 17-25 and 12-14, respectively. CMs and ECs were dissociated separately and mixed together such that final population was 89% CMs and 11% ECs (~7:1, CMs:ECs), as previously described[11]. The cell mixture was seeded onto FBS-treated fTNFS between 175 and 185 k/cm2 in 120 µL of cardiac growth medium (75% RPMI-B27 + insulin, 25% EGM-2, 10% FBS, 1% penicillin/streptomycin) to form a highly confluent monolayer (day 0). The cell mixture was cultured overnight at 37°C, 5% CO_2 to allow for maximum cell adhesion to the fTNFS, mechanosensation of the nanotopography, and cellular elongation along the nanogrooves and ridges (**Figure 3.1**).

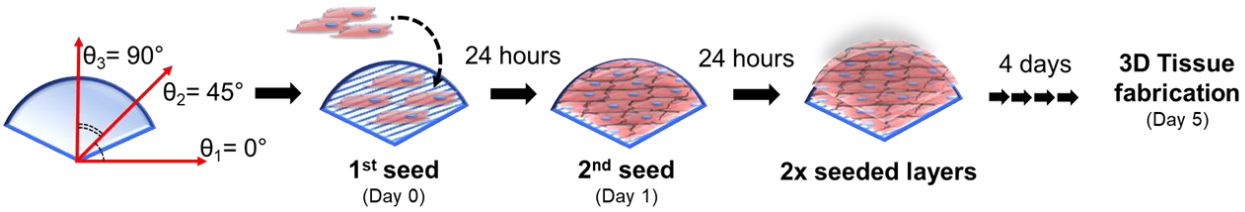

Figure 3.1. Experimental timeline for 3D ventricle model fabrication.

18-24 hours after the first seeding event (day 1), additional CMs and ECs were dissociated and mixed again at a 7:1 ratio as described above. The excess medium and

non-adherent cells was aspirated from the fTNFS surface and replaced with 120 µL of a second CM-EC cell suspension to provide another layer of cells between 175 and 185 k/cm^2. The twice-seeded or serial-seeded fTNFS was cultured overnight at 37°C, 5% CO_2 to allow for cell-cell adhesion to occur between the first and second seeded layers before addition of 2 mL of warmed (37°C) cardiac growth medium (day 2). Serial-seeded cell layers were cultured for an additional 4-5 days to allow for formation of aligned cardiac sheets with coordinated beating patterns before use in fabrication of 3D ventricular models.

3.3.4 Custom Models for Fabrication of 3D Ventricular Models

Modular 3D-printed molds were designed in a computer aided design software (Solidworks, Autodesk) and fabricated using a 3D-printer (CUBICON Style) and acrylonitrile butadiene styrene filament (Makerbot). The mold pieces were printed with a 0.1 mm line thickness and brushed with acetone before use to minimize the ridges formed by the layer-by-layer printing process. A modular design was incorporated to aid in mold disassembly and tissue extraction after fabrication (**Figure 3.2**). The assembled molds contained a hollow conical lumen (D_{base} = 6 mm, H = 7 mm) which was used to cast a tissue with a conical geometry that is similar to the left-ventricle of the heart. The final tissue product was on scale to a whole mouse heart[14].

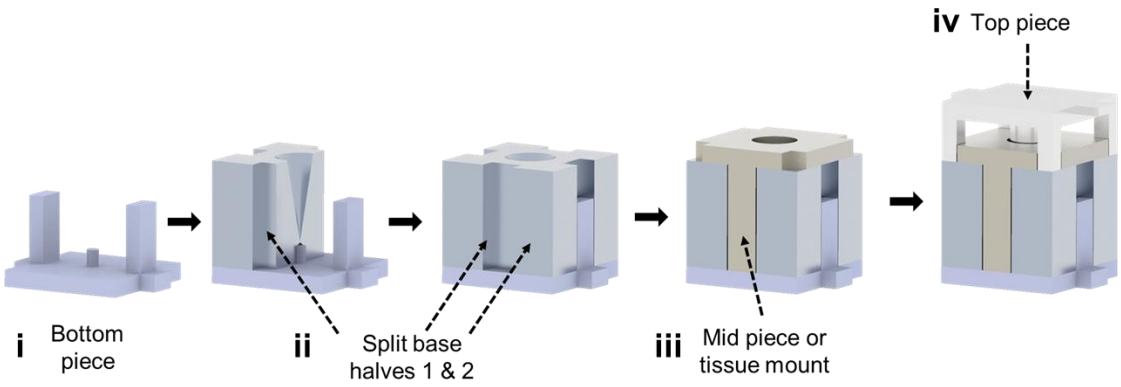

Figure 3.2. Assembly of custom conical molds for 3D ventricular tissue fabrication. (i) The bottom mold piece is used as a platform to assemble the two base pieces **(ii).** The base pieces join to create a conical lumen into which the fTNFS and cell sheets are folded and inserted into. A mid piece or tissue mount **(iii)** is inserted over top of the conical hole to prevent the fTNFS and cell sheets inside from springing out. Finally, the top piece **(iv)** acts as a positive mold to create a hollow lumen in the final tissue.

3.3.5 Fabrication of 3D Cardiac Ventricular Models from Organized Cardiac Sheets

Organized cardiac sheets with spontaneous and synchronous beating patterns were formed after five days in culture on the fTNFS. Before tissue casting, 3D-printed mold pieces were pre-sterilized with 70% ethanol and submerged in hydrophobic pluronic F-127 (5% in DI-water, Sigma) for at least 20 minutes to prevent the tissues from attaching to the molds. However, the tissue mounting pieces (**Figure 3.2.iii**) were not coated with pluronic F-127 to promote the tissue to adhere to this piece for future handling and culture. The submerged pieces were removed and allowed to dry in a sterile biosafety cabinet (BSC) for at least 5 minutes before assembly and tissue casting. Meanwhile, cardiac sheets were incubated with room-temperature phosphate buffer saline (PBS, Sigma) for 10 minutes to initiate partial cell sheet detachment from the fTNFS. The fTNFS was removed from the PDMS culture wells using forceps to hold one corner of the fan-shaped

pattern. The fTNFS were dabbed onto a sterile Kimwipe to remove excess PBS and another pair of forceps was used to grasp the other corner of the flexible pattern. Carefully, the two opposing corners were brought together and overlapped to create cone shape (**Figure 3.3.**) and inserted into the complementary conical mold. One pair of forceps was used to hold the fTNFS in the mold while another was used to insert the uncoated tissue mount overtop of the conical opening, fastening the fTNFS in place. To create a fibrin hydrogel scaffold, 18 µL of thrombin (50 units/mL, Sigma) was mix with 300 µL of fibrinogen (20 mg/mL, Sigma) and 200 µL of the thrombin/fibrinogen mixture was quickly pipetted into the open mold as to fill the entire well. Finally, the top mold piece was inserted through the mold's opening and into the conical well, pushing excess fibrin out and causing it to flow into the remaining negative space of the mold. This overflow was essential for attaching the final casted tissue onto the tissue mount for future culture purposes.

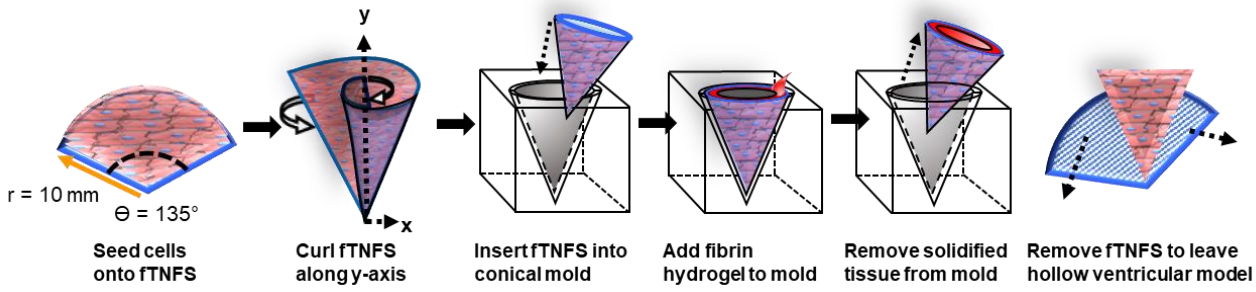

Figure 3.3. Schematic of 3D ventricle model fabrication from fTNFS using custom molds and fibrin hydrogel.

The fully assembled mold containing the fTNFS and cell sheets was placed into a humidified 37°C incubator for 1 hour to allow for the thrombin/fibrinogen mixture to fully polymerize into a fibrin hydrogel scaffold within the mold. The mold-fTNFS-cell sheets assembly was then moved back into a BSC to remove only the top and bottom portions

of the mold. The remaining mold-fTNFS-cell sheet assembly was then submerged in cardiac growth medium and cultured overnight at 37°C, 5% CO_2 to allow for the cell sheets to adhere to the newly polymerized fibrin hydrogel scaffold. After incubation, the mold was submerged in cold (4°C) medium and incubated at 4°C for 20 minutes to promote complete cell sheet detachment from the fTNFS. The mold was then fully disassembled and the fTNFS were removed leaving behind the tissue mount with a hollow, ventricle-shaped tissue and organized cell sheets wrapped around the outside walls of the fibrin hydrogel scaffold. The tissues were placed into 6 well plates with 9 mL of fresh medium for further culture.

3.3.6 Tissue Culture and Electrical Field Stimulation

After tissue casting (day 0) and extraction from the molds (day 1), ventricular models were cultured for an additional 24 hours before proving electrical field stimulation on days 2-4. On day 2, tissues were exposed to a 1 Hz pacing frequency (10 ms pulses, 3 V) for 24 hours and then increased to 1.5 Hz for an additional 1-2 days before functional measurements were taken on days 3-5 of culture.

3.3.7 Functional Assessment of Ventricular Models

After 4 days in culture, ventricular models were functionally evaluated using pressure-sensing catheters and echocardiography measurements. First, the ventricular models were transferred onto a custom 3D-printed stand within a 6 well-plate such that the tissues were positioned vertically with the base and the opening of the tissues' lumen

were at the highest point and the apex hung below. The wells were filled with warmed Tyrodes solution (pH 7.4) and a thin PDMS gasket was placed over the opening of the tissue's lumen at the base to create a closed-volume system. A small x-shaped slit was cut into the PDMS gasket to allow for the tip of a pressure sensing catheter (Millar SPR-671) to be threaded into the lumen of the tissue (Figure 6). Spontaneous pressure recordings were taken of each tissue to evaluate a baseline beat frequency using the Lab Chart Pro software (ADI Instruments). Platinum stimulating electrodes (⌀ = 0.5 mm) were then placed on either side of the tissue stand (15 mm apart) and the tissues were paced at 1 Hz with 10 ms pulses at 10 V. Pressure recordings were taken at 1 Hz for one minute before the pacing frequency was increased by 0.5 Hz and pressure production was recorded for another minute. This incremental pacing scheme was continued until the tissue could no longer capture at the challenging pacing frequency.

3.3.8 Analysis of Pressure Production Data

Spontaneous and electrically paced pressure recording events were parsed and exported from the LabChart Pro software as .csv files and imported into MATLAB (MathWorks) for analysis. A custom MATLAB script was used to find maximum peaks within each dataset and locate the preceding troughs to find the minimum peaks. The amplitudes of the minimums were subtracted from the maximum pressure peaks to calculate a pressure amplitude. The average pressure values at a 1 Hz pacing frequency for each tissue group (isotropic, patterned 0°, 45°, 90°) were averaged and compared using a one-way ANOVA and a Tukey's multiple comparisons test (alpha = 0.05) (**Figure 6C**). Similarly, spontaneous and maximum capture rates for each group were averaged

and compared using a one-way ANOVA and a Tukey's multiple comparisons test (alpha = 0.05).

Tissues were also evaluated for their contractility through their ability to generate pressure over time during systole and diastole, or $\Delta P/\Delta t$. In the LabChart software, the first derivative of the raw pressure signal ($\Delta P/\Delta t$) was calculated for each tissue under each pacing frequency and averaged over the one-minute trace. The data were exported as a .csv file and imported into Prism where the average contraction and relaxation values for each group (isotropic, patterned 0°, 45°, 90°) were compared using a two-way ANOVA and Tukey's multiple comparisons test (alpha = 0.05).

3.3.9 Compression Testing of Fibrin Gels

Compressive moduli of hydrated and crosslinked fibrin hydrogels (20 mg/mL) were measured using an Instron 5900 Series Universal Testing System equipped with a 10 N static load cell. Samples 5 mm in height and 6.8 mm in diameter were compressed at a rate of 10 mm/min until failure.

3.3.10 Finite Element Model

An axisymmetric finite element model of the conical tissue was built in ANSYS to understand the realignment of tissues observed experimentally. The geometry shown in Figure 5 consisted of an inner fibrin layer 250 microns thick and an outer cardiomyocyte cell layer 70 microns thick. The inner diameter at the base was 5 mm and the length of the tissue from base to apex was 7 mm. A 2-degree wide slice was meshed with 32,026

nodes and 4,390 quadratic 3D solid elements (SOLID186 in ANSYS), and cyclic periodicity was applied with 180 repeats to model the full conical shape. Considering the small deformations of the conical tissues observed experimentally, an isotropic elasticity was applied to both the fibrin and cell layers with a Young's modulus of 6.6 kPa and 20 kPa, respectively, and a nearly incompressible Poisson's ratio of 0.49. Fibrin stiffness was determined experimentally through compression testing, as described above. To simulate contraction of the cardiomyocyte cell layer, a negative strain was applied to the cell layer causing either unidirectional or isotropic contraction. The direction of the contractile strain was rotated to replicate all experimental orientations, and the amount of strain was chosen such that the apex displacement of the model matched the experimental data for the 1-day old tissues with longitudinal orientation (**Supplemental Video 3.1**).

3.3.11 Histological Sectioning and Staining

Tissues were fixed after 4 days in culture in 4% paraformaldehyde for 24 hours at 4°C before serial dehydrations in 30% to 100% ethanol, increasing the concentration by 10% with each wash. Each tissue was then embedded in paraffin wax and 4 µm-sections with taken in either the longitudinal or transverse directions to visualize cellular alignment and thickness, respectively. Sections were stained with hematoxylin and eosin to visualize extracellular matrix and cytoplasm (red) and DNA (blue).

3.3.12 Immunofluorescent Staining and Confocal Imaging

Tissues were fixed in 4% paraformaldehyde for 24 hours at 4°C before immunocytochemistry was performed. Tissues were permeabilized in a phosphate buffered saline (PBS) solution with 0.2 % Triton-X 100 (Sigma-Aldrich, 9002-93-1), 5% goat serum, and 0.5% bovine serum albumen (BSA, Sigma-Aldrich A7906) for one hour at room temperature. After three, five-minute PBS washes, the tissues were incubated with an antigen blocking buffer (1.5% goat serum, 0.2% Triton-X 100) for two hours at room temperature to minimize non-specific antibody binding. Primary antibodies specific to sarcomeric titin and raised in rabbit (Myomedix, 1:300) were applied in a staining solution (0.2 % Triton-X, 1.5% goat serum) and incubated overnight at 4°C. The next morning, excess primary antibodies were removed through three serial PBS washes before the secondary antibody (Alexa Fluor 647 donkey anti rabbit, 1:200) and fluorescently conjugated phalloidin (Invitrogen A12379, 1:200) were added. Tissues were incubated with secondary antibodies for two hours at room temperature in the dark before staining for nuclei DAPI (Invitrogen, D1306).

To aid in visualization of the large tissue surface area, the stained ventricular models were gently flattened and sandwiched between two glass coverslips using a think (~3 mm) PDMS gasket with Vectashield anti-fade mounting medium (Vectro Labratories, H-1000-10). The tissues were then imaged using low- and high-powered objectives (20x air, 40x water immersion lens) and a SP8 Leica confocal microscope. Large-area stitched z-stacks were taken of the entire visible tissue area using the 20x-magnificaiton objective. For more detailed analysis of the cellular and cytoskeletal structure through the tissue walls, 40x-magnificaition z-stacks were taken at several locations across the tissue.

3.3.13 Analysis of Cellular Organization

40x-magnificaiton confocal z-stacks were taken across the tissue surface (at least three) to survey transmural cellular alignment in the top (base), middle, and bottom (apex) sections (**Figure 3.4**).

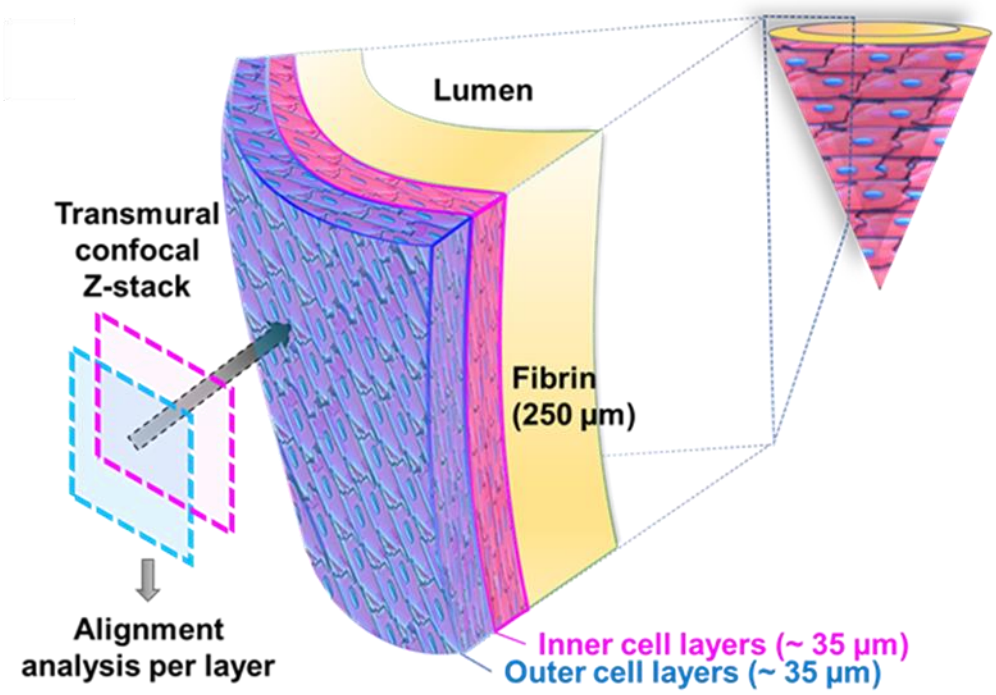

Figure 3.4. Schematic of transmural image acquisition and alignment analysis.

The z-stack depths were parsed into quarters and the outer and inner 25% (~20 µm thick) were separated out. These sections were used to create a maximum intensity projections (MIP) representing the outer cell layers closest to the surface and inner cell layers closest to the fibrin wall of the tissue. Cellular alignment was determined for each of these MIPs based on alignment of the filamentous actin (F-actin) cytoskeleton using a

modified MATLAB script as previously described [11,30,35]. Briefly, this script uses a low-pass Gaussian filter and edge detection to create a 2D convolution from which vertical and horizontal edges are detected using a Sobel filter [34]. These vectors are then used to calculate gradient magnitudes across each pixel within an image. The images are thresholded to define the edges of single cells or groups of cells and calculate their orientation angle between -90° and +90° relative to the x-axis at 0°. The total orientation angles detected within the image are binned and normalized using the probability density function in MATLAB (normpdf). The bin with the maximum distribution percentage was identified and its corresponding orientation angle was utilized as the principle direction of cellular alignment for that image. To determine the cellular organization relative to the tissue's own short axis rather than the arbitrary x-axis of the image acquisition, the degree of offset between the tissue's short axis and the image's x-axis was subtracted or added to each principle angle. The principle angle was determined for three images per tissue and averaged to determine the global cellular organization of each tissue. The principle orientation angle was determined for both the outer and inner layers of each tissue and compared for each tissue group and across groups using a one-way ANOVA and Tukey's multiple comparisons test (alpha = 0.05).

To determine the strength of cellular alignment around the principle orientation, or how wide or narrow the angle distribution was about the mean, we calculated the standard deviation values for each image's distribution. We compared average standard deviation values of the inner and outer layers within each group and between groups using a one-way ANOVA and Tukery's multiple comparisons test (alpha = 0.05). We interpreted low standard deviation values closer to mean that the distribution is narrower, or has a more

prominent peak, which meant that the cells in that image were more aligned in the principle or mean direction. Whereas larger standard deviation values meant that the distribution was wider, and the cells were less aligned in the principle direction.

3.4 Results

3.4.1 Fabrication of Functional Cardiac Ventricular Models

To investigate the 3D macroscopic structure-function relationships within the human myocardium, we adapted our previously developed flexible thermoresponsive nanofabricated substrates (fTNFS) to engineering scaled models of the human left ventricle (**Figure 3.5**)[11].

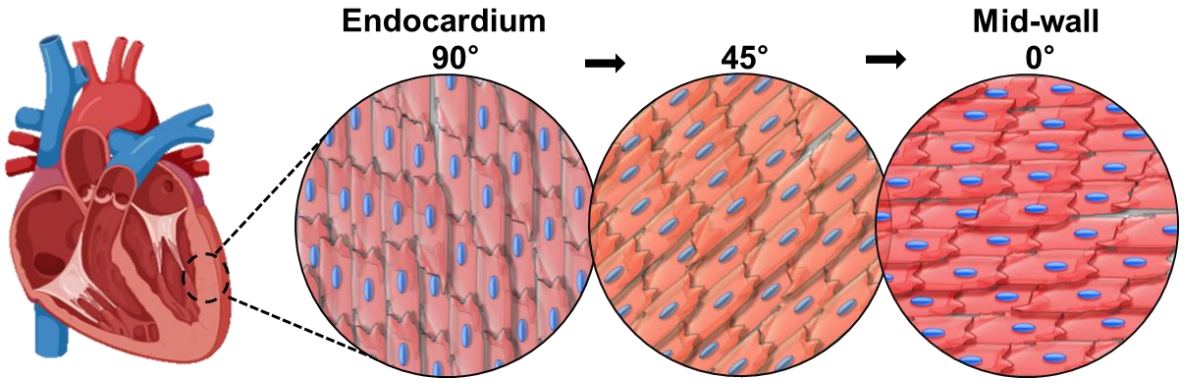

Figure 3.5. Helical myocardial organization possesses multiple cellular organizations. Inspired by the layered organization of the myocardium, we chose to model three main cellular organizations in this study: longitudinal (90°), angled (45°), and circumferential (0°).

The flexible TNFS were cut into fan shapes such that the nanoridges and grooves were oriented in at 90°, 45°, or 0° angle relative to the scaffold's long axis (**Figure 3.1 and 3.3**) to enable the production of 3D ventricular models with longitudinally, angled, or circumferential cellular patterning, respectively. Unpatterned or topographically flat

scaffolds were utilized to create models with random or isotropic cellular organization as a control. Each fTNFS was double seeded with induced pluripotent stem cell-derived (iPSC) cardiomyocytes and endothelial cells to form aligned cardiac sheets that exhibited coordinated spontaneous contraction patterns within 5 days of culture. The organized cardiac sheets were casted with a fibrin hydrogel (20 mg/mL) and custom molds (**Figure 3.2**) to fabricate hallow ventricular models that were on scale with the mouse heart[14]. The final dimensions were 7 mm in height, 5 mm in diameter at the base and tapered to a rounded point at the apex (**Figure 3.6**). The tissues exhibited coordinated spontaneous contractions within one hour after removal from the mold where the apex was pulled upward and inward towards the tissue's base which was attached to a tissue mount (**Supplemental Video 3.2**). This synchronized contraction suggested the cell layers were intact and formed a syncytium (**Figure 3.6.B**). When examined with histological staining and sectioning the tissue wall thickness was approximately 320-330 µm wide consisting of a 250 µm-thick fibrin wall encircled by 4-5 cell layers (70-80 µm thick) (**Figure 3.6.C**).

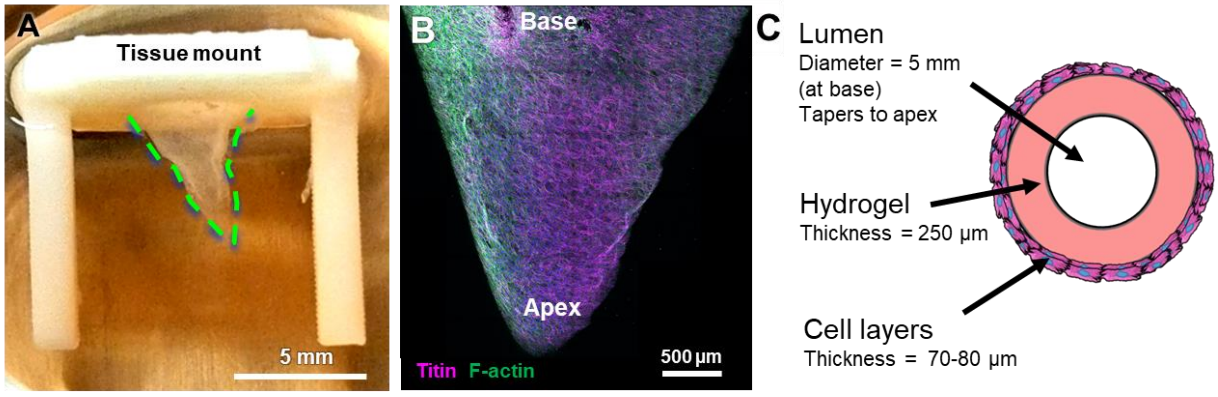

Figure 3.6. Characterization of 3D ventricular models. (A) Representative image of engineered ventricular model attached to a tissue mount in culture. Tissues exhibited spontaneous contractions within one hour after removal from the molds (**Supplemental Video 3.2**). **(B)** 3D confocal z-stack projection of a circumferentially patterned ventricular model immediately after fabrication (day 0). The tissue was stained

for sarcomeric protein titin (magenta) and filamentous actin fibers (F-actin, green). **(C)** Schematic of ventricular model cross-section.

3.4.2 Cellular Organization in 3D Ventricular Models Can Be Anisotropically Patterned

Immediately after fabrication (day 0), ventricular models with random, circumferential, angled, and longitudinal patterning were fixed and stained to evaluate their macro- and microscopic cellular organization after the tissue casting process. High-magnification confocal z-stacks were taken across the entire tissue area and transmurally through the cell layers. To determine if cellular organization was transmurally uniform, the outer and inner halves (~35 μm each, 2 cell layers thick) of the z-stacks were parsed, analyzed separately, and compared. The average cellular orientation for each group generally agreed with the intended tissue patterning scheme such that the circumferential, angled, and longitudinal groups had orientations of 4.0° ± 12.3° SEM, 61.0° ± 5.3° SEM, and 87.0° ± 4.2° SEM, respectively (**Figure 3.7.M)**.

The isotropic group demonstrated some direction bias towards +/-90° but the distribution of the cellular orientations was very wide and lacked a prominent peak as compared to the other groups. Across all groups, there was no difference between the mean angle of the inner and outer layers (**Figure 3.7 C&F**), however the angle distributions around the mean differed slightly between layers. For example, we compared the standard deviation values for each layer to examine the how strongly aligned the cells were, or how narrowly or widely the data were distributed around the peak. We found that the outer layers for all groups had slightly smaller standard deviation values suggesting a greater degree of alignment than the inner layers; these difference

were statistically significant for each group however reflected a small difference in angle between the orientations of each layer (**Figure 3.8**). These data suggest that the intended pattern of global cellular alignment was maintained after the tissue fabrication process and that uniform organization was maintained across all cell layers.

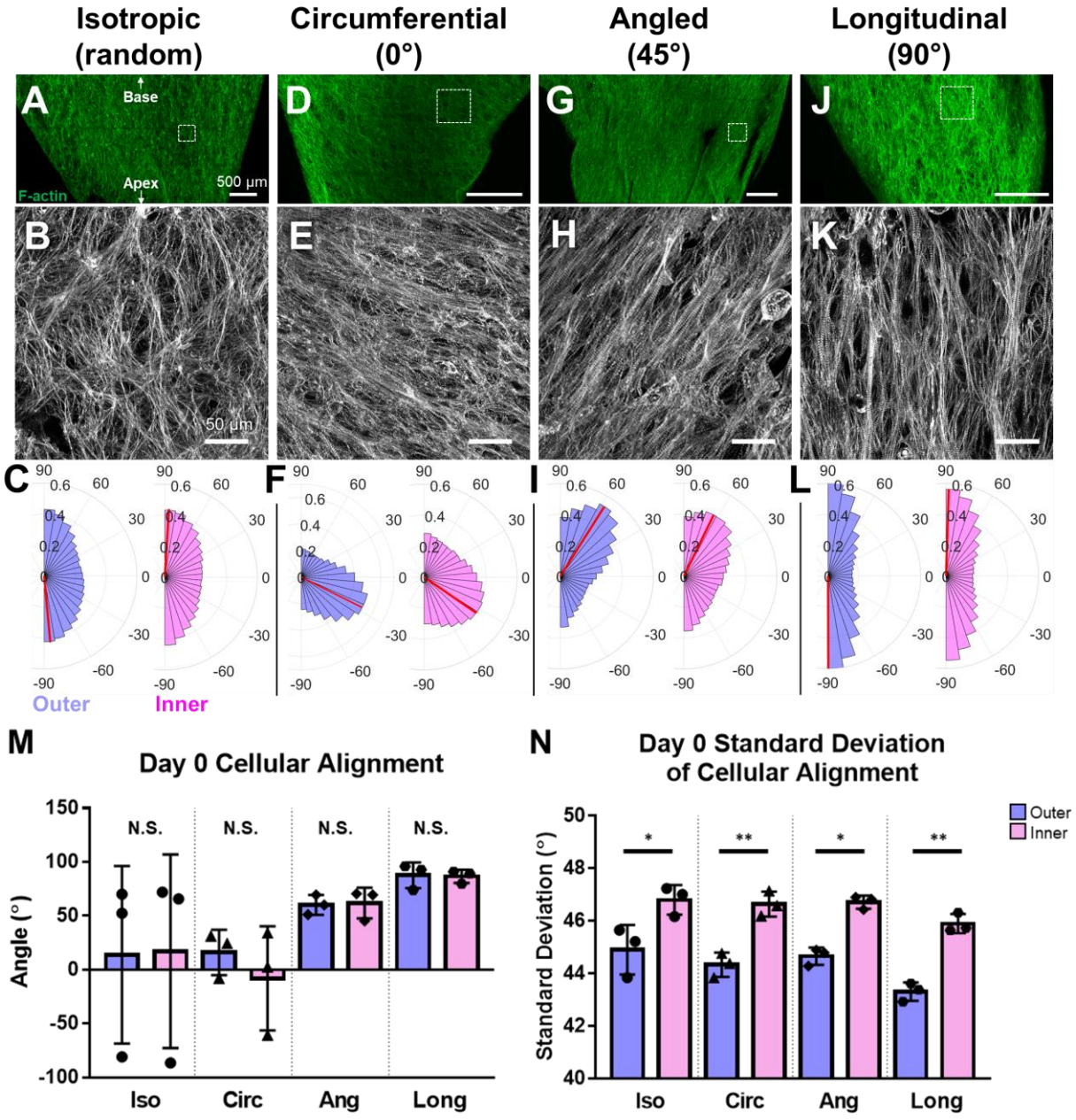

Figure 3.7. Patterning of cellular alignment in 3D cardiac ventricular models. 3D confocal z-stack projections of ventricular models patterned with **(A)** isotropic, **(D)** circumferential (0°), **(G)** angled (45°), and **(J)** longitudinal (90°) cellular organization as demonstrated by the filamentous actin organization (F-actin, green). All scale bars are 500 μm. **(B,E,H,K)** 40x magnification images of boxed insets of (A,D,G,J), respectively. F-actin filaments were false-colored gray for contrast. All scale bars are 50 μm. **(C,F,I,L)** Polar histograms representing the cellular alignment of the inner (pink) and outer (blue) cell layers of each tissue organization (A,D,G,J), respectively. Red lines on each histogram represent the mean orientation angle. **(M)** Average angle of cellular alignment relative to the tissue's short axis of outer (blue) and inner (pink) layers for each tissue group, respectively. **(N)** Average standard deviation of cellular orientation from mean angle of cellular organization. *p<0.05, **p<0.01. Tissue group abbreviations: isotropic (iso), circumferential (circ), angled (ang), longitudinal (long).

3.4.3 Cellular Remodeling Occurs at the Inner Cell Layers of Circumferentially Patterned Models

To determine if cellular patterning was maintained after transfer from their original 2D scaffolds with persistent nanotopographical cues to a dynamic 3D tissue environment, we fixed tissues after 4 days culture and analyzed their global transmural alignment (**Figure 3.8**). Isotropic tissues demonstrated almost no change in organization or angle distribution and maintained a random pattern of cellular alignment (**Figure 3.8.A**). Angled and longitudinal tissues exhibited some degree of remodeling where their alignment distribution became more diffuse as compared to tissues analyzed at day 0, but their mean angle of distribution remained within +/- 15° of the initial patterning scheme (**Figure 3.8.C & D**). To our surprise, the circumferentially patterned tissues exhibited striking transmural remodeling where the inner cell layers had reorganized longitudinally with strong effect, almost perpendicular to their original orientation (**Figure 3.8.B**). Whereas the outer cell layers maintained circumferential patterning on average but remodeled to have more diffuse patterns as compared to circumferential tissues analyzed on day 0 (**Supplemental Videos 3.3 & 3.4**). This result suggested that there might be differences in the transmural patterns of stresses and strains created by circumferentially patterned tissue organization and or contraction patterns as compared to the other tissue

architectures. Therefore, we next sought to computationally model our system to test our hypothesis and better understand the mechanical forces at play between tissues with different architectures.

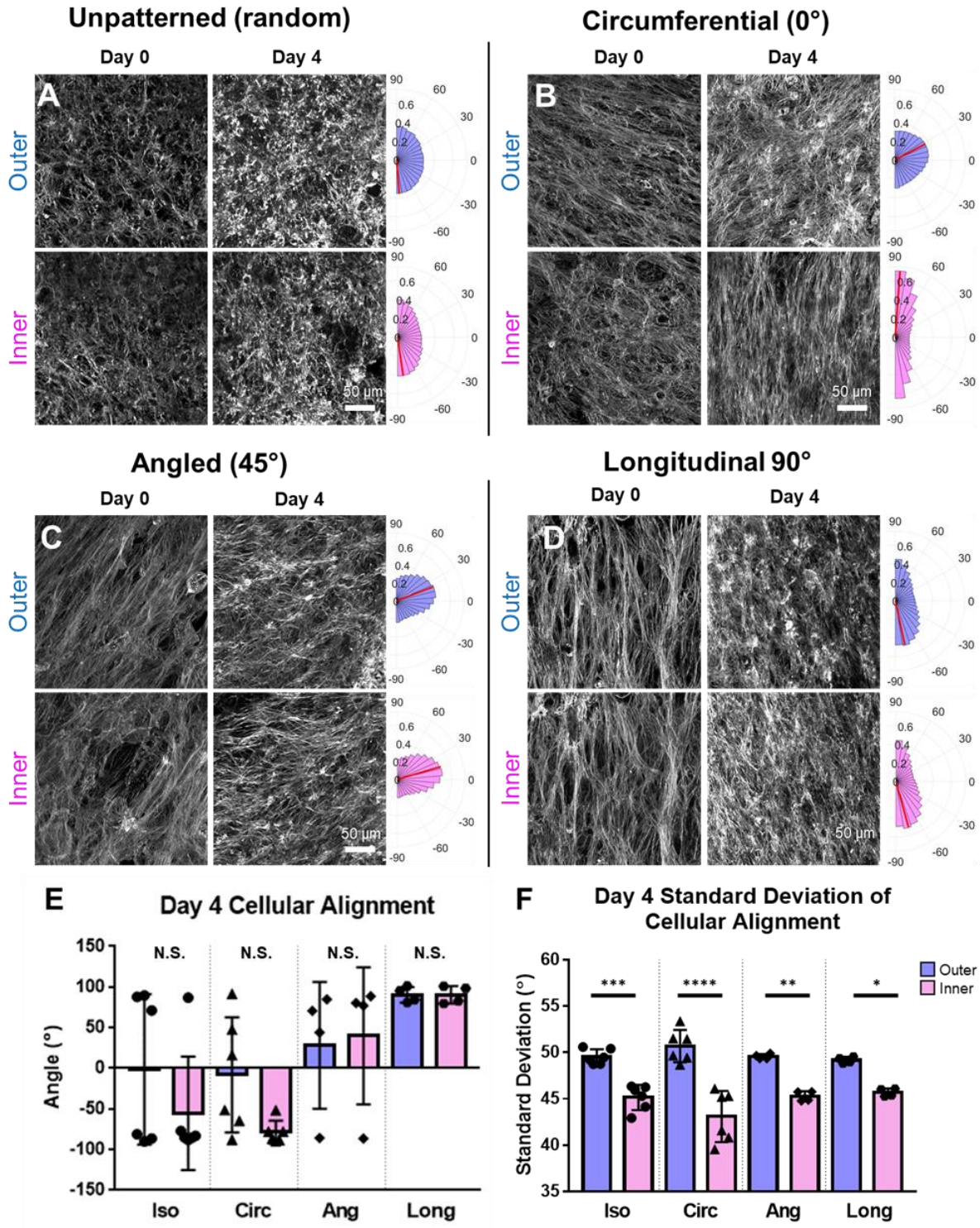

Figure 3.8. Cellular remodeling in 3D ventricular models after 4 days in culture. Representative 40x magnification images of filamentous actin organization on day 0 and day 4 in culture for ventricular models initially patterned with **(A)** isotropic, **(B)** circumferential, **(C)** angled, and **(D)** longitudinal cellular organization on day 0. Polar histograms for the outer (blue) and inner (pink) cell layers for each group on day 4 are positioned to the left of their respective groups. Red lines on each histogram represent the mean cellular orientation angle for each layer, respectively. **(E)** Average angle of cellular alignment relative to the tissue's short axis of outer (blue) and inner (pink) layers for each tissue group, respectively. **(F)** Average standard deviation of cellular orientation from mean angle of cellular organization. *p<0.05, **p<0.01, ***p<0.001, ****p<0.0001. Tissue group abbreviations: isotropic (iso), circumferential (circ), angled (ang), longitudinal (long).

3.4.4 3D Finite Element Model Demonstrates Transmural Gradients of Shear Force and Strain

To understand what might encourage the remodeling observed in the circumferentially patterned tissues but not in the other conditions, we built a finite element model to look at the different stresses and strains that might occur transmurally in each of the conditional models at day 1 in culture. The model included the average tissue dimensions, stiffness of the fibrin hydrogel, wall thicknesses of the fibrin and cell layers, and the different cellular organizations (circumferential (0°), angled (45°), longitudinal (90°), and random) (**Figure 3.9.A & B**). We first provided the model with experimental changes in tissue length from base to apex during contraction and relaxation observed in the longitudinally patterned tissues on day 1. This model was then used to predict the longitudinal and circumferential shear stress and strain transmurally for each experimental condition (**Figure 3.9.C-E**).

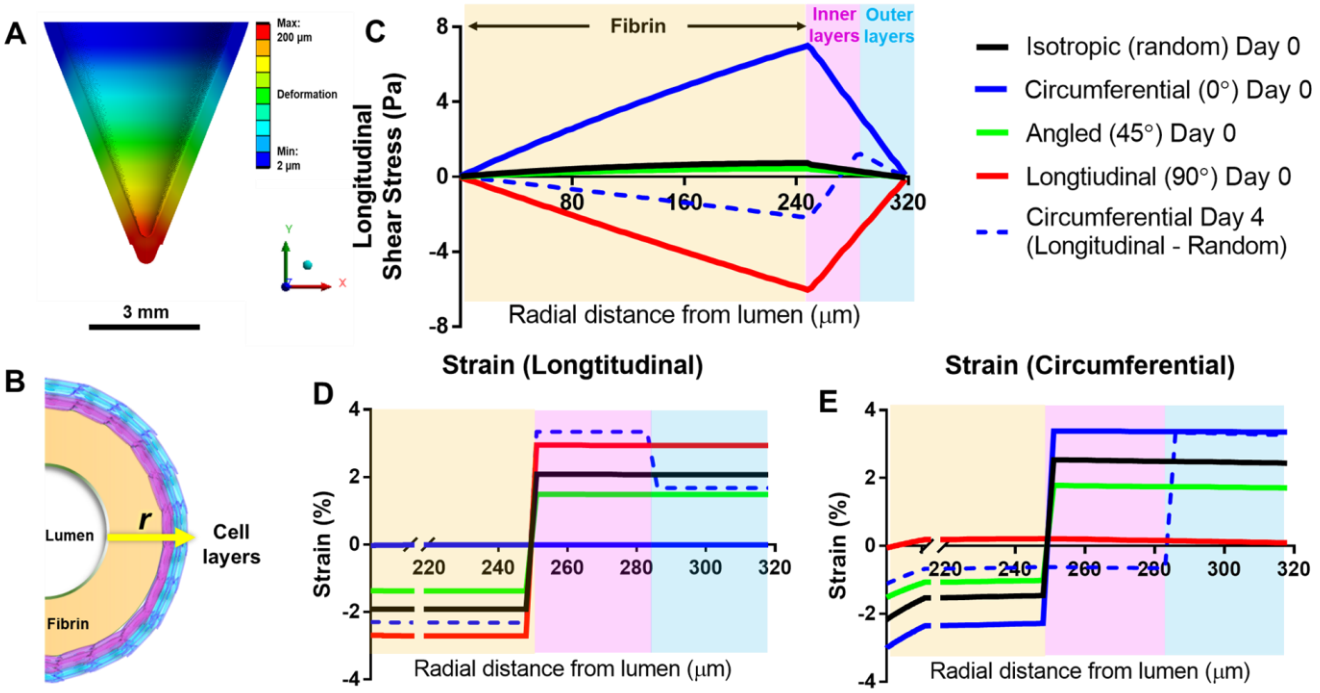

Figure 3.9. 3D Finite element (FE) model of transmural shear stress and strain. (A) 3D rendering of FE model of a longitudinally patterned tissue. The color map projected onto the model represents the range of tissue deformation or movement at peak systole; legend units = µm. **(B)** Schematic of how transmural shear stress and strain were measured in (C-E) where *r* = radial distance from the fibrin wall at the lumen space. Inner and outer cell layers are depicted in pink or blue, respectively. **(C)** Longitudinal shear stress, **(D)** longitudinal strain, and **(E)** circumferential strain measured across a tissue's wall thickness as illustrated in **(B)** for all organizational groups. Pink and blue panels highlight the thickness and position of the inner and outer cell layers, respectively.

From these simulations, isotropic (black lines) and angled tissue models (green lines) were found to have almost identical patterns of stress and strain across the tissue wall thickness, but the isotropic tissues slightly surpassed the angled tissues in every measure. It was interesting to learn that very little shear stress was developed across the cell layers in either of these tissue organizations as compared to the other two experimental conditions. Remarkably, longitudinal shear stresses were observed to be greatest, but opposite, at the interface between the fibrin hydrogel and the inner-most cell

layers of the longitudinal (red lines) and circumferential models (blue lines) (at 250 μm from the tissue lumen) (**Figure 3.9.C**). Similarly, the longitudinal and circumferential strains were also equal but opposite for these two groups (**Figure 3.9.D & E**). These results combined with our structural analysis on day 4 (**Figure 3.8.B**) suggested that the initial circumferential cellular patterning and contractions created large enough longitudinal shearing forces that were perpendicular to the cellular organization at the cell-fibrin interface and promoted cellular remodeling to align with the longitudinal shear.

To test this hypothesis, we adapted our computational model to match the cellular remodeling observed of the circumferentially patterned tissues after 4 days in culture where the inner most layers were patterned longitudinally and the outer most layers were more isotropic (**Figure 3.9.B ,"Circumferential Day 4", dotted blue line**). This configuration revealed that the cells that interface with the fibrin now experienced almost three-fold less shear and in a similar pattern as the longitudinal group. Similarly, the patterns of strain within the longitudinal-random configuration also adapted to mirror that of the longitudinal condition within the inner cell layers only (**Figure 3.9.D & E, blue dotted lines**). There was also a sharp change in both shear stress and strain observed at the interface of the differently oriented inner and outer cells layers. However, the longitudinal shear stress at that interface is markedly less than the shear exhibited at the cell-fibrin interface of the purely circumferential condition (blue line). These results suggested that there is a threshold of perpendicular shear force that is required to promote cellular remodeling to align parallel with the direction if the opposing force.

3.4.5 Cellular Anisotropy and Remodeling Provide Functional Benefit Over Isotropic Tissue Organization

To explore the structure-function relationships that might exist between cellular patterning and the observed remodeling effects, we evaluated each tissue organization for their ability to generate isovolumic pressures (**Figure 3.10**). We hypothesized that ventricular models with biomimetic anisotropic patterning would be afforded better function than isotropic tissues. Pressure-sensing catheters were threaded into the lumens of each ventricular model after 4 days in culture and pressure readings were recorded during spontaneous or electrically paced contractions. Circumferentially and longitudinally patterned tissues performed similarly, and both generated significantly greater pressure amplitudes than isotropic tissues with random cellular organization (**Figure 3.10.C**). They were also found to have faster contraction and relaxation velocities than the isotropic and angled tissues and could be paced at higher frequencies as demonstrated by their maximum capture rates (**Figure 3.10.D-F**). The angled tissues were found not to have significantly greater function than isotropic tissues all around, but there was an upward trend towards the functional performance of the circumferential and longitudinal groups. These findings partially supported our hypothesis that anisotropic tissue organization would be allow for greater functional output but also demonstrated a that circumferential and longitudinal tissue organizations outperformed angled ones.

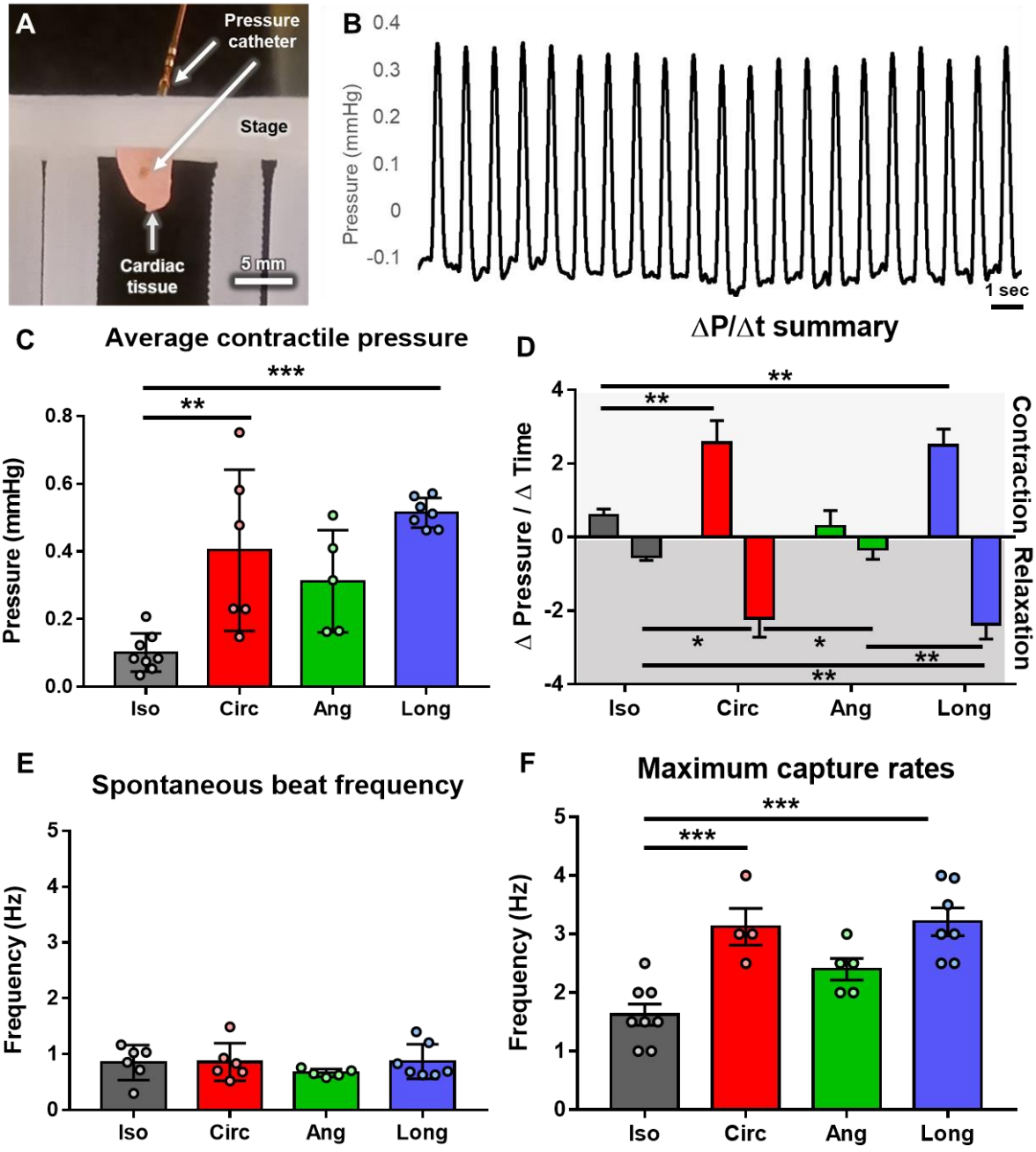

Figure 3.10. Functional assessment of ventricular models thorough isovolumic pressure production. (A) Image of ventricular model under catheterization during live pressure recordings. Tissues are positioned upright on a 3D printed stage during recordings. **(B)** Representative pressure trace from a tissue under 1 Hz electrical field stimulation with 3V, 10 ms pulses. **(C)** Average contractile pressure amplitude from each tissue organization. Each data point highlighted in each group represents one tissue. **(D)** Average contraction and relaxation velocities for each tissue group as measured by the change in pressure over the change in time. **(E)** Average spontaneous beat frequencies recorded from several tissues within each group. **(F)** Average maximum pacing frequencies or capture rates for each group. Tissue group abbreviations: isotropic (iso), circumferential (circ), angled (ang), longitudinal (long). * $p < 0.05$; ** $p < 0.01$; *** $p < 0.0001$.

3.5 Discussion

There are few tissue engineering approaches that can recapitulate the multi-scale organization present in the myocardium, such as formation of an organized functional syncytium within a physiological tissue environment. Here, we adapted our flexible-TNFS platform to engineer human 3D cardiac ventricular models with controllable cellular architecture. Our goal was to model different cellular organizations that exist within the myocardium and evaluate their structure-function relationships. We demonstrated that engineered ventricular models could be patterned with circumferential, angled, and longitudinal cellular organization using fTNFS and custom tissue casting molds (**Figure 3.7**). To our surprise, we observed a stark perpendicular cellular remodeling of the inner most cell layers of the circumferentially patterned tissues. This remodeling effect was not exhibited by any other tissue organization (**Figure 3.8, Supplemental Videos 3.3 & 3.4**). Instead, the longitudinal, angled, and isotropic tissues retained their initial orientation on average but with some loss in alignment intensity. Cellular remodeling in response to mechanical stretching has been previously reported in other studies with adult rat cardiac fibroblasts[15], endothelial cells[16–18], smooth muscle cells[19], dermal fibroblasts[20,21]. These studies were performed with either 2D cell monolayers or 3D laminar tissue patch settings. In the 2D settings, the cells often aligned their stress fibers perpendicularly to the principle direction of cyclic mechanical stretch as a form of “strain avoidance”[16–18]. However, when cells are embedded in a 3D hydrogel, the cells align parallel to the stretch direction [22–25]. We were unsure which phenomena was at play in our system given that the cellular contraction forces provide their own mechanical stimulus in addition to a more complex 3D geometry than the beforementioned studies. We hypothesized that differing

patterns in shear forces or strain might be elicited by each of the initial cellular patterning schemes that “motivate” cellular alignment or avoidance to the direction of these forces.

We investigated this hypothesis by computationally modeling each of the initial cellular alignment patterns and tissue deformations during contraction with a custom 3D finite element model (**Figure 3.9**). We found that circumferentially patterned tissues were predicted to produce large shear forces perpendicular to the cellular alignment on day 1 of culture. We then modeled the observed tissue organization for the circumferential group on day 4 where the inner most layers were now longitudinally aligned and the outer layers were more isotropic (**Figure 3.9, dotted blue lines**). Our model predicted smaller shear forces and in the same direction as the longitudinally patterned tissues at the fibrin-cell interface for this remodeled configuration. We interpreted these data to have two implications: (1) the initially circumferential contraction patterns produce great enough *perpendicular* shear forces at the fibrin-cell interface to promote cellular remodeling, and that (2) cells reorganize to avoid perpendicular shear by aligning parallel to the direction of longitudinal shear provided by upward and inward motions during contractions (**Supplemental Videos 3.1 & 3.2)**. With this logic, the angled and isotropic tissue organizations did not exhibit the same remodeling because strong gradients of shear stress were not present to promote their reorganization. Additionally, the longitudinally patterned tissues produced large shear forces at the cell-fibrin interface but in the same direction as the upward tissue movements during contraction, and therefore cells remained oriented longitudinally. In combination, these results are congruous with other reports of cells in 3D settings aligning with the direction of mechanical stretch [22–26], but

they also suggest that remodeling is simultaneously an avoidance tactic of high shear forces.

When we evaluated each model's ability to create pressure after 4 days in culture, circumferential and longitudinally patterned tissues outperformed isotropic and angled tissues and were also capable of capturing at higher pacing frequencies. These results coupled with our observation of longitudinal remodeling in the circumferential tissue case suggest that longitudinal tissue architecture provides functional benefit by greater pressure production, contraction and relaxation speeds, and faster pacing frequencies. We postulated that this is likely due to the greater cellular alignment in the longitudinal direction overall in both the circumferential and longitudinal cases (**Figure 3.9.B & D, day 4**).

It was interesting to observe that the angled tissues did not have significantly better function than isotropic tissues. However, our computational model suggested that they have similar patterns of shear force and strain transmurally (**Figure 3.11**), which might explain how their functional outputs were also similar. For example, angled tissues exhibit torsional contraction patterns that follow in the direction of their diagonal cellular organization. In this case, their total exerted force is divided between the x (circumferential) and y (longitudinal) directions and therefore cannot create as much shear stress as the circumferential or longitudinal tissues resulting in shear stress profiles similar to isotropic tissues. Although angled tissues possessed greater cellular organization than isotropic ones, these data suggest that how the contractile force is distributed spatially is also important for tissue function.

Overall, these results support the hypothesis that recapitulating the anisotropic organization of the myocardium within a physiological 3D tissue environment provide functional benefit compared to isotropic models. Additionally, the observed remodeling effect in response to gradients of transmural shearing forces has implications for how helical myocardial patterning might occur in cardiac morphogenesis and development. For example, the embryonic heart first begins as a circumferentially patterned tube and develops advanced helical myocardial patterning around 12-14 weeks after fertilization in humans[27,28]. However, it is poorly understood as to how this patterning is inspired or initiated[29]. In future, this approach could be used to study the mechanics of tissue morphogenesis and mechanotransduction in the heart and other organs.

3.6 References

1. Mekkaoui, C. *et al.* Diffusion Tractography of the Entire Left Ventricle by Using Free-breathing Accelerated Simultaneous Multisection Imaging. *Radiology* **282**, 850–856 (2017).
2. Garcia-Canadilla, P. *et al.* Myoarchitectural disarray of hypertrophic cardiomyopathy begins pre-birth. *J. Anat.* **235**, 962–976 (2019).
3. Yen Ho, S. Anatomy and myoarchitecture of the left ventricular wall in normal and in disease. doi:10.1093/ejechocard/jep159.
4. Liu, Y. W. *et al.* Human embryonic stem cell-derived cardiomyocytes restore function in infarcted hearts of non-human primates. *Nat. Biotechnol.* **36**, (2018).
5. Smith, A. S. T., Macadangdang, J., Leung, W., Laflamme, M. A. & Kim, D.-H. Human iPSC-derived cardiomyocytes and tissue engineering strategies for disease modeling and drug screening HHS Public Access. *Biotechnol Adv* **35**, 77–94 (2017).
6. Tzatzalos, E., Abilez, O. J., Shukla, P. & Wu, J. C. Engineered heart tissues and induced pluripotent stem cells: Macro- and microstructures for disease modeling, drug screening, and translational studies. *Advanced Drug Delivery Reviews* vol. 96 234–244 (2016).

7. MacQueen, L. A. *et al.* A tissue-engineered scale model of the heart ventricle. *Nat. Biomed. Eng.* 1 (2018) doi:10.1038/s41551-018-0271-5.

8. Lee, A. *et al.* 3D bioprinting of collagen to rebuild components of the human heart. *Science (80-.).* **365**, 482–487 (2019).

9. Lee, E. J., Kim, D. E., Azeloglu, E. U. & Costa, K. D. Engineered Cardiac Organoid Chambers: Toward a Functional Biological Model Ventricle. *Tissue Eng. Part A* **14**, 215–225 (2008).

10. Kupfer, M. E. *et al.* In Situ Expansion, Differentiation and Electromechanical Coupling of Human Cardiac Muscle in a 3D Bioprinted, Chambered Organoid. *Circ. Res.* CIRCRESAHA.119.316155 (2020) doi:10.1161/CIRCRESAHA.119.316155.

11. Williams, N. P. *et al.* Engineering anisotropic 3D tubular tissues with flexible thermoresponsive nanofabricated substrates. *Biomaterials* **240**, 119856 (2020).

12. Streeter, D. D. & Hanna, W. T. Engineering mechanics for successive states in canine left ventricular myocardium. II. Fiber angle and sarcomere length. *Circ. Res.* **33**, 656–64 (1973).

13. Pope, A. J., Sands, G. B., Smaill, B. H. & LeGrice, I. J. Three-dimensional transmural organization of perimysial collagen in the heart. *Am. J. Physiol. Circ. Physiol.* **295**, H1243–H1252 (2008).

14. Gargiulo, S. *et al.* PET/CT Imaging in Mouse Models of Myocardial Ischemia. *J. Biomed. Biotechnol.* **2012**, 1–12 (2012).

15. Chen, K. *et al.* Role of boundary conditions in determining cell alignment in response to stretch. *Proc. Natl. Acad. Sci.* **115**, 986–991 (2018).

16. Kaunas, R., Nguyen, P., Usami, S. & Chien, S. Cooperative effects of Rho and mechanical stretch on stress fiber organization. *Proc. Natl. Acad. Sci. U. S. A.* **102**, 15895–15900 (2005).

17. Moretti, M., Prina-Mello, A., Reid, A. J., Barron, V. & Prendergast, P. J. *Endothelial cell alignment on cyclically-stretched silicone surfaces*.

18. Hsu, H.-J., Lee, C.-F. & Kaunas, R. A Dynamic Stochastic Model of Frequency-Dependent Stress Fiber Alignment Induced by Cyclic Stretch. doi:10.1371/journal.pone.0004853.

19. Pang, Y., Wang, X., Lee, D. & Greisler, H. P. Dynamic quantitative visualization of single cell alignment and migration and matrix remodeling in 3-D collagen hydrogels under mechanical force. *Surg. Serv.* (2011) doi:10.1016/j.biomaterials.2011.02.003.

20. Huang, C. *et al.* Biological effects of cellular stretch on human dermal fibroblasts. in *Journal of Plastic, Reconstructive and Aesthetic Surgery* vol. 66 e351–e361 (Elsevier, 2013).

21. Bellows, C. G., Melcher, A. H. & Aubin, J. E. *ASSOCIATION BETWEEN TENSION*

AND ORIENTATION OF PERIODONTAL LIGAMENT FIBROBLASTS AND EXOGENOUS COLLAGEN FIBRES IN COLLAGEN GELS IN VITRO. *J. Cell Sci* vol. 58 (1982).

22. Matsumoto, T. *et al.* Three-Dimensional Cell and Tissue Patterning in a Strained Fibrin Gel System. doi:10.1371/journal.pone.0001211.

23. Roby, T., Olsen, S. & Nagatomi, J. Effect of Sustained Tension on Bladder Smooth Muscle Cells in Three-Dimensional Culture. doi:10.1007/s10439-008-9545-5.

24. Foolen, J., Deshpande, V. S., Kanters, F. M. W. & Baaijens, F. P. T. The influence of matrix integrity on stress-fiber remodeling in 3D. (2012) doi:10.1016/j.biomaterials.2012.06.103.

25. Lee, E. J., Holmes, J. W. & Costa, K. D. Remodeling of Engineered Tissue Anisotropy in Response to Altered Loading Conditions. doi:10.1007/s10439-008-9509-9.

26. Obbink-Huizer, C. *et al.* Computational model predicts cell orientation in response to a range of mechanical stimuli. *Biomech. Model. Mechanobiol.* **13**, 227–236 (2014).

27. Mekkaoui, C. *et al.* Diffusion MRI Tractography of the Developing Human Fetal Heart. *PLoS One* **8**, e72795 (2013).

28. Sosnovik, D. E. & Geva, T. Imaging the Microstructure of the Human Fetal Heart. *Circ Cardiovasc Imaging* **11**, 8298 (2018).

29. Grosberg, A. & Gharib, M. Physiology in Phylogeny: Modeling of Mechanical Driving Forces in Cardiac Development. *Heart Fail. Clin.* **4**, 247–259 (2008).

30. Jiao, A. *et al.* Thermoresponsive nanofabricated substratum for the engineering of three-dimensional tissues with layer-by-layer architectural control. *ACS Nano* **8**, 4430–9 (2014).

31. Guan, X. *et al.* Dystrophin-deficient cardiomyocytes derived from human urine: New biologic reagents for drug discovery. *Stem Cell Res.* **12**, 467–480 (2014).

32. Lian, X. *et al.* Directed cardiomyocyte differentiation from human pluripotent stem cells by modulating Wnt/β-catenin signaling under fully defined conditions. *Nat. Protoc.* **8**, 162–175 (2012).

33. Palpant, N. J. *et al.* Generating high-purity cardiac and endothelial derivatives from patterned mesoderm using human pluripotent stem cells. *Nat. Protoc.* **12**, 15–31 (2017).

34. Jiao, A. *et al.* Regulation of skeletal myotube formation and alignment by nanotopographically controlled cell-secreted extracellular matrix. *J. Biomed. Mater. Res. Part A* (2018) doi:10.1002/jbm.a.36351.

35. Cho, H. *et al.* Self-Organization in High-Density Bacterial Colonies: Efficient Crowd Control. *PLoS Biol.* **5**, e302 (2007).

Chapter 4. Conclusions and Future Directions

The research presented in this dissertation illustrate the role of myocardial cellular organization at micro- and macroscopic levels and its influence over cardiac tissue function. Our approach of engineering cellular organization first at the level of cellular monolayers and then using them as building blocks for 3D tissue fabrication provided a unique advantage over other bioengineering approaches. This technique enabled production of different tissue architectures with relative ease. These tissues demonstrated the ability to generate measurable isovolumic pressures with relatively few cells and were used to differentiate between anisotropic and isotropic tissue architectures. We observed functional advantages of tissues with organized cellular patterning over those with random cellular orientations, including greater pressure production, faster contraction and relaxation velocities, and higher maximum pacing frequencies. Additionally, the combination of cellular patterning, ventricular 3D tissue geometries, and soft fibrin hydrogels that mimic myocardial tissue stiffnesses, enabled an unexpected cellular remodeling effect that was not observed in 2D culture. We were able to computationally model this effect and found that different tissue organizations give rise to unique gradients of transmural shear stress and strain.

These findings have potential implications for how helical myocardial tissue patterning happens in cardiac morphogenesis. For example, the primitive embryonic heart structures first form a tubular shape with layers of circumferentially ordered cardiomyocytes[1]. It is possible that with circumferential contraction patterns, like the ones seen in our circumferentially patterned ventricular models, transmural gradients of stress

and strain are also produced that promote cellular remodeling of differing magnitudes in each cell layer. These forces would surely act in concert with and arise from changing hemodynamic loads within the heart tube caused by contraction and morphogenesis of surrounding embryonic tissue[2]. Hypotheses similar to these have been computationally modeled[3,4] and studied in several animal models[5] for over two centuries. However, there is still very little that is known about the genesis of helical myocardial patterning and embryonic heart development. Recent advances in stem cell biology and tissue engineering have laid the groundwork for building complex tissues in a dish, as demonstrated in this dissertation. It is possible that these technologies are ready for a new challenge: recapitulating cardiac morphogenesis in vitro. Given its tubular structure, comparatively simpler to the chambered heart associated with later points of development, the linear heart tube would be an approachable starting point to model. By providing a “seed structure” of the primitive heart and promoting its morphogenesis, this approach would provide an opportunity to learn more about developmental biology through reverse engineering. In turn, this would be a critical step for developing more representative models of heart development that can be used for more advanced modeling of heart disease, have applications in regenerative medicine, and enable biological discovery.

Another natural application of this platform would be to model cardiovascular diseases using patient derived iPSC-CMs and other derivative cell types, such as cardiac fibroblasts, smooth muscle cells, endocardial cells, and hemogenic cell lineages that were not explored in this research. By substituting diseased for healthy cells, one could explore functional and structural phenotypic differences to that of a healthy ventricular

model. These differences could be pinpointed and interrogated with molecular biology, gene editing, and delivery of small molecules for therapeutic approaches. For example, Duchenne muscular dystrophy (DMD) is an X-linked genetic condition characterized by muscle wasting due to the loss or truncation of the dystrophin protein, resulting in respiratory, orthopedic, and cardiac dysfunction[6]. Currently, there are no clinically available therapies that target the underlying dystrophin gene mutations. Furthermore, a clinically tested therapeutic, Sildenafil, was famously withdrawn from market since it did not offer any translational benefits that were promisingly observed in dystrophic mouse models[7]. Part of the reason for the lack of available therapies is a paucity of accurate, human preclinical models to elucidate the mechanistic pathways that contribute to the progressive loss of function that is exhibited in dystrophic cardiomyopathies. Current in vitro models of DMD cardiomyopathy using human induced pluripotent stem cell-derived cardiomyocytes (iPSC-CMs) have been unable to investigate how dystrophic CMs contribute to heart failure at the organ level due to their over-simplified, two-dimensional (2D) or single-cell configurations[8,9]. In addition, the mdx mouse model of DMD only captures the orthopedic and respiratory manifestations of the disease but lacks a representative cardiomyopathic phenotype[10]. To date there are no human 3D in vitro cardiac tissue models that can recapitulate physiological cardiac ventricular function in the context of dystrophic cardiomyopathy.

4.1 References

1. Price, R. L., Chintanowonges, C., Shiraishi, I., Borg, T. K. & Terracio, L. Local and regional variations in myofibrillar patterns in looping rat hearts. *Anat. Rec.* **245**, 83–93 (1996).

2. Tobita, K., Garrison, J. B., Liu, L. J., Tinney, J. P. & Keller, B. B. Three-dimensional myofiber architecture of the embryonic left ventricle during normal development and altered mechanical loads. *Anat. Rec. Part A Discov. Mol. Cell. Evol. Biol.* **283A**, 193–201 (2005).

3. Grosberg, A., Gharib, M. & Kheradvar, A. Effect of Fiber Geometry on Pulsatile Pumping and Energy Expenditure. *Bull. Math. Biol.* **71**, 1580–1598 (2009).

4. Grosberg, A. & Gharib, M. Physiology in Phylogeny: Modeling of Mechanical Driving Forces in Cardiac Development. *Heart Fail. Clin.* **4**, 247–259 (2008).

5. Wallingford, J. B. The 200-year effort to see the embryo. *Science (80-.).* **365**, 758–759 (2019).

6. Perloff, J. K., de Leon, A. C. & O'Doherty, D. The cardiomyopathy of progressive muscular dystrophy. *Circulation* **33**, 625–48 (1966).

7. Leung, D. G. *et al.* Sildenafil does not improve cardiomyopathy in Duchenne/Becker muscular dystrophy. *Ann. Neurol.* **76**, 541–9 (2014).

8. Long, C. *et al. Correction of diverse muscular dystrophy mutations in human engineered heart muscle by single-site genome editing*. https://www.ncbi.nlm.nih.gov/pmc/articles/PMC5796795/pdf/aap9004.pdf (2018).

9. Macadangdang, J. *et al.* Nanopatterned Human iPSC-Based Model of a Dystrophin-Null Cardiomyopathic Phenotype. *Cell. Mol. Bioeng.* **8**, 320–332 (2015).

10. Durbeej, M. & Campbell, K. P. Muscular dystrophies involving the dystrophin-glycoprotein complex: an overview of current mouse models. *Curr. Opin. Genet. Dev.* **12**, 349–61 (2002).

VITA

Nisa Penland Williams was born as Nisa Marie Penland in Gibraltar, Michigan in 1992. She received her Bachelor of Science in Neuroscience from the University of Michigan in 2014. From 2011 to 2014, she worked as an Undergraduate Researcher in Dr. Kenneth Cadigan's laboratory. She earned her Ph.D. in Bioengineering from the University of Washington in 2020.